



Johannes Michael Funk, BSc.

Testing of Cathode Materials for Solid Oxide Fuel Cells

MASTERARBEIT

zur Erlangung des akademischen Grades Diplom-Ingenieur

Masterstudium Advanced Materials Science

Eingereicht an der

Technischen Universität Graz

Betreuer:

Ao.Univ.-Prof. Dipl.-Ing. Dr.techn. Klaus Reichmann

Institut für Chemische Technologie von Materialien

Graz, Mai 2018

Deutsche Fassung:

Beschluss der Curricula-Kommission für Bachelor-, Master- und Diplomstudien vom 10.11.2008

Genehmigung des Senates am 1.12.2008

EIDESSTÄTTLICHE ERKLÄRUNG

Ich erkläre an Eides statt, dass ich die vorliegende Arbeit selbstständig verfasst, andere als die angegebenen Quellen/Hilfsmittel nicht benutzt, und die den benutzten Quellen wörtlich und inhaltlich entnommenen Stellen als solche kenntlich gemacht habe.

Graz, am

.....

(Unterschrift)

Englische Fassung:

STATUTORY DECLARATION

I declare that I have authored this thesis independently, that I have not used other than the declared sources / resources, and that I have explicitly marked all material which has been quoted either literally or by content from the used sources.

Graz,

.....

date

(signature)

Acknowledgement

First and foremost I want to thank my supervisor from the Technical University Graz, Ao.Univ.-Prof. Dipl.-Ing. Dr.techn. Klaus Reichmann for mentoring this thesis and providing essential advice and scientific guidance throughout the whole process. Further my very special thanks goes to my advisor and college from AVL side, Dipl.-Ing. Jörg Mathé for giving me the required backing and advice from company side and to the APU-team leader Dipl.-Ing. Michael Reissig for making this project possible in the first place. Additional shout-out to all the members of the fuel cell department at AVL for supporting me during the course of my employment so far. I am furthermore highly thankful for the sublime cooperation with Dr. L.G.J. Bert de Haart and all the members of the IEK-9 at the Forschungszentrum Jülich GmbH I had the opportunity to work with during my time in Germany and hereafter. Also I want to thank Dipl.-Ing. Dr.techn. Wolfgang Schafbauer from Plansee SE and his colleges for supplying knowledge and the needed sample materials for my experiments. A big thank you goes to assoz.Prof. Dipl.-Ing. Dr.mont. Edith Bucher and Dipl.-Ing. Dr.mont. Andreas Egger from the Department of Physical Chemistry at the Montanuniversität Leoben for kindly providing the required equipment, knowledge and skill for the post mortem analysis tasks. Last, but not in the slightest way least I would like to express my deepest gratitude to my family, friends, colleges and all the people around me for supporting me beyond anything during the process of my thesis and the eventful and exciting educational journey over the last couple of years, really helping to keep the emotions positive and the vibes up high, it was an extraordinary pleasure.

Abstract

In the prospect of renewable energy generation fuel cell technology offers promising possibilities regarding the efficient conversion of chemical into electrical energy in both stationary and mobile applications. In particular solid oxide fuel cell (SOFC) systems achieve supreme efficiencies and further allow the utilization of different hydrocarbon fuels in order to steer the transition away from combusting fossil fuels towards renewable energy generation.

In the course of the present thesis the possibilities to heat up a SOFC system exploiting a blend of ethanol and water were investigated. In particular the opportunity to bring the unit up to its optimum operating temperature by using the exhaust gasses of a burner utilizing the ethanol fuel was in the focus research. Therefore the tolerance of the fuel cell itself for such gases containing oxygen, water and carbon dioxide is of major interest. A series of single cell tests was executed, where artificial exhaust gas was supplied to the fuel cell's air electrode (cathode) at temperatures varying from 350°C to 650°C between each trial in order to replicate certain domains of a startup procedure. To evaluate the merits of the experiments power output (IV-curves) and the frequency response (EIS) were recorded periodically and the samples were later examined regarding their microstructure and chemical composition.

The results of cell testing give evidence for enhanced degradation of the tested cells when exhaust gas is applied. Further the drop in power output going along with an increase in resistance is more distinct towards lower temperatures. The post mortem investigation reveals macroscopic changes (cracks, delamination) of the cathode layers amongst suspected changes in the microstructure constituting to degradation.

Kurzfassung

Im Kontext der Energiewende hin zu erneuerbarer Energiegewinnung bieten Brennstoffzellen vielversprechende Möglichkeiten zur effizienten Erzeugung von elektrischem Strom aus chemisch gebundener Energie sowohl in stationären, als auch mobilen Anwendungen. Festoxidbrennstoffzellen(SOFC)-Systeme erzielen hohe Wirkungsgrade und erlauben weiters die Verwendung von kohlenwasserstoffhaltigen Kraftstoffen, was den Übergang vom Verbrennen fossiler Treibstoffe hin zu alternativen Energiequellen erleichtern soll.

Im Zuge dieser Arbeit wurde die Verwendung eines Brenners zum Aufheizen eines Ethanol-Wasser betriebenen SOFC-Systems untersucht. Im Detail ist die Toleranz der einzelnen Brennstoffzelle gegenüber einem Abgas bestehend aus Sauerstoff, Wasser und Kohlendioxid von besonderem Interesse. Dazu wurde eine Serie von Einzelzelltests durchgeführt, bei denen ein artifizielles Abgas auf die Lufterlektrode (Kathode) der Zelle geschickt wurde. Dabei wurde die Temperatur in einem Bereich von 350°C bis 650°C zwischen den Versuchen variiert, um Punkte während eines Startvorganges abzubilden. Während der Experimente wurden das Leistungsvermögen (UI-Kurven) und die Frequenzantwort (EIS) der Zellen aufgezeichnet, welche danach auf deren Mikrostruktur und chemischen Zusammensetzung untersucht wurden.

Die Ergebnisse weisen auf eine erhöhte Degradation der getesteten Zellen unter Abgas Bedingungen hin. Zusätzlich ist der Leistungsverlust verbunden mit einem Anstieg des Widerstandes bei niedrigeren Temperaturen am ausgeprägtesten. Die folgende Untersuchung der Exemplare zeigt makroskopische Beschädigungen (Risse, Delaminierung) der Kathodenschicht zusammen mit Veränderungen in der Mikrostruktur der Zellen, welche für den Leistungsverlust der Zellen verantwortlich gemacht werden.

Contents

Acronyms.....	1
1. Introduction	3
2. Fuel Cell Basics	4
2.1. Unit cell.....	4
2.2. Types of fuel cells	5
2.2.1. Low temperature fuel cells	7
2.2.2. High temperature fuel cells	8
2.2.3. Summary of fuel cell types	9
3. APU program at AVL List GmbH.....	11
3.1. Nissan e-Bio Fuel-Cell® vehicle	11
3.2. Ethanol APU development at AVL	13
4. Solid oxide fuel cells.....	16
4.1. Fundamental principle	16
4.2. Electrochemical and thermodynamic basics.....	17
4.2.1. Nernst equation and open circuit voltage	18
4.2.2. Losses during operation.....	19
4.2.3. Cell efficiency.....	20
4.3. Cell designs	22
4.3.1. Planar SOFCs.....	23
4.3.2. Tubular SOFCs	23
4.4. Materials and manufacturing.....	24
4.4.1. Cell fabrication	24
4.4.2. Substrate.....	26
4.4.3. Electrolyte	26
4.4.4. Anode.....	27
4.4.5. Cathode	28
5. SOFC cathode materials	29
5.1. Reaction mechanisms and kinetics.....	29
5.2. Perovskite materials	30

5.3.	Oxygen ion transport in perovskite oxides	32
5.3.1.	Definition of diffusion coefficient.....	32
5.3.2.	Oxygen tracer diffusion coefficient	32
5.3.3.	Surface exchange coefficient	33
5.3.4.	Defect chemistry of perovskite oxides.....	34
5.4.	Influences on diffusivity in MIECs	37
5.4.1.	Effect of A-site cation	37
5.4.2.	Effect of B-site cation	37
5.4.3.	Other influences on oxygen diffusivity.....	38
5.5.	LSCF as cathode material for SOFCs	39
6.	Degradation mechanisms in SOFCs	41
6.1.	Cathode degradation	42
6.2.	Degradation of LSCF-based cathode materials	42
6.2.1.	Effect of H ₂ O on cathode performance.....	43
6.2.2.	Effect of CO ₂ on cathode performance.....	46
7.	Experimental	48
7.1.	Testing environment	48
7.2.	Sample cells for testing.....	49
7.3.	Test bed setup.....	51
7.3.1.	Cell housing and sealing	52
7.3.2.	Measurement equipment at test bed.....	54
7.4.	Testing schedule.....	54
7.4.1.	Startup procedure	54
7.4.2.	Test matrix	56
8.	Results of cell tests	59
8.1.	LSCF 1: Reference trial at 650°C (1309-005A)	59
8.2.	LSCF 2: Exhaust gas trial at 650°C (1309-005B)	62
8.3.	LSCF 3: Exhaust gas trial at 500°C (1309-019B)	64
8.4.	LSCF 4: Exhaust gas trial at 350°C (1309-019A)	67
8.5.	Summary of cell tests	70

9.	Post mortem analytics	72
9.1.	Analytics strategy	72
9.2.	Suspected failure modes	73
9.3.	Results from SEM-analytics	75
9.3.1.	LSCF 0: Green sample (1309-175B)	75
9.3.2.	LSCF 1: Reference sample 650°C (1309-005A)	76
9.3.3.	LSCF 2: Exhaust gas sample 650°C (1309-005B)	78
9.3.4.	LSCF 3: Exhaust gas sample 500°C (1309-019B)	79
9.3.5.	LSCF 4: Exhaust gas sample 350°C (1309-019A)	80
9.4.	Results of XRD-analytics	81
9.4.1.	Overview of XRD spectra	81
9.4.2.	Main phase spectrum	81
9.4.3.	Secondary phases section 1 (24-31°)	84
9.4.4.	Secondary phases section 2 (36-41°)	84
9.4.5.	Secondary phases section 3 (42.2-48°)	85
9.4.6.	Summary of XRD-results	86
10.	Roundup and discussion	88
11.	Conclusion and prospect	91
12.	References	93
13.	Illustration directory	102
14.	List of tables	106
15.	Appendix	107

Acronyms

AFC	Alkaline fuel cell
APU	Auxiliary power unit
ASC	Anode supported cell
ASR	Area specific resistance
AVL	Anstalt für Verbrennungskraftmaschinen List
BSCF	Barium strontium cobalt ferrite
BSD	Backscattered electron detector
CGO	Cerium gadolinium oxide (GDC)
CHP	Combined heat and power
CTE	Coefficient of thermal expansion (TEC)
DBL	Diffusion barrier layer
DC	Direct current
EBZ	Entwicklungs- und Vertriebsgesellschaft Brennstoffzelle
EDX	Energy dispersive X-ray spectroscopy
EG	Exhaust gas
EIS	Electrochemical impedance spectroscopy
EMF	Electromotive force
ESC	Electrolyte supported cell
FCV	Fuel cell vehicle
FU	Fuel utilization
FZJ	Forschungszentrum Jülich GmbH
GDC	Gadolinium doped ceria (CGO)
GPU	Gas processing unit
GT	Gas turbine
GTCC	Gas turbine combined cycle
GUI	Graphical user interface
HC	Hydrocarbon
HEX	Heat exchanger
HT	High temperature
IC	Interconnector
ICDD	International Centre for Diffraction Data
ICE	Internal combustion engine

IEK	Institut für Energie- und Klimaforschung
IGCC	Integrated gasification combined cycle
IT	Intermediate temperature
ITM	Intermediate temperature metal
IV	Current-voltage
LSCF	Lanthanum strontium cobalt ferrite
LSGM	Lanthanum gallium magnesium oxide
LSM	Lanthanum strontium manganite
LT	Low temperature
LZO	Lanthanum zirconia oxide
MCFC	Molten carbonate fuel cell
MFC	Mass flow controller
MIEC	Mixed ionic and electronic conductor
MSC	Metal supported cell
MUL	Montanuniversität Leoben
OCV	Open circuit voltage
ORR	Oxygen reduction reaction
PAFC	Phosphoric acid fuel cell
PEFC	Polymer electrolyte fuel cell
PEM	Proton exchange membrane/Polymer electrolyte membrane
PEMFC	Proton exchange membrane fuel cell
PVD	Physical vapor deposition
REF	Reference
SE	Secondary electron detector
SEM	Scanning electron microscope
SOFC	Solid oxide fuel cell
SZO	Strontium zirconia oxide
TEC	Thermal expansion coefficient (CTE)
TPB	Triple phase boundary
XRD	X-ray diffraction
YSZ	Ytria stabilized zirconia/Ytria zirconium oxide

1. Introduction

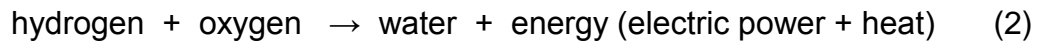
In terms of decentralized power supply fuel cells offer a promising prospect regarding simple, efficient and clean generation of electricity. The basic principle of a fuel cell is the conversion of chemical energy directly to electric energy through an electrochemical process, so there is no need for any moving parts in particular. The exchange of electric charge arises from an electrochemical reaction between a reducing medium (fuel containing hydrogen) and an oxidizer (commonly oxygen in air). Consequently this charge separation yields to the performance of electric work. Hence electrical energy is generated, which further can be harvested and stored for multiple use. The fact that fuel cells can operate highly efficient while at the same time reducing system complexity and environmental footprint, qualifies them as a reasonable alternative for clean power generation of any scale. However there are still some technical challenges to overcome.

Mobile applications (e.g. automotive engineering) however demand some important requirements which need to be taken into account. In order to provide energy for vehicle movement the power plant needs to operate in a dynamic manner. Especially start up times, when the system ramps up to full operational power, are crucial for the marketability of a powertrain. The Auxiliary Power Units (APUs) developed at AVL List GmbH use Solid Oxide Fuel Cell (SOFC) technology to generate electricity from hydrogen carbonate containing fuels (e.g. diesel or ethanol). These SOFCs require operating temperatures of around 650°C to function properly. Boosting an APU-system of multiple kilowatts from room temperature to its dedicated operating temperature requires some substantial effort in the first place before one can gain electricity out of it.

For a rapid startup procedure the use of a burner directly combusting the on-board fuel would be a neat solution. However the compatibility of the fuel cell itself with combustion exhaust gas still remains unsolved. The scope of this thesis is to examine the heatup of a fuel cell system by using the exhaust gas of a burner combusting an ethanol-water mixture, which is in contact with the air electrode of the cell. Therefore this application of off-gas in direct combination with the fuel cell's cathode material is subject to be evaluated.

2. Fuel Cell Basics

As already mentioned in the introduction the principle of a fuel cell is to convert chemical energy into electric energy. This is achieved in the fundamental process of oxidizing hydrogen with oxygen producing water.[1]

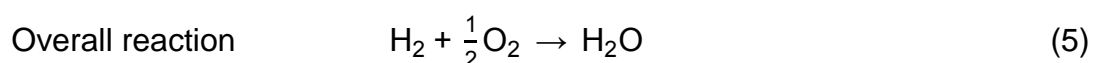
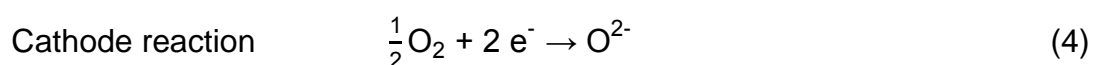
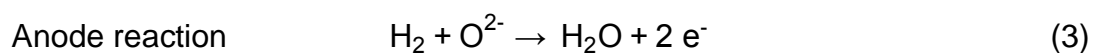


Reaction (1) requires hydrogen and oxygen as educts. Hydrogen is either supplied purely or as part of a gas of a reformed hydrocarbon (HC) fuel, whereas the oxygen is commonly taken out of ambient air. Of course the isolation of pure hydrogen is an energy consuming process and using it as an energy carrier does not outweigh the efforts of its production in the first place, but nevertheless it is a promising energy carrier for renewable energy sources.[2]

Furthermore the scalability of a fuel cell system qualifies them for different demands ranging from small portable electric devices as well as auxiliary power units with the output of multiple kilowatts for the use in vehicles up to large scale stationary combined heat and power (CHP) applications offering energy in the megawatt range.[3]

2.1. Unit cell

The basic concept of a fuel cell is schematically shown as a unit cell in Fig.1. The chemical energy is provided in the form of gaseous fuel on the anode side (negative electrode) and oxygen supplied on the cathode side (positive electrode). Both anode and cathode are separated by an electrolyte, which works as both an ion conductor and electronic isolator. At the electrodes, basically two partial reactions of (1) happen:[1]



In Fig.1 the schematic of a single fuel cell unit is shown. Fuel is supplied continuously to the anode side, while the oxidant (usually oxygen out of ambient air) is flowing over to the cathode. The electrochemical reactions (3) and (4) take place at the surface of the electrodes. The electron transfer is inhibited by the electrically isolating electrolyte, which forces the electrons to flow through an outer circuit, driven by the electric potential.

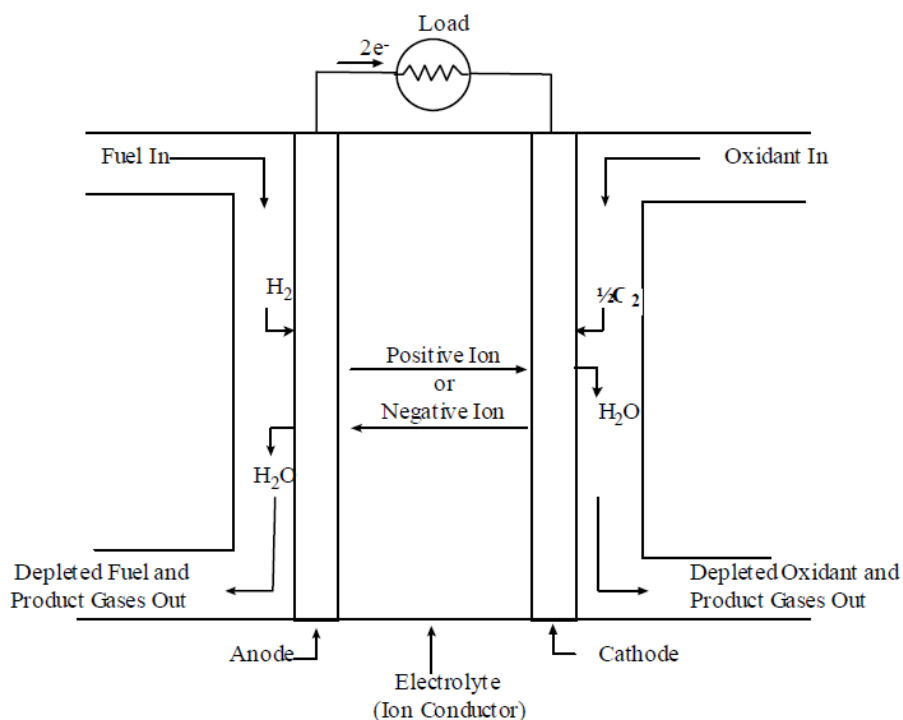


Figure 1: Schematic of a unit cell[1]

As electrodes usually porous materials are used because they offer a high specific surface promoting ion exchange. However it is beneficial that these materials are mixed ionic and electronic conductors (MIECs). The electrolyte separating the two electrodes has to offer ion conductivity (depending on fuel cell type) and electron isolation.

2.2. Types of fuel cells

In general fuel cells are classified by their operation temperature into high temperature (HT) and low temperature (LT) fuel cells. They are further categorized by the type of electrolyte they utilize. The electrolyte material is responsible for the charge transfer caused by the electrochemical reaction (1). Thus a general classification of fuel cells with their main properties such as operating temperature, type of electrolyte and range of applications is shown in Table 1.

Table 1: Comparison of fuel cell technologies [4][5][6]

	Electrolyte	Operating T(°C)	Stack Size	Overall efficiency	Applications	Advantages	Disadvantages
Low Temperature	PEM	50-100	<10kW-100kW	60% 40% stationary transportation	- Backup power - Portable power - Distributed generation - Transportation - Specialty vehicles	- Solid electrolyte reduces corrosion and electrolyte management problems - Low temperature - Quick start-time	- Expensive catalysts - Sensitive to fuel impurities - Low temperature waste heat
	AFC	90-250	10-100kW	60%	- Military - Space	- Cathode reaction faster in alkaline electrolyte leads to high performance - Low cost components	- Sensitive to CO2 in fuel and air - Electrolyte management - Pt catalyst
	PAFC	150-220	400 kW 100 kW module	40%	- Distributed generation	- Higher temperature enables CHP - Higher tolerance to fuel impurities	- Long start-up time - Low power
High Temperature	MCFC	600-700	300kW-3MW 300kW module	45-50%	- Electric utility - Distributed generation	- High efficiency - Fuel flexibility - Can use a variety of catalysts - Suitable for CHP	- High temperature corrosion and breakdown - Long start-up time - Low power
	SOFC	550-1000	1kW-2MW	60%	- Auxiliary power - Electric utility - Distributed generation	- High efficiency - Fuel flexibility - Flexible Catalyst and solid electrolyte - Suitable for CHP/CHHP-hybrid/GT	- High temperature corrosion and breakdown - Long start-up time

2.2.1. Low temperature fuel cells

Fuel cell systems operating at temperatures below 250°C, such as proton exchange membrane-, also named polymer electrolyte fuel cells (PEMFC, PEFC or PEM), alkaline fuel cells (AFC) and phosphoric acid fuel cells (PAFC) are categorized as low temperature (LT) fuel cells. They operate utilizing pure hydrogen as fuel. Lower temperatures allow faster startup times and more dynamic controllability of the system.

That is the reason why polymer exchange membrane fuel cells are already used in mobile applications such as fuel cell vehicles (FCV). They incorporate an ion exchange membrane (e.g. fluorinated sulfonic acid polymers) and are operated at temperatures below 100°C. However, at these low temperatures catalysts in the form of noble metals such as platinum are necessary to enhance the oxidation of the hydrogen according to reaction (1). The need of such precious catalysts, the vulnerability to fuel impurities and carbon monoxide (CO) poisoning and the required water management for the membrane substantially increases manufacturing costs of these PEM-systems while operation itself constitutes a challenge.[1]

Alkaline fuel cells are a technology famously pioneered in the Apollo spacecraft vehicle for combined production of electricity and water. Concentrated potassium hydroxide (KOH) retained in a matrix (mostly asbestos) is supplied as electrolyte for operating temperatures up to 250°C maximum. Although providing a high chemical activity leading to quick startup times at a relatively low price point, AFCs are sensitive to carbon dioxide (CO₂) in both air and fuel requiring additional cost-pushing purification processes. AFCs therefore have only seen their use in military or space applications so far.[1,5]

Phosphoric acid fuel cells use phosphoric acid (H₃PO₄) embodied in a silicon carbide matrix as an electrolyte and are typically operated at temperatures between 150°C and 220°C, depending on the concentration of the acid. PAFCs are primarily developed for stationary power generation and feature better CO-tolerance than other low temperature fuel cells, but still need extensive fuel processing, and the aggressive nature of the phosphoric acid requires the use of expensive materials for stack design.[1]

As a recap, low temperature fuel cells offer a promising prospect regarding quick startup procedures and dynamic controllability. However the need of pure hydrogen and expensive catalyst materials in order to make ion exchange work at low temperatures and the vulnerability against different impurities rises the complexity and further the costs of such systems.

2.2.2. High temperature fuel cells

As illustrated in Table 1 high temperature fuel cells operate at temperatures above 500°C and can be scaled to a wide range of power output. The elevated operating temperatures are beneficial to the electrochemical reaction (1), which is promoted towards higher temperatures. However the temperature on the other hand influences the theoretical fuel cell efficiency, which is outlined in in chapter 4.2.3. Cell efficiency.

Molten carbonate fuel cells (MCFC) use a combination of alkali carbonates as an electrolyte, which are supported by a LiAlO_2 matrix. Operating temperatures range from 600°C up to 700°C, at which the alkali carbonates form a highly ion conductive molten salt. Carbonate ions (CO_3^{2-}) are responsible for the ionic conductivity. MCFCs offer advantages concerning fuel flexibility and simplicity and are suitable for stationary CHP applications. However long startup times and the corrosivity of the electrolyte leading to a complex demand of materials has set them back in different ways.[1]

Solid oxide fuel cells (SOFC) on the other hand incorporate an electrolyte made of dense metal oxides. They are operated at temperatures between 550°C and 1000°C providing thermal activity for oxygen ions to be conducted through the ceramic membrane. Typically Y_2O_3 -stabilized ZrO_2 is used as an electrolyte material with several options for anode and cathode materials (see chapter 4). SOFCs used to be limited by the ion conductivity of the electrolyte at lower temperature levels, but current developments boost the technology of so called intermediate temperature SOFCs (IT-SOFC), which provide decent power output in the range of 550°C up to 1000°C.[1]

SOFC-technology offers high electric efficiencies and fuel flexibility regarding different types of hydrocarbon fuels at a relatively robust and cost-effective system setup compared to low temperature FCs.

On the flipside the high operating temperatures lead to longer startup times and do not promote dynamic system operation. Further the elevated temperatures lead to multiple challenges regarding material selection for cell and stack design in terms of thermal expansion and stability influencing reliability.[7]

2.2.3. Summary of fuel cell types

The choice of the appropriate type of fuel cell for a certain application vastly depends on the boundary conditions of the desired system, as described in Table 2.

Table 2: Influences on fuel cell type selection

Boundary condition	Impact on system selection and design
Fuel type	availability of either pure hydrogen or some HC-species type of fuel; need of fuel flexibility regarding HC-fuels like ethanol or diesel shifts the technology demand towards HT-fuel cells (comparison of the fuel cell types and their fuel requirements in Fig.2)
Operating environment	whether the system is for stationary or mobile application; determines and limits weight and size of the system and also influences the demands towards the operational modes
Handling characteristics	requirement of fast startup times and dynamic controllability; demand for rapid startup times currently calls for LT-fuel cells
Power output	affects system complexity and material choice; at high specific outputs (measured in kW/kg _{system}) the demand for special materials and technological effort increases
Price	influenced by system complexity, type of fuel and material requirements

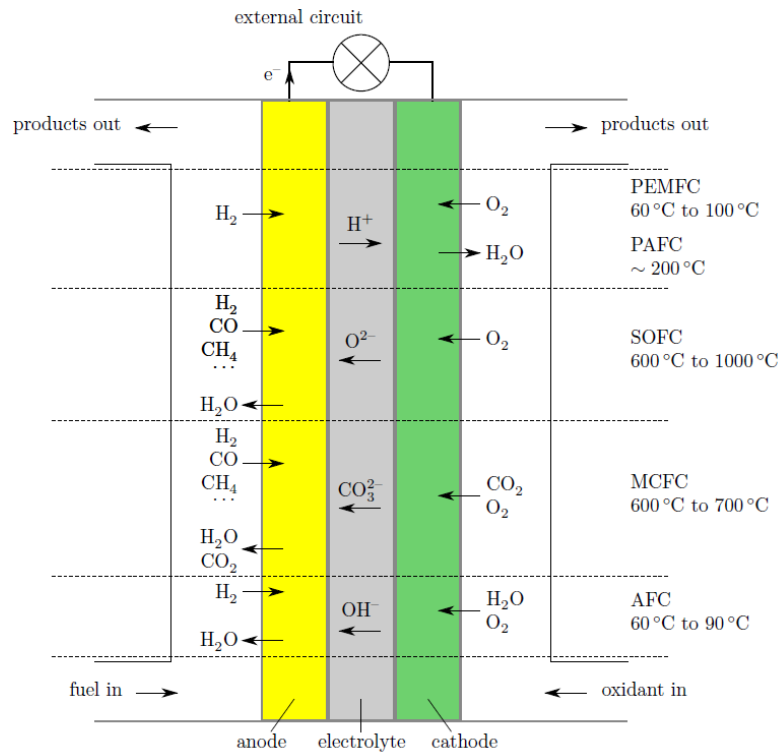


Figure 2: Overview of reactants and operating temperatures of the most important types of fuel cells[8]

For the AVL List GmbH's APU-program the SOFC-technology has been chosen due to its fuel flexibility and robustness to environmental influences.

3. APU program at AVL List GmbH

The AVL List GmbH has been involved in SOFC system development since the year 2002. Currently there are several fields of development for either stationary or mobile application of HT-fuel cell systems realized in cooperation with various industrial partners. The systems operate either with diesel or a blend of ethanol and water (aquanol).[9] There are several advantages of a fuel cell system as a power plant for vehicles compared to conventional combustion engines, such as improved fuel efficiency, reduced emissions (both greenhouse gases and particles), silent operation and a reduced ecological footprint in general with regard to efficiency and fuel consumption.

The research for this master thesis was done in the course of the auxiliary power unit development for mobile application in vehicles fueled with bioethanol. In areas of high availability of bioethanol the combination of an electric powertrain in combination with an APU incorporating SOFC technology generating electricity offers a promising concept of future mobility. The ethanol produced biologically from sugarcane or corn offers a better environmental footprint compared to fossil fuels. Based on the easy availability in areas like North and South America systems like this could be easily introduced to the existing market without the needs of new sorts of charging infrastructure or safety measurements.[10] As the CO₂-emissions from a fuel cell vehicle running on ethanol are beyond those of an equally powerful conventional petrol or diesel car and on condition that the fuel is produced organically from plants leading to a somewhat closed CO₂-circle leads to a smaller ecological footprint of such propulsion systems.

3.1. Nissan e-Bio Fuel-Cell® vehicle

In 2016 the Nissan Motor Company announced the development of their e-Bio Fuel-Cell® car (Fig.3) based on their existing e-NV200 platform in cooperation with AVL as the world's first for automotive use. The vehicle houses a SOFC system, which is capable of producing electricity out of either pure ethanol or an ethanol-water blend.[10] The vehicle is driven by an electric motor which receives power from a battery, which is further charged by the APU. The basic architecture of the system is shown in Fig.4.



Figure 3: Nissan e-Bio Fuel-Cell vehicle based on the e-NV200 platform[10]

In order to be utilized by a SOFC the ethanol fuel stored in the fuel tank has first to be evaporated and fed to a reformer, where it is essentially split up into basic molecules such as hydrogen (H_2), methane (CH_4), carbon monoxide (CO) and carbon dioxide (CO_2).

The reformat gas is further supplied to the fuel cell stack, where it is oxidized to water, carbon dioxide and energy according to reaction (1).[11] The combined exhaust gas has to be further processed after the stack in order to eliminate CO - and residual CH_4 emissions, before it can be emitted to the environment. The electric energy generated from the fuel cell system then charges a battery pack, which acts as an energy buffer and storage system. The APU-system is targeted to deliver 5kW of electric power at a system efficiency of 50%.[12] More basic data of the fuel cell vehicle can be seen in Table 3.

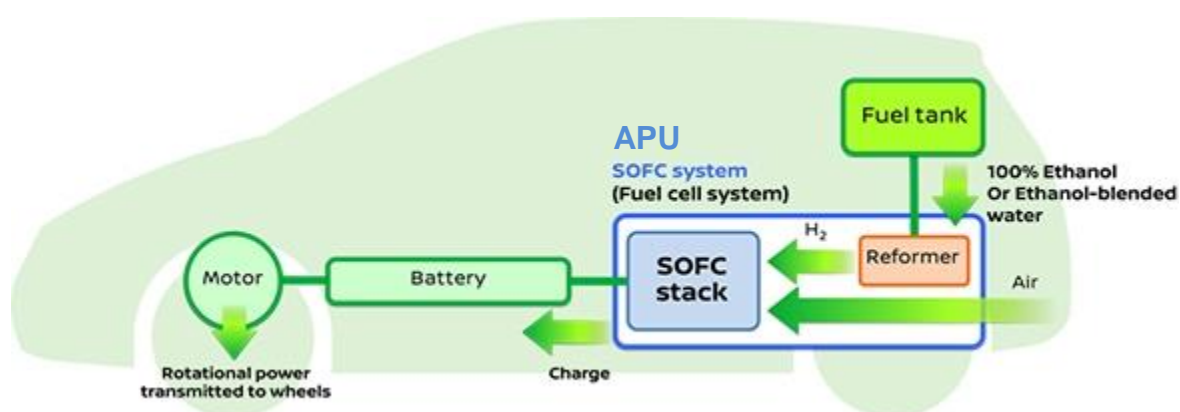


Figure 4: Schematic architecture of an electric vehicle incorporating a SOFC-APU[10]

Table 3: Vehicle data for Nissan e-Bio Fuel-Cell® vehicle[10]*

Vehicle platform	Nissan e-NV200
Power output electric motor	80 kW
Power output SOFC system	5 kW
Energy sources	Electricity, Fuel (pure ethanol or ethanol-water blend)
Battery capacity	24 kWh
Fuel tank capacity	30 l
Estimated range	+600 km

*Note: due to prototype status the vehicle specifications are subject to change

3.2. Ethanol APU development at AVL

The scope of this thesis is to gather knowledge about possible startup procedures of an ethanol fueled SOFC system. The APU design developed by AVL (Fig.5) consists of three main parts: the media supply, the gas processing unit and the stack module.[9]

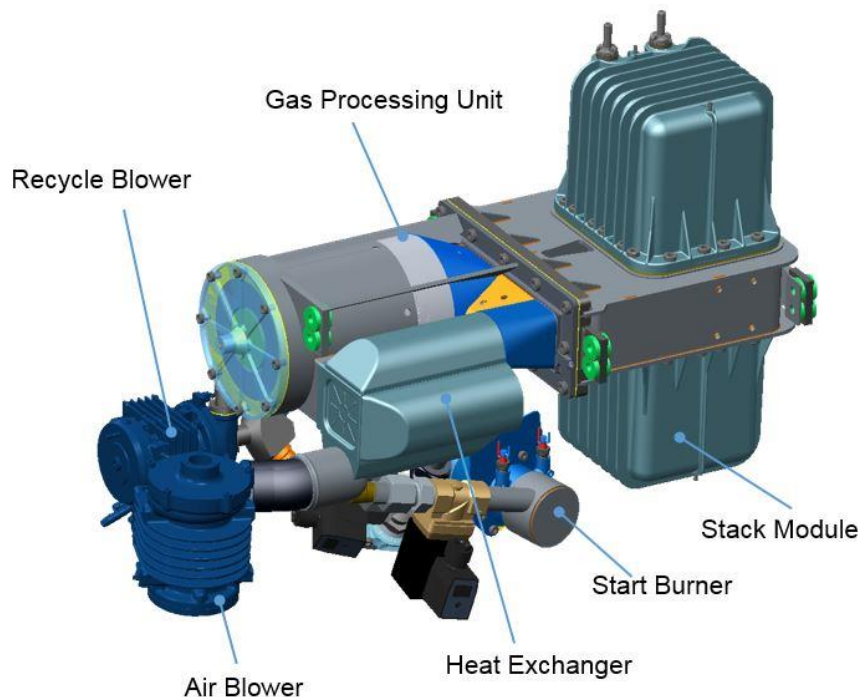


Figure 5: APU-system developed by AVL - main parts[9]

The media supply consists of an air blower for the cathode side air, a fuel pump for the anode side fuel supply and some valves for controlling. The gas processing unit (GPU) involves a burner providing heat for the startup process, an evaporator and reformer unit, which processes ethanol, a heat exchanger for pre-heating the cathode air and an oxidation catalyst for exhaust gas after treatment. The stack module of the latest generation ethanol APU consists of two SOFC stacks, which are operated at 650°C and produce a combined 5kW of electric power gross under normal operation.[9]

Fig.6 shows a process diagram of the ethanol APU with all its basic components and actuators. Fuel is fed into the system by a fuel pump either supplying the catalytic burner for startup or the vaporizer and reformer unit for normal operation. The thermal energy of the exhaust gas is recycled in order to provide heat for the fuel evaporation and reforming process and for air preheating through the cathode side heat exchanger (HEX).

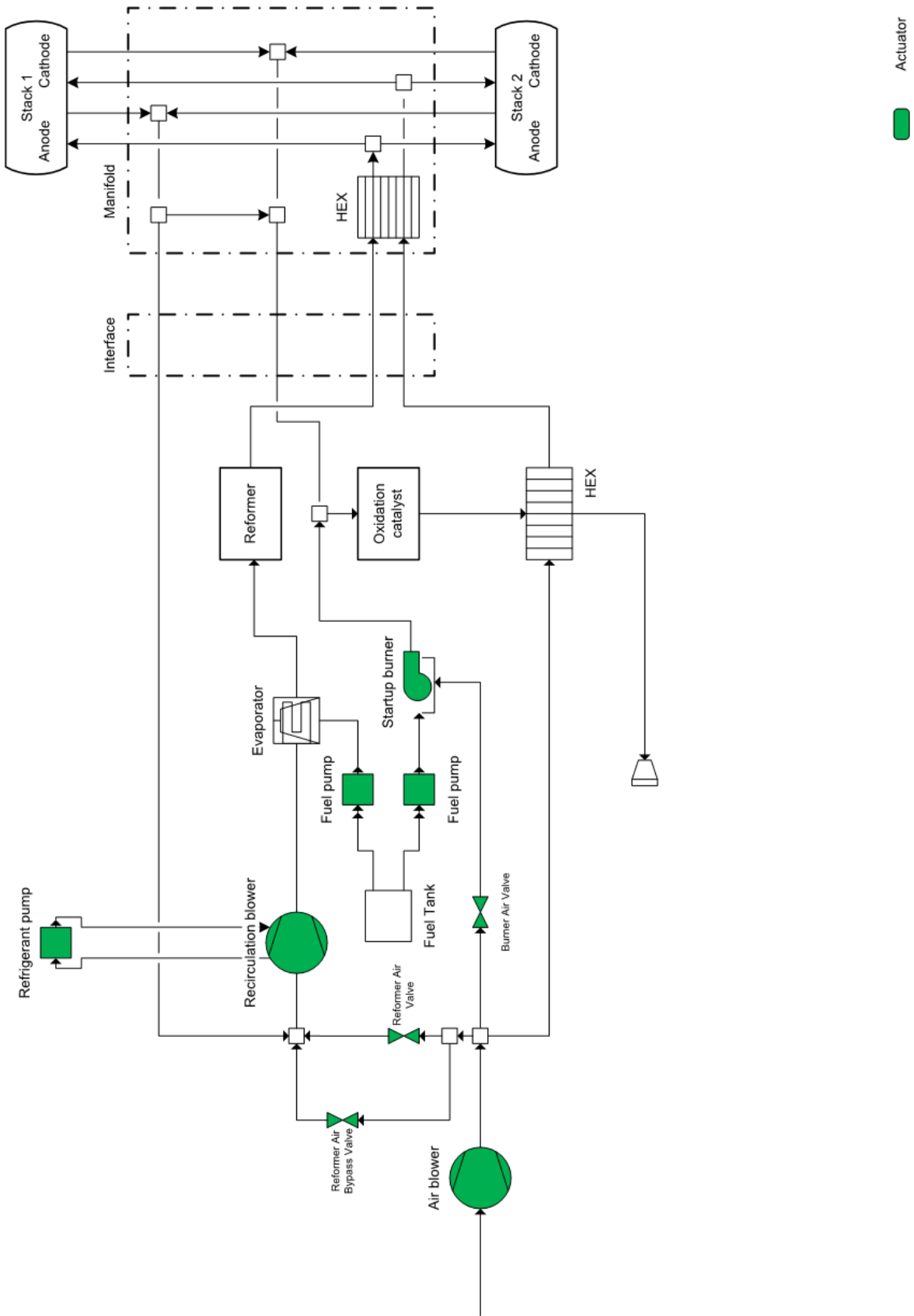


Figure 6: Flowsheet of ethanol APU developed by AVL including sensor and actuator position [13]

4. Solid oxide fuel cells

Regarding the use of solid oxide fuel cell technology in the course of AVL's APU program, a more in depth review of this technology is done in this chapter. As already mentioned in 2.2. SOFCs are high temperature fuel cells operating between 550°C and 1000°C.

4.1. Fundamental principle

As their name suggests, SOFCs contain a solid, non-porous ceramic oxide as an electrolyte. These ceramic oxides achieve oxygen ion (O^{2-}) conductivity at elevated temperatures, which is the reason why they have to be operated at temperatures above 600°C, where the ion mobility is enhanced. The electrolyte is sandwiched between the two electrodes, which are responsible for gas exchange with either hydrogen (anode) or oxygen (cathode). The basic operating principle of a SOFC with hydrogen fuel and oxygen as an oxidant can be seen in Fig.7.[1,5]

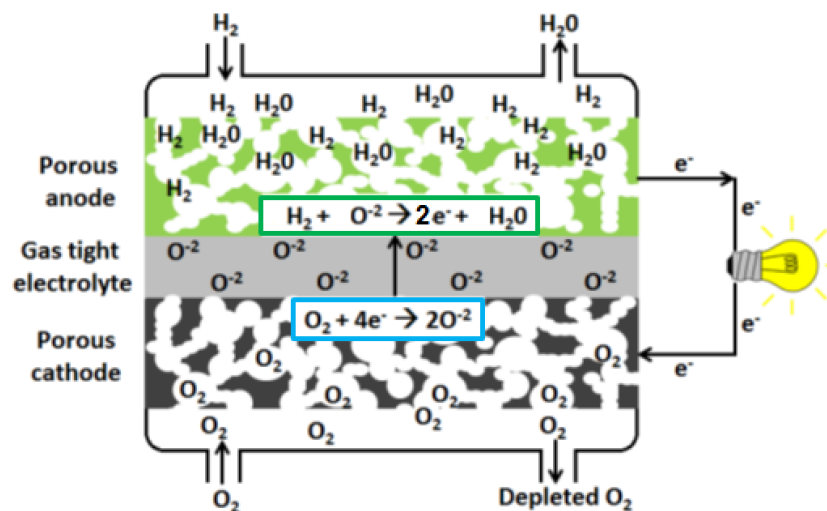
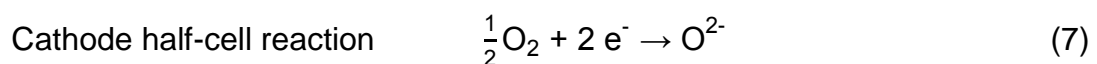
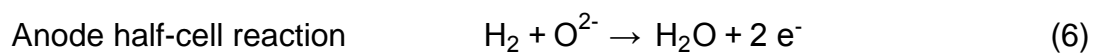
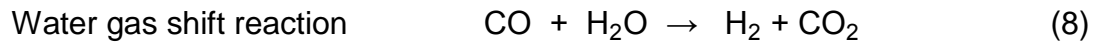


Figure 7: Operating principle of a SOFC[14]

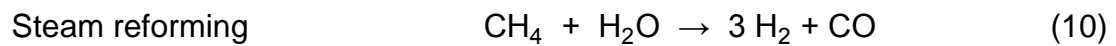
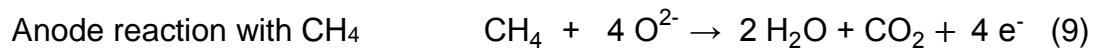
The electrode half-cell reactions take place at the electrode-electrolyte-pore interface. This area is called triple phase boundary (TPB), where the electrolyte, electrode and gas phase meet.



Apart from pure hydrogen, carbon monoxide (CO) can also be used as fuel in a SOFC, either directly or as product of the water gas shift reaction (8).[11,15]



Other HC-fuels can be used due to internal reforming. Methane (CH₄) can be processed directly or as a result of the steam reforming process in presence of water (see reaction (9)(10)).[11,15]



For hydrocarbons of higher order (e.g. ethanol, diesel) the fuel has to be pre-reformed by a catalytic reformer (see Fig.6), which splits the longer HC-molecules into hydrogen, methane, carbon monoxide and carbon dioxide before it is applied to the fuel cell. This flexibility in the use of different fuels makes the SOFC a promising alternative for power generation using various HC-fuels.

4.2. Electrochemical and thermodynamic basics

Generally speaking in a fuel cell power is generated by the electrochemical reaction of a fuel with an oxidizer according to equation (1). The driving force for this reaction is the change of the Gibbs free energy ΔG (or Gibbs free enthalpy ΔG). In order to make the reaction happen spontaneously, the change of ΔG from the reaction educts to the products has to be negative.

$$\Delta G_R < 0 \quad (\text{for } T, p = \text{const.}) \quad (11)$$

$$\Delta G_R = \Delta H_R - T \Delta S_R \quad (12)$$

ΔH_R represents the change in enthalpy and ΔS_R the change in entropy. ΔH_R is the totally available thermal energy, whilst $T \Delta S_R$ (either positive or negative) represents the unusable energy lost from an entropy change inside the system. A reaction is called endothermic, when external energy is needed for the process to occur, hence ΔH_R has a positive value. If on the other hand ΔH_R is negative, the system dissipates energy to the environment and the reaction is called exothermic.[1]

4.2.1. Nernst equation and open circuit voltage

In a first approximation all of ΔG_R can be transformed into electric energy W_{el} : [1]

$$W_{el} = -\Delta G_R = n F E_0 \quad (13)$$

where n represents the number of electrons participating in the reaction, F is the Faraday constant and E_0 is the standard potential of the cell.

The performance of a fuel cell is measured by its voltage output at a certain current. For single cells the current and power output are normalized to a current, respectively power density per surface area (usually A/cm^2 or W/cm^2). At equilibrium conditions this voltage output is characterized as open circuit voltage (OCV or EMF) and described by the Nernst equation:

$$E_N = E_0 + \frac{RT}{nF} \ln \prod p_i^{v_i} \quad (14)$$

with

$$E_0 = -\frac{\Delta G_R}{nF} \quad (15)$$

where R is the ideal gas constant, p_i are the partial pressures of the reactants and v_i are the stoichiometric coefficients of the reaction.

The Nernst equation (14) represents the ideal OCV, which sets the upper limit for maximum achievable performance of a fuel cell. The Nernst equations for various cell reactions regarding equations (6)-(10) are listed in Table 4.

Table 4: Nernst equations according to different fuel cell reactions (see chapter 4.1.) [1]

Cell Reactions*	Nernst Equation
$H_2 + \frac{1}{2}O_2 \rightarrow H_2O$	$E = E^\circ + (RT/2F) \ln [P_{H_2} / P_{H_2O}] + (RT/2F) \ln [P_{O_2}^{1/2}]$
$CO + \frac{1}{2}O_2 \rightarrow CO_2$	$E = E^\circ + (RT/2F) \ln [P_{CO} / P_{CO_2}] + (RT/2F) \ln [P_{O_2}^{1/2}]$
$CH_4 + 2O_2 \rightarrow 2H_2O + CO_2$	$E = E^\circ + (RT/8F) \ln [P_{CH_4} / P_{H_2O}^2 P_{CO_2}] + (RT/8F) \ln [P_{O_2}^2]$

- | | | | |
|-----|---------------------------------|---|------------------------|
| (a) | anode | P | partial pressure |
| (b) | cathode | R | universal gas constant |
| E | equilibrium potential (E_N) | T | temperature [K] |
| F | Faraday constant | | |

4.2.2. Losses during operation

In reality cell voltages are below the ideal potentials shown before. When current flows through the cell, the potential is lower than the OCV due to several non-reversible effects.

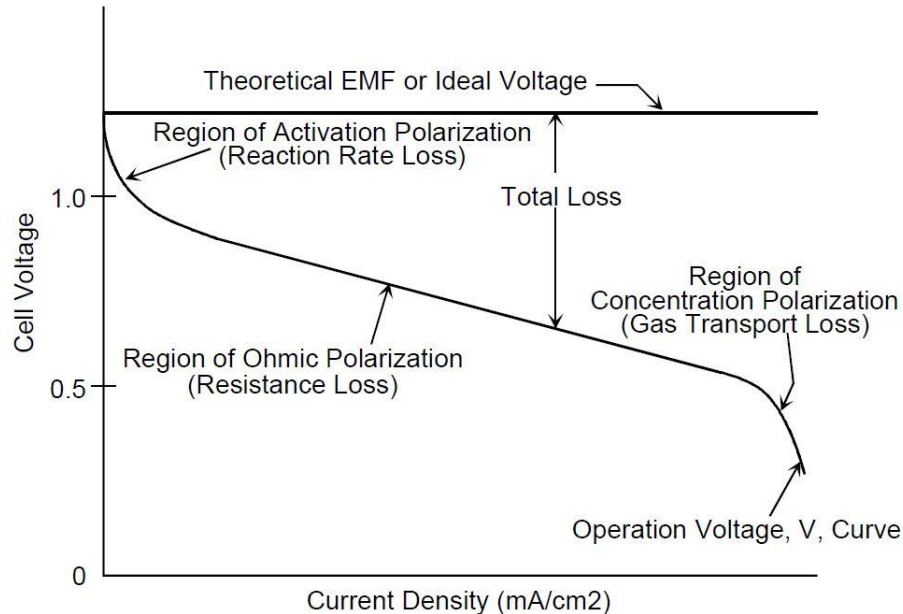


Figure 8: Characteristic IV-curve with different types of losses[1]

Fig.8 shows a typical plot of voltage versus current (IV-curve) of a real fuel cell compared to the theoretically possible potential. The real cell potential E_{real} therefore is dependent on four major phenomena:

$$E_{\text{real}} = E_0 - E_{\text{leak}} - \eta_{\text{act}} - \eta_{\text{ohm}} - \eta_{\text{conc}} \quad (16)$$

The leakage loss E_{leak} is largely caused by sealant or electrolyte imperfections and is noticeable in a voltage drop from the theoretical OCV (see Fig.8). Electrolyte imperfections as such can be porosities or interconnectivities related to the manufacturing process and therefore inevitable. In modern SOFCs the leakage loss can be reduced to the range of a few mV.[5]

The so called activation polarization (or reaction rate loss) η_{act} refers to the losses dominating at low current densities and originate in activation energy necessary for the electrode reactions. They depend on the reactions themselves, the temperature the cell is operated at, the materials used as electro-catalysts and their microstructure, the utilization of the reactants (see chapter 4.2.3.) and of course on the current density.[1]

The region of ohmic polarization (or resistance loss) η_{ohm} is mainly caused by the ohmic and ionic resistance of key cell components such as the electrolyte and electrodes and their interfaces. The losses are proportional to the current density and depend on material selection, geometry of the cell and temperature.[1]

The concentration polarization (or gas transport loss) η_{conc} describes losses related to mass transport kinetics causing insufficient reactant supply for a given current density and are therefore influenced by the flow- and diffusion rates of the reactants. Hence they depend mainly on current density, activity of the reactants and the structure and the surface of the electrodes. The total resistance of the cell is referred to as polarization resistance R_p . [1]

In HT-fuel cells, especially SOFCs, the activation losses are often negligible and thus the concave region of the IV-curve is hard to define. On the other hand the losses caused by inadequate mass transport are much more severe and the convex end of the IV-curve therefore more pronounced.

4.2.3. Cell efficiency

The efficiency of a fuel cell as a fuel converting device is defined by the useful energy generated relative to the change in enthalpy ΔH_R (unit [J/mol]) of the product stream to the educt stream during the reaction.[1] The total electric efficiency therefore is defined as:

$$\eta_{el} = \frac{P_{el}}{\Delta H_R \dot{n}_{fuel}} \quad (17)$$

where P_{el} is the available electric power generated and \dot{n}_{fuel} the molar fuel flow. The total efficiency can further be divided into three different types of efficiencies:

$$\eta_{el} = \eta_{th} \eta_V \eta_{FU} \quad (18)$$

The thermodynamic efficiency η_{th} relates to the electric energy produced in an ideally reversible system versus the available chemical energy. It is linked to the Nernst equation (14) and depends on temperature, pressure and composition of the fuel.[8] Further as seen from the nature of equation (19) η_{th} decreases with increasing temperature

$$\eta_{th} = \frac{\Delta G_R}{\Delta H_R} = 1 - \frac{T \Delta S}{\Delta H_R} \quad (19)$$

The voltage efficiency η_V depends on the actual cell voltage U_{cell} with all possible losses discussed in 4.2.2. occurring during operation against the fully reversible Nernst potential $E_0 = U_{Nernst}$. [8]

$$\eta_V = \frac{U_{cell}}{U_{Nernst}} \quad (20)$$

The fuel utilization η_{FU} (or FU) describes the amount of fuel converted in the cell reaction versus the inlet fuel flow. [16] Typically fuel utilizations of around 85% are desired for operation. [15] At higher values the anode oxygen partial pressure increases and causes potential oxidation of the anode material.

$$\eta_{FU} = \frac{\text{rate of fuel conversion}}{\text{rate of fuel supplied}} = 1 - \frac{\dot{m}_{fuel_out}}{\dot{m}_{fuel_in}} \quad (21)$$

Here \dot{m}_{fuel_in} is the inlet massflow at the anode, whereas \dot{m}_{fuel_out} is the outlet massflow. Hence the difference between these two has to be the amount of fuel converted by the fuel cell.

Compared to other sources of power generation, SOFC systems offer high efficiencies over a variable range of power output. A comparison of different combustion-based power plant systems is shown in Fig.9.

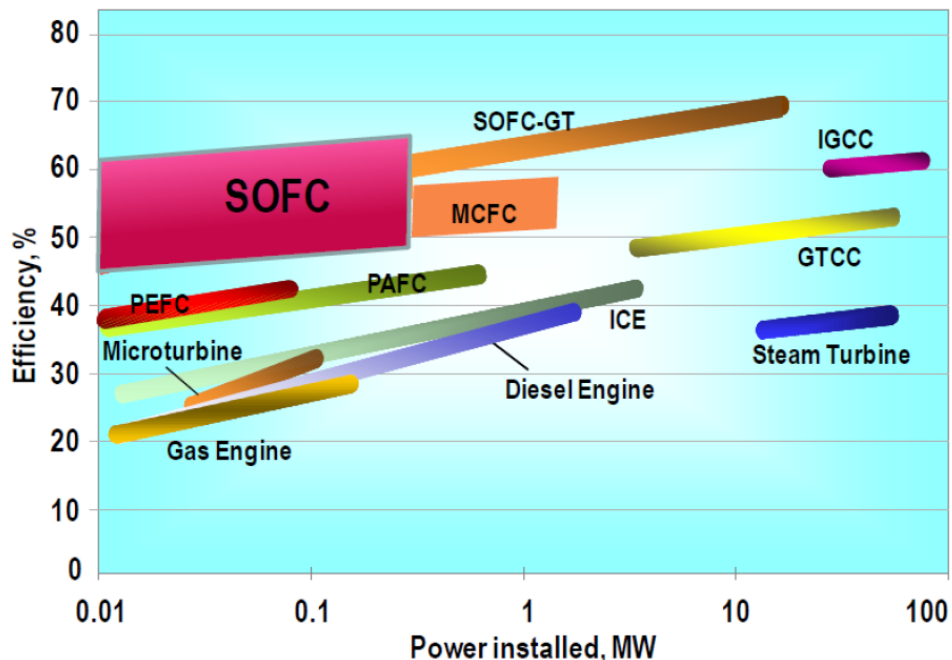


Figure 9: Comparison of combustion based power plant systems regarding efficiency and power output (ICE = internal combustion engine; GTCC = gas turbine combined cycle; IGCC = integrated gasification combined cycle; GT = gas turbine bottoming cycle [17])

4.3. Cell designs

The basic design of a SOFC was already discussed in chapter 4.1. A single SOFC mainly consists of three functional parts: the ceramic electrolyte, which is responsible for the oxide ion conductivity at elevated temperatures, the cathode, which provides oxygen ionization and exchange from the gas phase into the solid material, and the anode, where hydrogen reacts together with oxygen to produce water. The two most common SOFC designs are either the planar or tubular shape of the cell body shown in Fig.10.

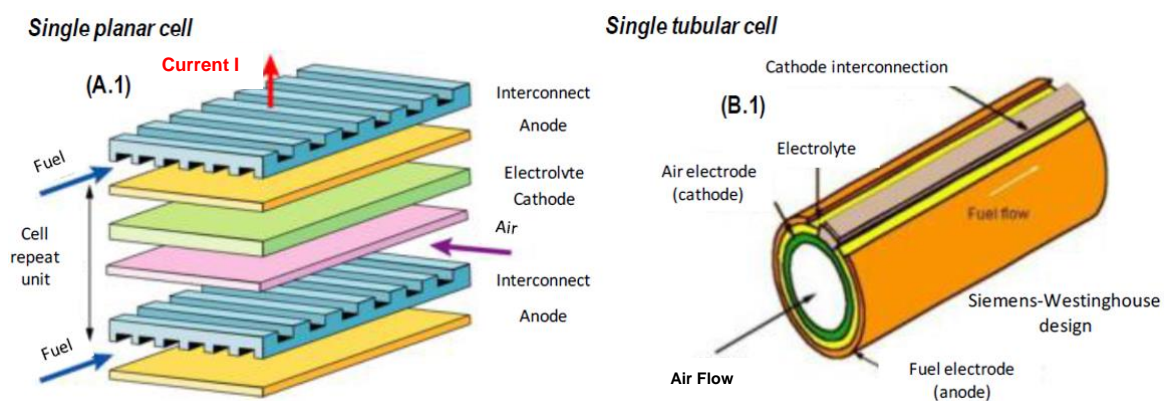


Figure 10: Schematic layout of planar (A.1) and tubular (B.1) SOFCs[18]

In order to increase the power output of a fuel cell system, usually numerous single cells are joined together to a fuel cell stack. For APU operation multiple stacks from different manufacturers incorporating planar cells are used. The stacks count up to 60 cells per stack at around 100cm² of active area per cell. Planar cells are commonly stacked on top of each other and connected serially, while tubular cells are often connected in a hybrid of serial and parallel configuration to reduce power drop in case of a single tube failure.[8]

Additional key components for stack manufacturing are interconnectors (IC) (see Fig.10, A.1) between the single cells providing electric conductivity and homogeneous gas supply to the active surface of the cell. In planar stacks with serial connectivity of the single cells interconnectors are implemented as bipolar plates or separators emphasizing the different polarities of the anode and the cathode. Their shape and material choice depend mainly on the stack design and its intended operating environment and temperature. Common materials for ICs are ceramic perovskites for high temperature operation or metal alloys for lower temperature applications.[1]

4.3.1. Planar SOFCs

Planar SOFCs have a stratified layout shown in Fig.10. The design evolved from an electrolyte supported cell (ESC) over an anode support (ASC) to metal supported cells (MSC) configuration (see Fig.11) named after the supporting layer, which provides the structural integrity of the cell. MSCs use a porous steel substrate plate, whereas ASCs are based on the ceramic anode layer, onto which the active layers are applied subsequently. Using steel as supporting material offers advantages regarding production effort, structural integrity and costs compared to ASCs, which make this layout a promising design for upcoming SOFCs.[19]

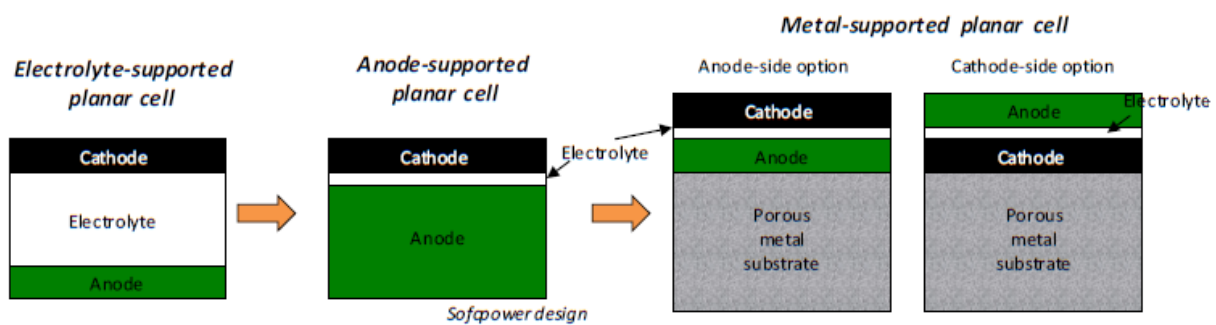


Figure 11: Evolution of the planar solid oxide fuel cell design[5]

Planar cells in general are relatively easy to manufacture and integrate into a multiple cell stack and offer high power densities. The main challenge is gas tightness throughout its wide range of operating temperature, where high temperature glass solder sealant is used, and the mechanical stability of the cell at temperatures up to 1000°C.

In the extent of this thesis planar metal supported single cells manufactured by Plansee SE were used.

4.3.2. Tubular SOFCs

The tubular SOFC design was initially developed by Siemens. Because of the tubular layout there is no need for high temperature sealant, which makes this type of cells easy to seal and therefore more stable during operation under thermal cycles. However the power density is lower compared to planar SOFCs and the manufacturing processes are more complicated, which limits the commercialization of tubular cells. There is nevertheless the prospect of reducing the tube diameter of the cell down to nanoscale, which leads to more competitive power densities.[1]

4.4. Materials and manufacturing

As a matter of fact planar fuel cells currently are more widely used in SOFC applications. The following chapters will primarily focus on this design. Furthermore due to the contemporary developments of metal supported solid oxide fuel cells, which offer strategic advantages compared to SOFCs comprising only ceramic materials, a more in depth look into material selection and manufacturing is taken.

4.4.1. Cell fabrication

As briefly mentioned in 4.3.1., the latest generation of MSCs are built onto a porous ferritic steel backbone, which offers benefits regarding structural integrity, production effort and costs. Nevertheless the fabrication process still remains a complex procedure consisting of multiple crucial steps utilizing a variety of manufacturing techniques in order to achieve maximum cell performances at a reasonable price point. Fig.12 shows the different steps and the manufacturing techniques used in a state-of-the-art MSC production performed by Plansee.

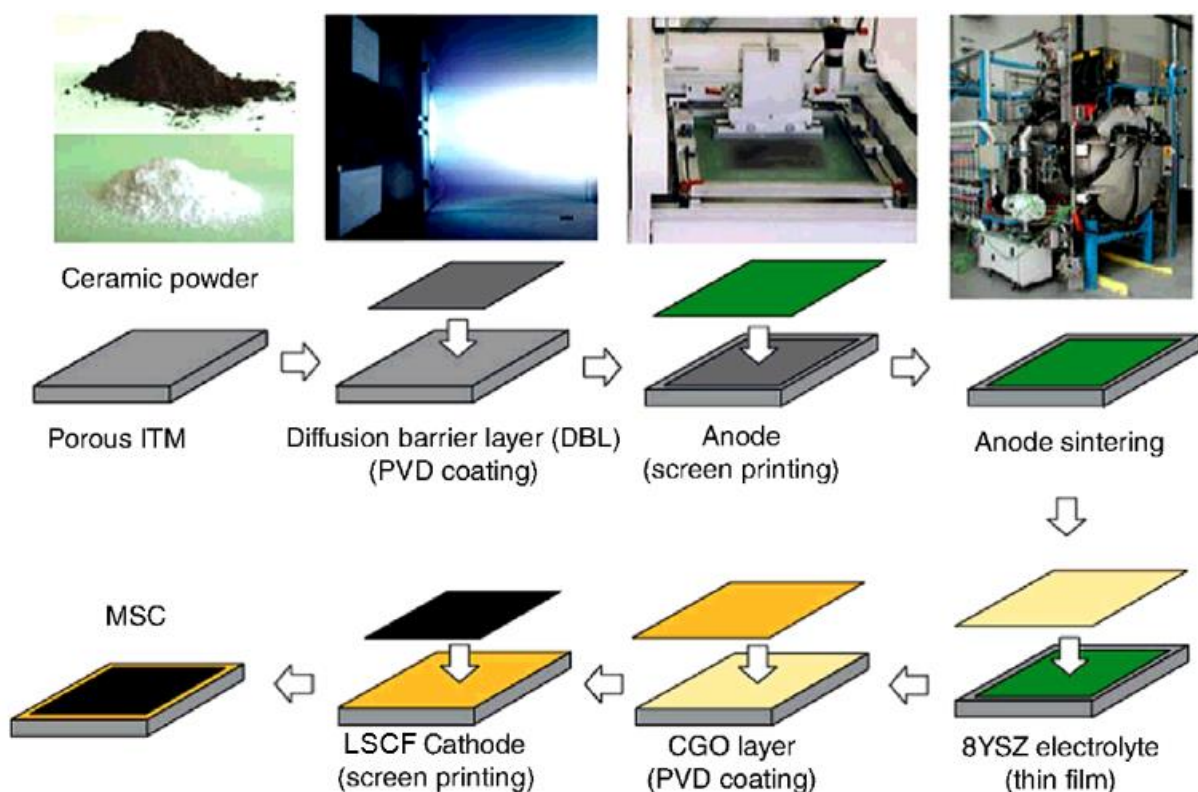


Figure 12: Fabrication cycle of a MSC developed by Plansee (ITM = intermediate temperature metal; DBL = diffusion barrier layer; PVD = physical vapor deposition; YSZ = yttria stabilized zirconia; CGO = cerium gadolinium oxide; LSCF = lanthanum strontium cobalt ferrite oxide)[20]

Thus the obvious complexity in the manufacturing of a MSC arises from the need of multiple functional layers to be bonded together, each demanding different conditions (atmospheres and temperatures) and techniques for their application.[19] The different functional layers including the manufacturing steps and challenges evoked by them are described in Table 5.[20-24]

Table 5: Functionality and processing of the different layers of a state-of-the-art MSC

Layer	Purpose	Manufacturing requirements
Substrate (ITM-alloy)	backbone of the cell, porosities required for gas permeability by the fuel	sintering of porous metal powder needs to be done in reducing conditions and temperatures below 1200°C due to segregation and melting at temperatures above
Diffusion barrier layer (DBL)	prevents counter diffusion of Fe and Ni between anode and substrate	applied by physical vapor deposition (PVD) in vacuum
Anode (Ni-YSZ)	provides catalytic activity for electrochemical reactions and fuel processing	screen printed on top of DBL covering and substrate and DBL filling pores to minimize undulations at the interface, subsequent sintering under reducing atmospheres and temperatures above intended operating temperature
Electrolyte (8YSZ)	oxygen ion conductivity at operating temperature and electric and gas-tight isolation	thin film application by tape casting, cofiring together with support in hydrogen/argon atmosphere above 1000°C
Diffusion barrier layer (CGO)	inhibits counter diffusion of Zr and La between electrolyte and cathode	application via reactive pulsed DC magnetron sputtering (PVD) under vacuum/argon atmospheres
Cathode (LSCF)	oxygen exchange and ionization, oxygen ion conductivity	screen printed on top of barrier layer, drying and successive firing above operating temperature

Additionally to the overview in Table 5 a more detailed perspective of the most important functional layers and the substrate focusing on MSC design is explained in the following chapters.

4.4.2. Substrate

For modern MSCs, as mentioned above, ferritic steels are used as porous substrates for the cell build up. Usually stainless steels with different Cr quantities are used. The crucial parameter for the substrate material however is its coefficient of thermal expansion (CTE), which has to match the ones of the ceramic functional layers of the cell, in order to minimize stresses occurring at elevated operating temperatures. CTEs of around 10-12 ppm/K are desired.[19] Other key requirements for the substrate are high electric conductivity, corrosion resistance in oxidizing, reducing and moist atmospheres, mechanical stability, gas permeability (porosity > 40 vol%), a flat surface area for the following application of the functional layers and of course all that at a reasonable price.[25] Different substrate materials currently used for MSC fabrication are listed in Table 14 (see chapter 15. Appendix).

4.4.3. Electrolyte

The main demand on the electrolyte is oxygen ion conductivity from the cathode to the anode side. Apart from the desired high ionic conductivity at SOFC operating temperatures, other characteristics such as electronic isolation, thermal, mechanical and chemical stability in oxidizing and reducing environments and in contact with surrounding materials, gas tight manufacturability and of course economic production and availability.[16]

Today the material of choice for SOFC electrolytes is yttrium stabilized zirconia (YSZ) due to its high ionic and low electronic conductivity. However research towards alternative materials like gadolinium doped ceria (GDC) or lanthanum strontium gallium magnesium oxide (LSGM) become more and more important due to their enhanced ion conductivity at lower temperatures in the range of 500°C to 700°C emphasizing the development of IT-SOFCs.[26-29] Pure zirconia (ZrO_2) undergoes a phase transition from monoclinic (room temperature) to tetragonal (above 1173°C) to cubic (from 2370°C until the melting point at 2690°C).[30]

To maintain the desired cubic phase down to room temperature and increase the oxygen vacancy concentration and hence the ion conductivity σ_O , yttria Y^{3+} (or Ca^{2+} , Ce^{4+} , Sc^{3+}) to the ZrO_2 phase, the enhancement of the oxygen vacancy formation through doping can be described using the Kröger-Vink notation:[31]



contributing to the amplified oxygen ion conductivity σ_O [8]

$$\sigma_O = 2 F [V^{\bullet\bullet}_O] \mu_O \quad (23)$$

where Y'_{Zr} stands for a Y-ion occupying a Zr-lattice site with negative relative charge, O^x_O represents an O-ion on an O-site with neutral charge and $V^{\bullet\bullet}_O$ an oxygen vacancy with double positive charge and $[V^{\bullet\bullet}_O]$ its concentration and μ_O as ionic mobility. For application in SOFCs doping concentrations of 8 mol% (8YSZ) are common due to the maximum ion conductivity at this doping level.[32]

4.4.4. Anode

The anode material of a SOFC has to fulfill a variety of different demands, such as: high electric and ionic conductivity combined with catalytic activity for electrochemical reactions and fuel processing, porosity for gas permeability, stability during redox and thermal cycles, chemical stability against adjacent materials, matching CTE with other cell materials and last but not least affordability.[33] Especially porosity is crucial for anode materials, hence in order to maximize fuel oxidation, high TPB-concentrations are required.

Ceramic-metal catalysts and composites provide a wide range of these demands, making nickel-zirconia cermets extensively used as state-of-the-art anodes for SOFCs. Nickel is an excellent catalyst material used for hydrogen oxidation in steam reforming processes and electric conductivity. The mixing of nickel with ion conducting electrolyte materials (see 4.4.3.) compensates for its CTE mismatch and provoke the extension of TPB across the anode.[34] Commonly nickel cermets contain at least 30 vol% of Ni to enhance electric conductivity.[35] On the downside nickel is highly susceptible to deactivation by sulfur and carbon deposition during internal fuel reforming.

4.4.5. Cathode

The requirements for the cathode materials for ordinary operation are somewhat similar to the ones of the anode, however the oxygen electrode of course has to be stable in oxidizing atmospheres throughout its application range. Further demands are likewise high electric conductivity (preferably above 100 S/cm in oxidizing atmospheres), mixed electronic and ionic conductivity, high catalytic activity, matching CTE and chemical compatibility with the other layers, porosity and all that together at low costs.[36]

There are two cathode design approaches in order to maximize the activity, namely the use of:

- (a) porous composites of an electronic conducting cathode mixed with an ionic conducting electrolyte material and
- (b) single-phase mixed ionic electronic conductors (MIECs) offering both oxide ion and electron mobility.[5]

In state-of-the-art SOFCs perovskite oxides with the chemical formula ABO_3 are the material of choice for the oxygen electrode material. Lanthanum cobaltite and ferrite cathodes are widely used, with $La_ySr_{1-y}Co_xFe_{1-x}O_{3-\delta}$ (LSCF) being the most commonly seen MIEC for IT-SOFC application.[36] However at present research is carried out with many different perovskite type oxide materials (see Table 15, chapter 15. Appendix). Five of the most common cathode materials and their important properties are listed in Table 6.

Table 6: Most common perovskite materials used in SOFCs (CTEs of electrolytes are usually 10-12ppm/K; σ_e =electronic conductivity, σ_i =ionic conductivity)[5]

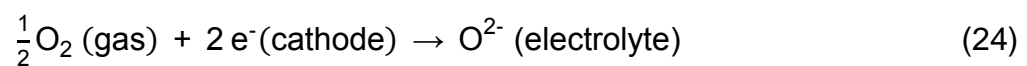
Composition	CTE (ppm/K)	T (°C)	σ_e (S/cm)	σ_i (S/cm)	REF.
$La_{0.8}Sr_{0.2}MnO_3$	11.8	900	300	$5.93 \cdot 10^{-7}$	[37]
$La_{0.6}Sr_{0.4}CoO_3$	20.5	800	1600	0.22	[38,39]
$La_{0.8}Sr_{0.2}FeO_3$	16.3	800	129	$5.6 \cdot 10^{-3}$	[38]
$La_{0.6}Sr_{0.4}Co_{0.2}Fe_{0.8}O_3$	15.3	600	330	$8 \cdot 10^{-3}$	[38,40]
$LaNi_{0.6}Fe_{0.4}O_3$	11.4	800	580	-	[41]

5. SOFC cathode materials

As previously mentioned various oxides with perovskite type structure are used as cathode materials for SOFC application due to their high electron and ion mobility. Because the focus of this thesis lays on the behavior of the cathode material under certain circumstances a more in depth look at the reaction mechanisms occurring at a cathode and further the properties and demands for a cathode material is taken.

5.1. Reaction mechanisms and kinetics

The ionization of the oxygen molecules is described by the oxygen reduction reaction (ORR), which takes place on the surface of the cathode:



This reaction convolutes three different types of transport mechanisms: the ionic conductivity of the electrolyte, the electronic conductivity of the cathode and the convective oxygen transport within the gas phase. Therefore it is promoted in the areas around the TPB on the cathode side illustrated in Fig.13.

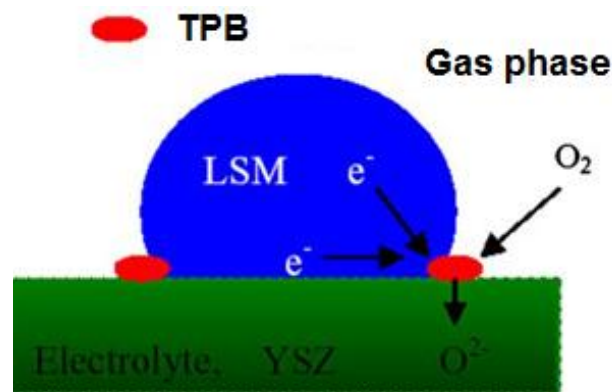


Figure 13: Schematic of the cathode side triple phase boundary (TPB)[36]

The overall electrode reaction can thus be broken down to the following elementary reactions: (1) reduction of O_2 molecules covering adsorption, dissociation, reduction and incorporation of the resulting anion into the cathode materials lattice structure; (2) ionic diffusion through the cathode material to the electrolyte interface; (3) ion jumping from cathode to electrolyte lattice.[42,43] Among these different steps the oxygen reduction is the biggest contributor to the total cell resistance. Therefore an increase in catalytic activity of the cathode material has a big and decisive impact on overall cell performance.[44,45]

Regarding porous electron conducting perovskite materials there are three possible paths for the cathode reaction (equation 24): the electrode surface path, the bulk path and the electrolyte surface path all shown in Fig.14.[46]

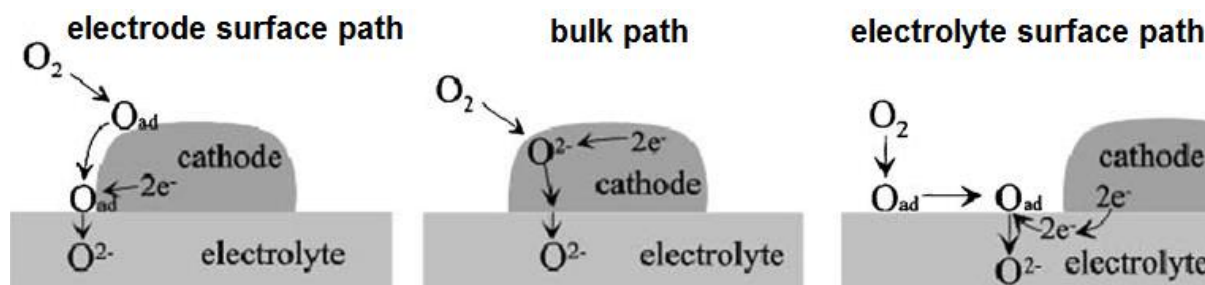


Figure 14: Mechanisms of three different reaction paths for the oxygen reduction at a porous SOFC cathode[46]

This description of the oxygen reduction is suitable for MIECs such as e.g. LSCF. The total ORR can occur as a simultaneous combination of these three mechanisms, whereas each single step determines the combined reaction rate. Hence the cathode geometry (e.g. porosity, tortuosity) and its interface with the electrolyte have a big impact on cathode performance and further on overall cell performance.

5.2. Perovskite materials

In order to choose an appropriate material for cathode application in a SOFC a better understanding of the basic perovskite structure is necessary. As mentioned above a perovskite oxide unit cell has the layout ABO_3 , where A and B indicate two different cations with a combined charge of +6. The A-site usually is occupied by larger, lower valence cations (e.g. La, Sr, Ca, Pb, etc.) coordinated to 12 oxygen anions, whereas the B-site is taken by smaller 6-coordinated cations (e.g. Ti, Cr, Ni, Fe, Co, Zr, etc.).[47] The structure of a cubic perovskite is shown in Fig.15.

In order to tweak physical properties (e.g. electronic and ionic conductivity, catalytic activity and CTE) full or partial substitution of A or B with cations of different valence is possible. For SOFC cathodes the A-site is usually occupied by a mixture of rare earth metals (commonly La) and alkaline earth metals (such as Sr, Ca and Ba), while the B-site is filled with one or various mixed-valence transition metals (such as Mn, Co, Fe and Ni) providing the catalytic activity for the ORR (equation 24).[48]

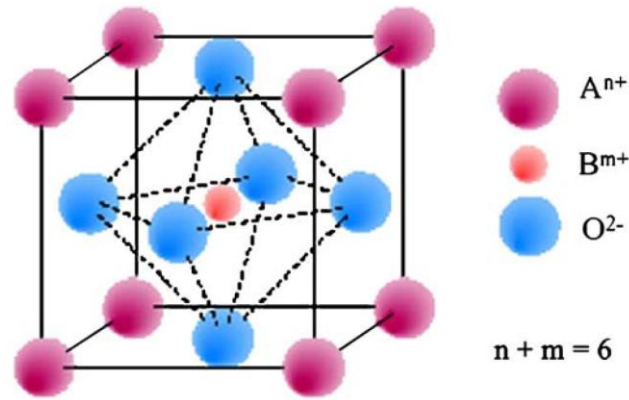


Figure 15: Unit cell layout of an ideal ABO_3 perovskite structure[49]

In reality many perovskite materials are distorted and therefore differ from the ideal cubic structure shown in Fig.15. The distortions are related to proportion of the radii of the A- and B-elements and in further regard to a possible substitution of the A- and B-site cations with different atoms with different properties and therefore can result in cation displacement or tilting of the octahedra.[36] To quantify the level of distortion and further give information about the stability of a perovskite the Goldschmidt tolerance factor t is introduced:

$$t = \frac{r_A + r_B}{\sqrt{2}(r_B + r_O)} \quad (25)$$

where r_A , r_B and r_O represent the effective radii of the A-, B- and O-ions. For an ideal cubic structure this factor is 1, whereas stable perovskite structures are predicted for $0.77 \leq t \leq 1.00$. For $t > 1$ the hexagonal structures tend to be stable, while for $t < 1$ the cubic structure changes first to rhombohedral and then to orthorhombic.[50]

The substitution of A- and/or B-site atoms with aliovalent cations further evokes two different compensation mechanisms to maintain overall charge neutrality: in case of ionic compensation in acceptors (see chapter 5.4.) oxygen vacancies are induced into the lattice, which promotes oxygen bulk transport and therefore ionic conductivity. On the other hand in case of electronic compensation the B^{n+} -ions are either oxidized or reduced, which influences the electronic properties of the material. Furthermore temperature and oxygen partial pressure affect the oxidation state and oxygen vacancy concentration of the perovskite, which has a profound effect on the transport mechanisms required in case of a SOFC cathode material.[31,36]

5.3. Oxygen ion transport in perovskite oxides

As indicated above perovskite materials show a wide variety of physiochemical properties relevant for SOFC application, such as catalytic activity, ionic and mixed conductivity. As a cathode material the oxygen ion diffusion and its dependency on different parameters like temperature, oxygen partial pressure and type as well as degree of substitution of A- and B-site cations is of great interest.

5.3.1. Definition of diffusion coefficient

The oxygen flux J_O through a material is driven by a gradient of the oxygen concentration c_O and further described by Fick's first law:

$$\vec{J}_O = -D \cdot \vec{\nabla} c_O \quad (26)$$

where D is defined as the oxygen self-diffusion coefficient. The continuity equation in small elements leads to Fick's second law:

$$\frac{dc_O}{dt} = \nabla \vec{J}_O = -D \cdot \nabla^2 c_O - \bar{v} \cdot c_O \quad (27)$$

where \bar{v} indicates a present drift field velocity induced by either a chemical or electrical field. In presence of a chemical field equation (27) can be simplified according to Philibert [51]:

$$\frac{dc_O}{dt} = -D_{\text{chem}} \cdot \nabla^2 c_O \quad (28)$$

where D_{chem} is the chemical diffusion coefficient related to the self-diffusion coefficient by the thermodynamic enhancement factor.[47]

5.3.2. Oxygen tracer diffusion coefficient

The self-diffusion coefficient can be determined by the measurement of the oxygen tracer diffusion coefficient D^* including a correlation factor f , which represents the deviation from a random jump pattern of the oxygen ions ($f \approx 1$).

$$D^* = f D \quad (29)$$

Regarding a material with oxygen deficiency resulting from mobile oxygen vacancies, D^* can be deviated from the random walk theory:

$$D^* = \beta [V_{\text{O}}^{\bullet\bullet}] a_0^2 v_0 \exp\left(-\frac{\Delta H_m}{RT}\right) \quad (30)$$

with

$$\beta = \frac{z}{6} f \exp\left(\frac{\Delta S_m}{R}\right) \quad (31)$$

and further defining the vacancy diffusion coefficient D_V as

$$D_V = \beta a_0^2 v_0 \exp\left(-\frac{\Delta H_m}{RT}\right) \quad (32)$$

the oxygen self-diffusion coefficient can be simplified as

$$D^* = [V_{\text{O}}^{\bullet\bullet}] D_V \quad (33)$$

where $[V_{\text{O}}^{\bullet\bullet}]$ in this case represents the mobile vacancy concentration, a_0 is defined as the distance between equal sites, z is the number of equal near neighbor sites and $v_0 \exp\left(-\frac{\Delta H_m}{RT}\right)$ is the jump frequency for the migrating ion with ΔH_m and ΔS_m referring to its enthalpy and entropy.

The vacancy diffusion coefficient therefore contains all relevant terms concerning the mobility of the vacancies and hence the effort required for an oxygen ion to jump from a lattice point to a neighboring vacancy during its diffusion process through a solid material.[47]

5.3.3. Surface exchange coefficient

For perovskites as cathode materials the oxygen surface exchange coefficient k is yet another crucial kinetic parameter contributing to the overall oxygen transport. It is defined by the oxygen exchange flux across the oxide surface at equilibrium[52]:



with

$$k = \frac{J_{\text{O}}}{[\text{O}]} \quad (35)$$

The oxygen exchange coefficient k is the ratio between the netto oxygen flux from the gas phase to the solid J_O and the total oxygen concentration in the surrounding atmosphere $[O]$, whilst the total exchange flux further depends on the vacancy and electron concentration at the surface and the rate of dissociation of the oxygen molecule, with the surface vacancy concentration having the biggest impact on the exchange kinetics.[52]

5.3.4. Defect chemistry of perovskite oxides

As mentioned in 5.2., the materials used for SOFC cathodes are usually 3,3-perovskite oxides with the basic formula $A^{3+}B^{3+}O_3$ with the A-site most commonly occupied by lanthanum acceptor doped with strontium and complementary a transition metal (mostly Co, Fe or Mn) on the B-site. These materials show a large variety of stoichiometry, ranging from hypostoichiometric to hyperstoichiometric and therefore their electrical and ion-conducting properties can be tweaked by different types of doping.[47]

The non-trivial defect structure results in a number of simultaneous defect equilibria leading to the different conducting mechanisms. First the intrinsic defect processes for a mixed conducting oxide with the structure $La_{1-x}Sr_xBO_{3\pm\delta}$ are evaluated, which experiences Schottky disorder in combination with intrinsic electronic disorder according to De Souza et al. [53]:



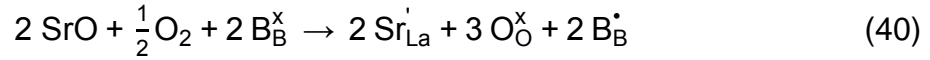
where e' represents a free electron (with negative charge) and h^\bullet a complementary hole (with positive charge). The dissociation of the effectively neutral B-site cation into two charged states according to equation (37) can be rewritten as:



The redox processes happening in the lattice of perovskites with variable valent B-site cations can be described at first by the oxidation of the lattice leading to regions of oxygen excess, where cation vacancies can form[54]:



In this oxygen rich environment the formation of B-site cation vacancies consequently decreases the oxygen vacancy concentration vastly according to the Schottky equilibrium. This effect can be compensated by either an electronic or a vacancy mechanism or the combination of both:



The combination of all possible defect types then forms the neutrality condition:

$$3 [\text{V}'_{\text{La}}] + 3 [\text{V}''_{\text{B}}] + [\text{Sr}'_{\text{La}}] + [\text{B}'_{\text{B}}] = 2 [\text{V}^{\bullet\bullet}_{\text{O}}] + [\text{B}'_{\text{B}}] \quad (42)$$

In order to illustrate the concentration of these defect types in a solid material over different oxygen partial pressures, a Brouwer diagram is constructed:

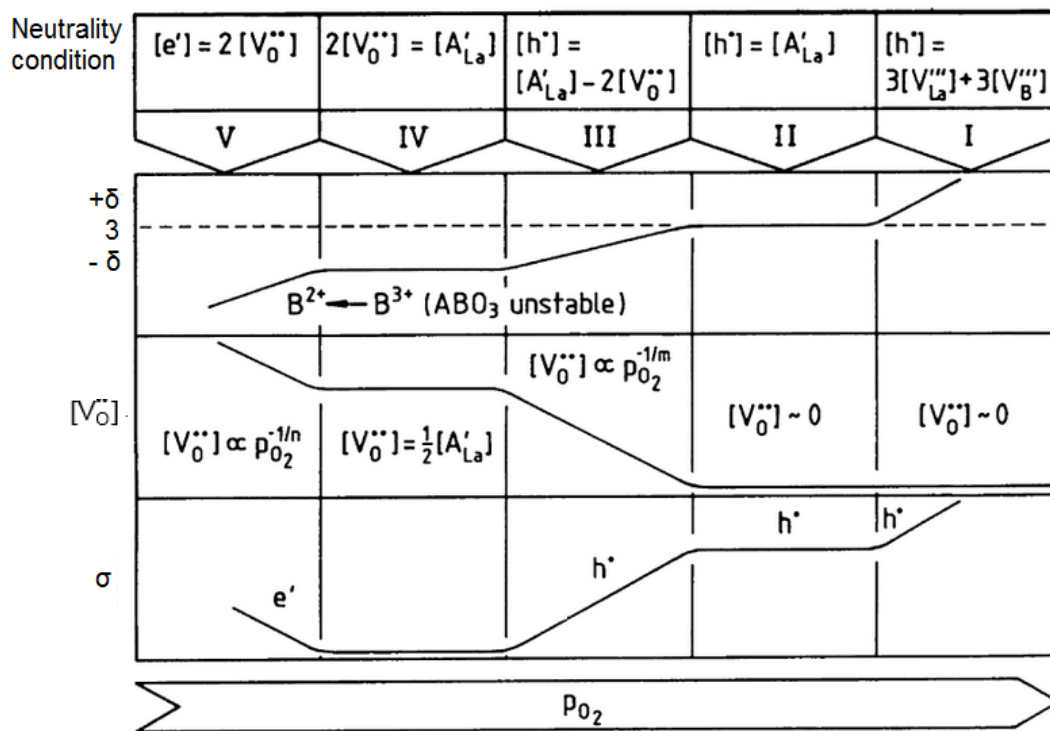


Figure 16: Brouwer diagram for an acceptor doped $\text{La}_{1-y}\text{A}_y\text{BO}_{3\pm\delta}$ showing five different regions of oxygen content δ with their corresponding oxygen vacancy concentration $[\text{V}_\text{O}^{\bullet\bullet}]$ and electronic conductivity σ as a function of the oxygen partial pressure p_{O_2} [55]

To explain the relations shown in Fig.16 some approximations have to be defined according to Ishihara [47]. Starting from high partial pressures first the hyperstoichiometric region I with $\delta > 0$ has to be considered, which shows p-type conductivity through electron holes h^\bullet at the B-sites and an oxygen vacancy concentration of about 0. Therefore the following neutrality equation is valid:

$$3 [V_{La}^{\bullet\bullet}] + 3 [V_B^{\bullet\bullet}] = [B_B^\bullet] = [h^\bullet] \quad (43)$$

It is followed by the stoichiometric region II, where the material behaves like a controlled valence p-type semiconductor with $\delta = 0$ and has the following neutrality equation:

$$[Sr_{La}'] = [B_B^\bullet] = [h^\bullet] \quad (44)$$

Next is the region III with both electronic and vacancy compensation. The compensation of the acceptor in perovskite materials does not change abruptly and the material changes to a hypostoichiometric composition. Additionally δ becomes negative and the neutrality condition is defined as:

$$[Sr_{La}'] = 2 [V_O^{\bullet\bullet}] + [B_B^\bullet] = [h^\bullet] \quad (45)$$

Further the material becomes vacancy compensated exclusively in region IV with a fixed $\delta = -x/2$ and hence a constant $[V_O^{\bullet\bullet}]$.

$$[Sr_{La}'] = 2 [V_O^{\bullet\bullet}] \quad (46)$$

In the end the material gets reduced in region IV and oxygen vacancies in combination with free electrons emerge. The electronic conductivity is now fully n-type with e' only.

$$[B_B^\bullet] = [e'] = 2 [V_O^{\bullet\bullet}] \quad (47)$$

The materials used for IT-SOFC application (e.g. lanthanum ferro-cobaltites as LSCF) are meant to be in the mixed compensation region III operated at high oxygen partial pressures and $-x/2 \geq \delta \geq 0$. These high oxygen vacancy concentrations lead to enhanced oxygen diffusivity under normal operating conditions.[47]

5.4. Influences on diffusivity in MIECs

As defined above, the electrochemical properties of mixed ionic electronic conducting perovskite oxides can be tweaked throughout a broad range by both A- and B-site substitution (doping). Therefore many different combinations of different elements for the occupation and substitution of the A- and B-sites are possible.

5.4.1. Effect of A-site cation

There are two possible types of A-site cation substitution in the perovskite structure: aliovalent and isovalent doping. Aliovalent doping refers to the replacement of the host cation by a substituting ion with different oxidation state, hence introducing effective charges. In order to keep electrical neutrality oppositely charged defects are formed by either changing the oxidation state of the B-site cation (electronic compensation) or by the formation of vacancies of opposite charge (ionic compensation).

Isovalent doping on the other hand occurs when the oxidation state of the substituting ion is identical to the host ion. Therefore no charges are introduced into the lattice and no further compensation mechanisms are necessary. Albeit due to the difference in size of the hosting and substituting ion elastic lattice strains are introduced.

For MIECs lanthanum has become the A-site host ion of choice because of its large ionic radius and decent availability. As substitution ions alkaline earth elements (e.g. Sr, Mg and Ca) are favored due to the close size match compared to the lanthanides and thermodynamic stability in SOFC operating environments. In general the desired increase of the oxygen diffusion coefficient can be achieved by increasing the oxygen vacancy concentration by causing ionic compensation.[47]

5.4.2. Effect of B-site cation

In chapter 5.3.4. it is shown that the nature of the B-site cation determines which neutrality condition is valid for a specific MIEC (see Fig.16). As B-site materials transition metals from group 4 (such as Mn, Fe, Co or Ni) are commonly used in MIECs. The use of cobalt as both B-site host cation and substitute has become popular because of its influence on the oxygen tracer diffusion coefficient due to

large oxygen hypostoichiometry (region III in Fig.17).[56] Further the surface exchange coefficient increases significantly with a growing B-site Co-content shown in Fig.17 using of cobalt doped $\text{La}_{0.8}\text{Sr}_{0.2}\text{MnO}_{3\pm\delta}$ exemplary, whilst the A-site ratio of La/Sr is kept constant:

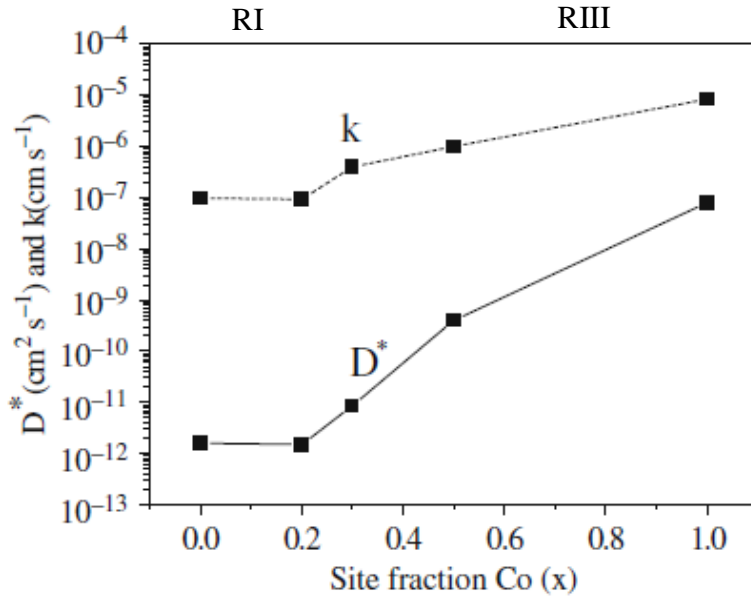


Figure 17: Oxygen tracer diffusion D^* coefficient and surface exchange coefficient k of $\text{La}_{0.8}\text{Sr}_{0.2}\text{Mn}_{1-x}\text{Co}_x\text{O}_{3\pm\delta}$ as a function of the Cobalt site fraction x at 1000°C[57]

5.4.3. Other influences on oxygen diffusivity

Apart from the material itself there are of course other environmental parameters (e.g. temperature and oxygen pressure) influencing the oxygen transport through a perovskite material. The activation energy E_a for the oxygen ion diffusion further depends on several terms:

$$E_a = \Delta H_m + \Delta H_f + \Delta H_a \quad (48)$$

The enthalpy of vacancy migration ΔH_m influences the vacancy diffusion coefficient D_V (see equation 32), whilst the enthalpy of vacancy formation ΔH_f affects the stoichiometric vacancy concentration and ΔH_a is representing the enthalpy of vacancy-dopant association influences the mobile vacancy concentration.[47] In general the oxygen diffusivity profits from increasing temperature, consequently E_a estimated from Arrhenius plots of the diffusion coefficient decreases, with its quantity strongly depending on the composition and level of doping of the perovskite material. Further the oxygen diffusivity decreases with increasing oxygen partial pressure at a constant temperature according to Benson [58].

5.5. LSCF as cathode material for SOFCs

Ferro-cobaltite materials ($\text{La}_y\text{Sr}_{1-y}\text{Co}_x\text{Fe}_{1-x}\text{O}_{3-\delta}$) with different levels of both A- and B-site substitution are widely used as cathode materials in state-of-the-art IT-SOFCs. The reason being their good electrical conductivity combined with high oxygen surface exchange and self-diffusion coefficients especially at temperatures between 600°C to 800°C. The level of cation substitution, hence the overall composition, can be altered depending on the desired properties, such as CTE and ionic- and electronic conductivity. Fig.18 shows an extended supercell of a possible LSCF perovskite consisting of 8 unit cells (see Fig.15).

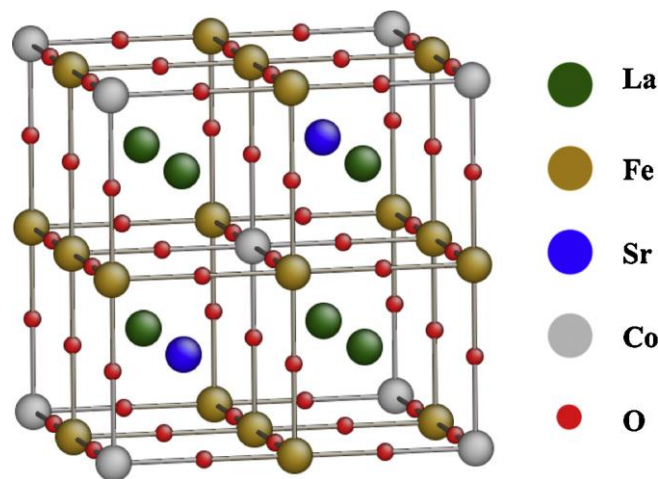


Figure 18: Layout of a 2x2x2 supercell of $\text{La}_{0.75}\text{Sr}_{0.25}\text{Co}_{0.25}\text{Fe}_{0.75}\text{O}_3$ [59]

As for composition there has to be found a compromise between conductive behavior and CTE. The ionic conductivity is generally influenced by the Sr-concentration at the A-site, whereas the electronic conductivity is more dependent on the Co-concentration at the B-site. The value of the CTE can be adjusted by the quantity of Fe added to the perovskite and reaches a minimum at high levels of A-site deficiency and therefore offers a good match with commonly used electrolytes.[36,60] Further the amount of Co within the material dictates the catalytic activity. Additionally a low A-site deficiency in comparison to stoichiometric composition combined with a high Sr-content offers a particularly positive impact on cell performance established by Kilner et al. [31] and Mai et al. [61]. Especially at operating temperatures below 700°C LSCF-type cathodes have the edge over the commonly used HT-SOFC-LSM-materials as a result of a reduced area specific resistance (ASR) and better overall conductivity.

It should further be noted that LSCF-materials are to a certain extent incompatible with YSZ-electrolytes as a result of interface reactions causing the formation of insulating lanthanum zirconate phases ($\text{LZO} = \text{La}_2\text{Zr}_2\text{O}_7$) due to La-diffusion significantly lowering the overall cell performance. Therefore a diffusion barrier layer is required between cathode and electrolyte (see Table 5). However LSCF shows no reactivity with ceria-based electrolytes.[62,63,64]

Although LSCF has more and more become the material of choice as state-of-the-art cathode material in IT-SOFCs, further improvements could be done by, for instance, substituting the A-site La-cation with Pr in multiple valence states. The resulting PSCF-material shows improved conductivities down to operating temperatures well below 700°C .[65] Additionally Ce- and Ba-substituted perovskite materials show a promising perspective in order to lower the operating temperature of IT-SOFCs even further into the 500°C up to 600°C range for applications in so-called *next generation SOFCs*.[66,67]

6. Degradation mechanisms in SOFCs

Solid oxide fuel cells experience a variety of different degradation mechanisms depending on the operating- and environmental conditions. In general degradation can be displayed regarding cell performance as power loss through a decrease in OCV and current- and respectively power-density in combination with a simultaneous increase in area specific resistance over time. As a reference state-of-the-art MSCs undergo a drop in OCV by 4.5% in 1000h of normal operation with 4% moist hydrogen as fuel and air on the cathode side.[19] Fig.19 shows a schematic of cell degradation depending on the physicochemical parameters of the system:

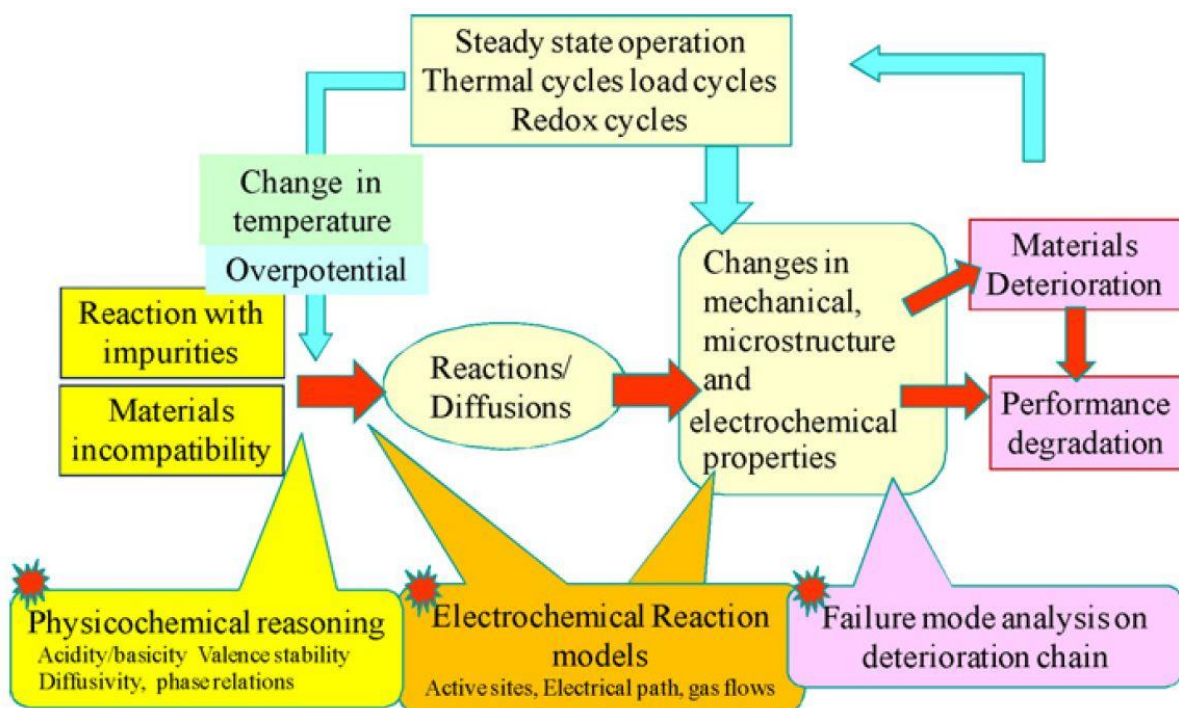


Figure 19: Schematic of degradation phenomena of SOFCs[68]

Measurable degradation/deterioration for failure mode analysis is mostly a result of changes in microstructure and mechanical or electrochemical properties induced by reactions of the cell material with impurities in the media supply and/or incompatibility with other surrounding materials of the system or even between different cell layers (physicochemical reasoning) impacting the electrochemical cell reactions. Aside from performance loss, degradation can also result in mechanical failure of the cell.

6.1. Cathode degradation

Fuel cell degradation is often related to malfunction of the electrodes which are responsible for the exchange of the reaction partners. Mechanisms reducing the cathode performance are of both intrinsic and extrinsic origin and can be categorized as the following [68,69]:

- Coarsening of the microstructure during sintering or at excessively high operating temperatures
- Decomposition of the cathode material (e.g. segregation and diffusion of active elements like La, Sr or Co within the perovskite; decay under highly reducing atmospheres)
- Formation of insulating or chemically inactive phases due to chemical reactions between cathode and electrolyte at their interfaces (e.g. LZO or SZO = SrZrO_3)
- Mechanical failure of the material (e.g. delamination)
- Contamination of surface (e.g. through secondary phases or foreign particles)
- Poisoning of the cathode (e.g. by sulfur or chromium)

All these processes impact the electronic and ionic conductivity and also the catalytic activity of the cathode material and therefore reduce cell performance. Especially contamination of the cathode surface by artifact substances reduces porosity and further the active surface area available, which affects the oxygen exchange process. Moreover the above mentioned effects are dependent on each other as well as environmental parameters (e.g. operating temperature, current density, oxygen partial pressure and presence of other reactive phases in the gas stream).[68]

To understand degradation processes both the extrinsic influence of the operating environment as well as the intrinsic behavior of the material and the interactions between its individual elements have to be considered carefully.

6.2. Degradation of LSCF-based cathode materials

The use of LSCF-type materials as a cathode material for SOFCs offers significant advantages regarding cell performance compared to for instance LSM, especially in the IT-range. However these ferro-cobaltite cathodes show slightly higher degradation rates compared to their manganese-based counterparts.[70,71,72]

Being one of the most reactive alkaline earth metals the segregation and diffusion of Sr inside the cathode is one of the major reasons for degradation in LSCF cathodes. Sr can further react to inactive secondary phases like SrZrO_3 at the electrolyte interface or SrO / SrCO_3 / $\text{Sr}(\text{OH})_2$ on the cathode surface depending on the reaction partner, which then hinder oxygen and electron transport and exchange.[59,71,73]

These mechanisms can be displayed as a change in ASR, particularly the degradation can be assigned to a major increase of the cell polarization resistance combined with small change in ohmic resistance as well.[68] The reason for the increased polarization resistance is an increased A-site deficiency resulting from the Sr-diffusion leading to poorer electrochemical performance of the cell.[74] These Sr-depletion induced degradation mechanisms are strongly dependent on operating parameters like temperature, current density and composition of the gas phase of the cathode stream.

As the objective of this thesis is to characterize the effect of an exhaust gas resulting from the combustion of an ethanol-water mixture on the cathode material, the focus of this study will be laid towards the impact of H_2O and CO_2 on cathode- and cell performance.

6.2.1. Effect of H_2O on cathode performance

As mentioned before the contamination of the cathode-air stream by impurities can influence performance of a SOFC over time. At the forefront of this thesis there have already been some investigations regarding the impact of humidity on electrochemical performance, cathode chemistry and microstructure.

Experiments have shown that in presence of water the polarization resistance of the cathode increases significantly depending on the water content and temperature of the cathode-medium supply stream and exposure time. Fig.20 shows the Nyquist-plots of the impedance spectra of a porous LSCF cathode sample exposed to humidified air with different water content at 600°C measured by the Georgie Institute of Technology[75]. The experiments show an increase of polarization resistance of up to 10% at a water content of 10 vol%.

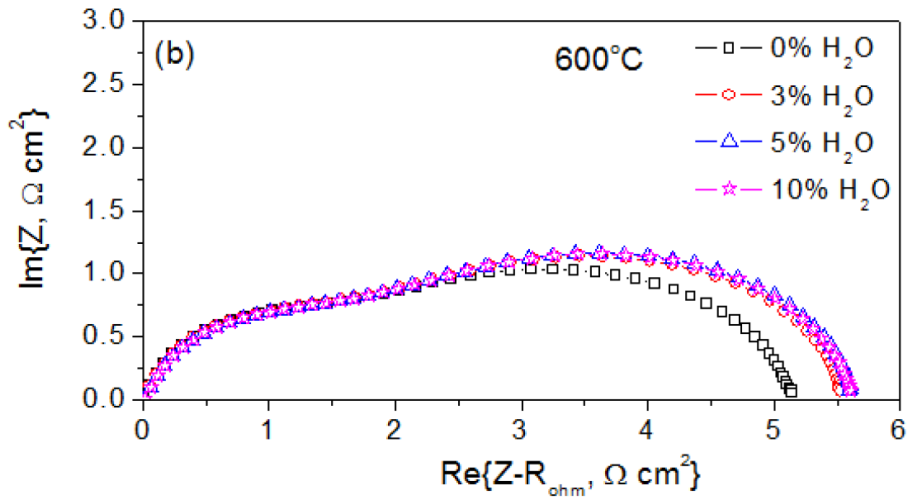


Figure 20: Nyquist-plots of impedance spectra of porous LSCF cathode sample in humidified air with varying water content at 600°C[75]

The plots show a change in resistance in the mid- to low-frequency range on the right-hand side of the spectrum, which according to Hubert et al. [76] relates to surface reactions and bulk solid transport within the electrode. Further experiments at different temperatures show a temperature-dependence of the change in resistance, which is more severe at lower temperatures. Apart from the more spontaneous degradation at lower temperatures the effect reaches a saturation level independent of temperature. Fig.21 compares the increase in polarization resistance depending on the concentration of water between 600°C and 750°C.

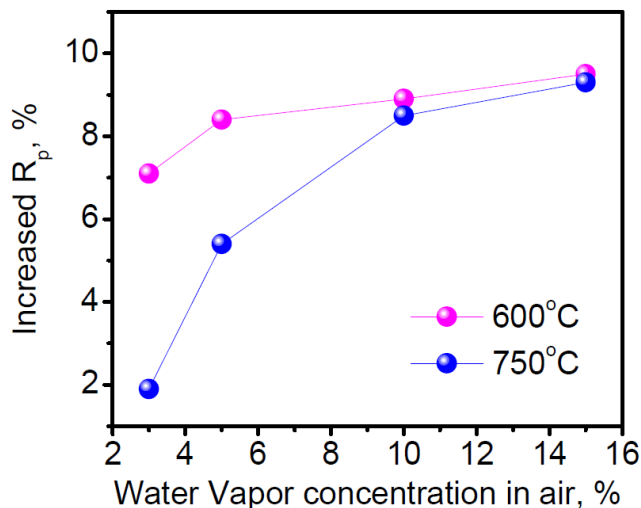


Figure 21: Increase in polarization resistance of LSCF cathode sample depending on concentration of water in air[75]

The degradation therefore does not depend linearly on the water content and shows a more parabolic correlation. Additionally measurements of the cathodic overpotential show that the experienced degradation effect is largely reversible, when switching back and forth between humidified (10 vol% water) and dry air (10 vol% argon). However Fig.22 shows that it takes progressively longer for the material to recover from the water induced contamination effect.

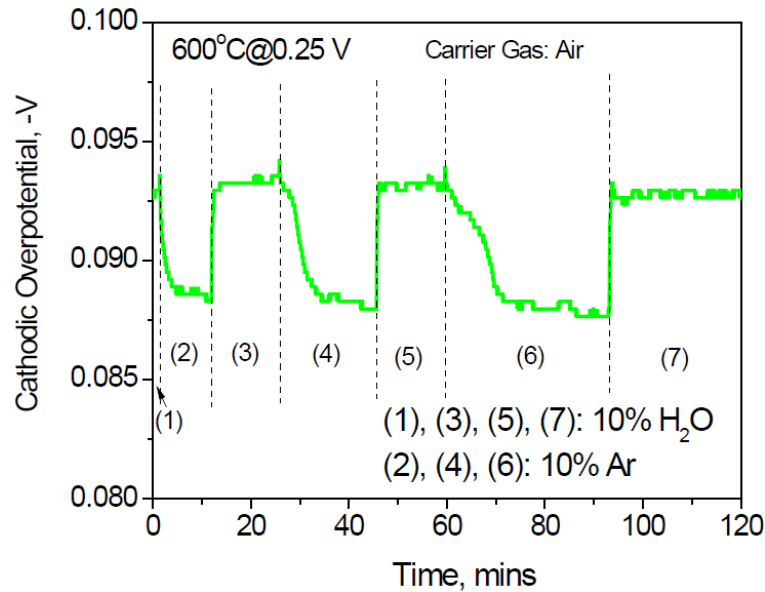
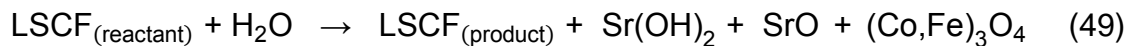


Figure 22: Time dependent cathodic overpotential of LSCF cathode sample when switching between dry (10 vol% argon in air) and humidified (10 vol% water in air) media at 600°C and constant voltage of 0.25V [75]

Research suggests the reason behind this degradation being the formation of secondary phases (e.g. SrO and Sr(OH)₂) as a result of the reaction between adsorbed water and segregated Sr on the surface of the cathode material.



In general water starts to interact with LSCF at temperatures of around 300°C and therefore also takes part in the ORR. The segregation processes within the material are amplified in humid atmospheres and adsorption of water preferably takes place at the active vacancy sites of the LSCF surface. As shown full coverage is more likely to be achieved at lower temperatures. Nevertheless the total adsorption capacity of the material seems to be independent of temperature according to Fig.21. The partial Sr enrichment is further enhanced due to the increase of A-site vacancy formation. The formed oxide- and hydroxide species bond to the Co- and Fe-ions of the lattice,

which affects the valence of these ions. As a result surface vacancy concentration decreases, which slackens the oxygen transport. Furthermore reaction (49) shows, that under the presence of water the formation of minor Fe/Co-rich spinel phases ((Co,Fe)₃O₄) is possible, which due to their different lattice parameters depending on the Fe/Co-ratio can cause an expansion of the material leading to a possible delamination of the cathode over time.[75,77]

6.2.2. Effect of CO₂ on cathode performance

Another concern regarding the stability of cathode materials is the effect of carbon dioxide on performance. Previous studies show a similar increase in polarization resistance of LSCF cathode samples when exposed to CO₂-containing atmospheres compared to the effects of water. Fig.23 shows the percentage of increase in polarization resistance of LSCF depending of the concentration of CO₂ in air at different temperatures.

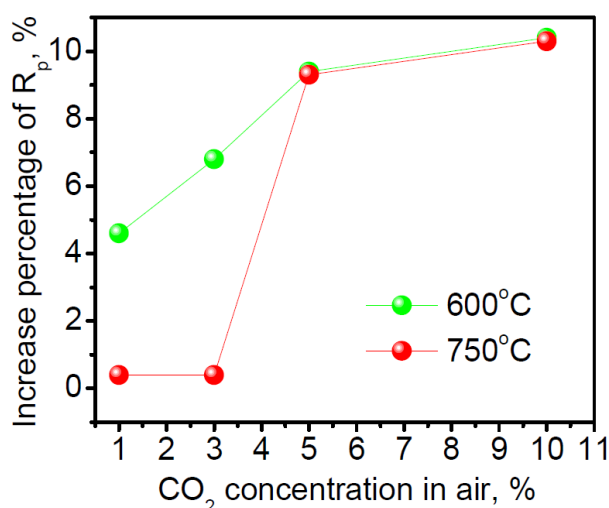
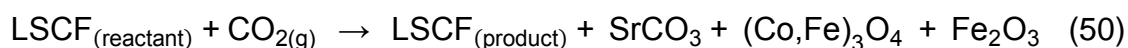


Figure 23: Increase in polarization resistance of LSCF cathode sample depending on concentration of CO₂ in air[75]

Again the effect is more pronounced at lower temperatures and reaches a saturation above 5 vol% CO₂ in air. The mechanism behind this form of degradation being again the formation of secondary phases due to the reaction between the segregated Sr of the LSCF and CO₂ within the air forming SrCO₃ at the surface of the cathode. The Sr-carbonate formation is described in the following reaction:[78,79]



Byproducts of reaction (50) are again a Fe/Co-rich spinel phase ((Co,Fe)₃O₄) and iron(III) oxide (Fe₂O₃). Stability mappings show that the carbonate phase becomes more stable at lower temperatures and higher CO₂ concentrations. Fig.24 shows the amount of SrCO₃ formed per 1 mole LSCF as a function of the carbon dioxide partial pressure at different temperatures. Therefore degradation rates are expected to be even higher at temperatures below 600°C.

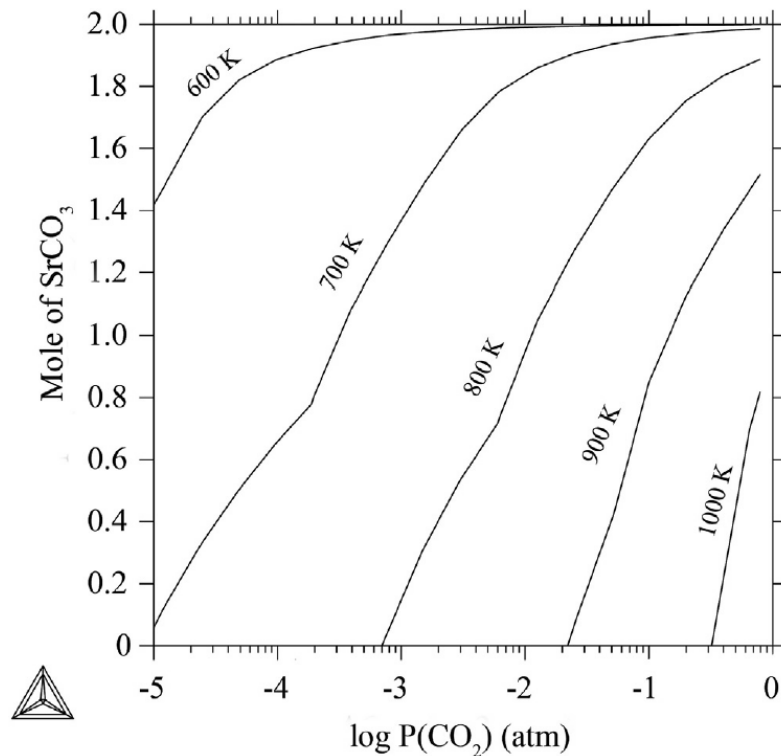


Figure 24: Amount of SrCO₃ formed out of LSCF-6428 depending on p_{CO₂} at different temperatures [78]

The formation of SrCO₃ further leads to a Sr-depletion within the LSCF phase, which affects activity and stability of the bulk material. Additionally the agglomeration of carbonate phases at the surface acts as a diffusion barrier and hence inhibits the surface-to-bulk diffusion flux of oxygen ions by decreasing the active surface area available for the oxygen exchange, which leads to lower overall cell performance. Moreover apart from the temperature the carbonate formation is dependent on both the CO₂- and O₂-partial pressure and reaches a steady state after a certain saturation level of surface phase deposition. Experiments with BSCF (barium strontium cobalt ferrite) cathodes show, that the CO₂-induced contamination effect is reversible until temperatures of 550°C, with a further decrease in temperatures irreversibly affecting cell performance.[36,59,79]

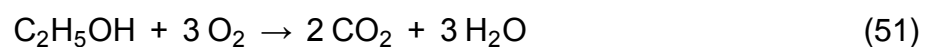
7. Experimental

As initially mentioned the goal of this thesis is to gather knowledge of the behavior of state-of-the-art fuel cells operating in an exhaust gas environment during a heatup procedure. In particular the tolerance of the cathode material exposed to H₂O- and CO₂-containing atmospheres is of potential interest. Therefore single cell tests with MSC samples were carried out with defined anode and cathode gas composition and exposure time, whereas cell temperature was varied between each test and kept constant throughout the duration of each experiment. During testing IV-curves and impedance spectra were monitored. After testing the samples were examined regarding elementary composition and surface topography of the cathode material.

7.1. Testing environment

Per definition the gas to which the cathode material should be exposed during testing has to represent the exhaust gas resulting from the combustion of an ethanol-water mixture. As the experiments were carried out on standardized single cell test beds, where no actual combustion was possible, some boundary conditions and simplifications were set:

- For convenience reasons exhaust gas was a blend of each separate fraction taken from the gas supply (H₂O, CO₂ and air)
- The individual volume flows were calculated under consideration of the chemical equation for gaseous ethanol (C₂H₅OH) combustion:[80]



- E45 (mixture of 45vol% ethanol with water) was used as fuel resembling bioethanol
- Reaction (51) takes place under lean conditions with $\lambda=3$, hence no formation of CO is occurring[81]
- Excess oxygen, nitrogen and water are treated as inert-gases not participating in reaction (51)
- Total O₂/N₂-mixture in product stream was substituted by normal air at test bed due to ease of operation
- Cathode volume flows were normalized to 40 NI/h per single cell

As a result the composition of the cathode gas flow during exhaust gas exposure was determined as the following:

Table 7: Gas fractions of calculated exhaust gas for exposure to cell cathode

Mole fractions	[mol-frac.]	Mass flows	[g/s]	Volume flows	[NI/h]
x_{CO_2}	0.041	m_{CO_2}	3.24	$V_{c_CO_2}$	1.65
x_{H_2O}	0.144	m_{H_2O}	4.62	$V_{c_H_2O}$	5.75
x_{Air}	0.815	m_{Air}	41.96	V_{c_Air}	32.60
Σ	1	m_{tot}	49.82	V_{c_tot}	40.00

The anode line gas composition during operation was chosen as a mixture of H_2 , H_2O and N_2 to represent a possible reformat gas resulting in the decomposition of E45 aquanol fuel and normalized to 20NI/h for a single cell:

Table 8: Gas fractions for cell anode during operation

Mole fractions	[mol-frac.]	Mass flows	[g/s]	Volume flows	[NI/h]
x_{H_2}	0.30	m_{H_2}	0.54	$V_{a_H_2}$	6.00
x_{H_2O}	0.15	m_{H_2O}	2.41	$V_{a_H_2O}$	3.00
x_{N_2}	0.55	m_{N_2}	11.48	$V_{a_N_2}$	11.00
Σ	1	m_{tot}	14.43	V_{a_tot}	20.00

7.2. Sample cells for testing

The tested cells were state-of-the-art MSCs with LSCF cathode material manufactured by Plansee SE®. The support material measures 50x50mm in size and the active layers including the cathode come in at 40x40mm with a total cell thickness of around 950 μ m.[82] Fig.25 shows the sample cells before testing:

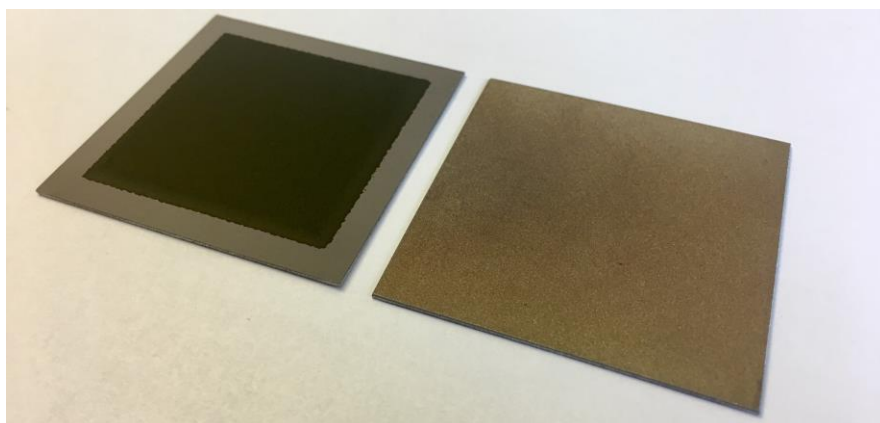


Figure 25: MSC sample cell with 40x40mm LSCF cathode (left); anode side (right)

The detailed manufacturing process for the cells can be seen in Fig.12. The screen printed cathode was fired in-situ for 10h at 850°C in reducing atmospheres. The basic buildup and specs of the samples are listed in Table 9:

Table 9: Buildup of tested MSC sample cells[82]

No.	Layer	Geometry	Material
1	Substrate	50x50mm thickness: 0.8mm	ferritic ITM-alloy (details see [83])
DBL 1	Diffusion barrier layer	40x40mm	GDC
2	Anode	40x40mm thickness: 80-100µm	Ni/8YSZ (2a,b = 60/40 2c = 80/20)
3	Electrolyte	40x40mm thickness: 4µm	8YSZ
DBL 2	Diffusion barrier layer	40x40mm	GDC
4	Cathode	40x40mm thickness: 50µm	LSCF 6428

For the experiments five samples with LSCF cathode material were available. A detailed SEM picture of the cross section of a MSC and a sketch with all functional layers mentioned in Table 9 are illustrated in Fig.26. The coarse porous substrate (1) can be seen at the bottom with the gradually finer anode layers (2a,b,c), the dense electrolyte (3) and the cathode layer (4) on top.

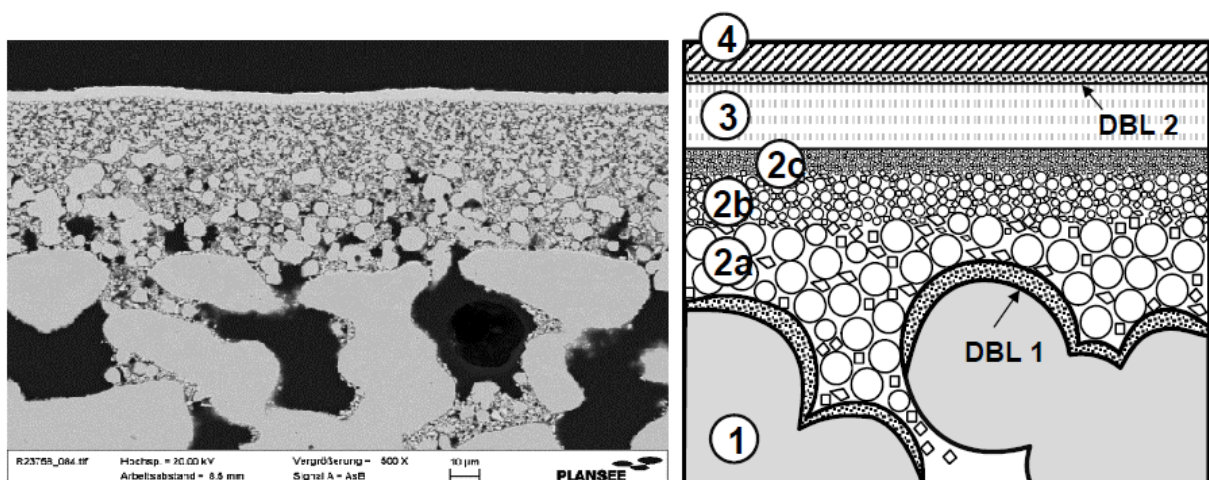


Figure 26: SEM picture of the cross section of MSC sample provided by Plansee SE (left); schematic of cross section with marking of the functional layers (right)[82]

7.3. Test bed setup

The infrastructure for the experiments was provided by the Institute of Energy and Climate Research, Department for Fundamental Electrochemistry (IEK-9) at the Forschungszentrum Jülich GmbH (FZJ). The employed test rig was a single cell SOFC – Teststand from the company EBZ Entwicklungs- und Vertriebsgesellschaft Brennstoffzelle mbH, model FCTR-C-FZJ-E-10-2-XX-L-01, year 2012.[85] Fig.27 shows a model of the test bench:

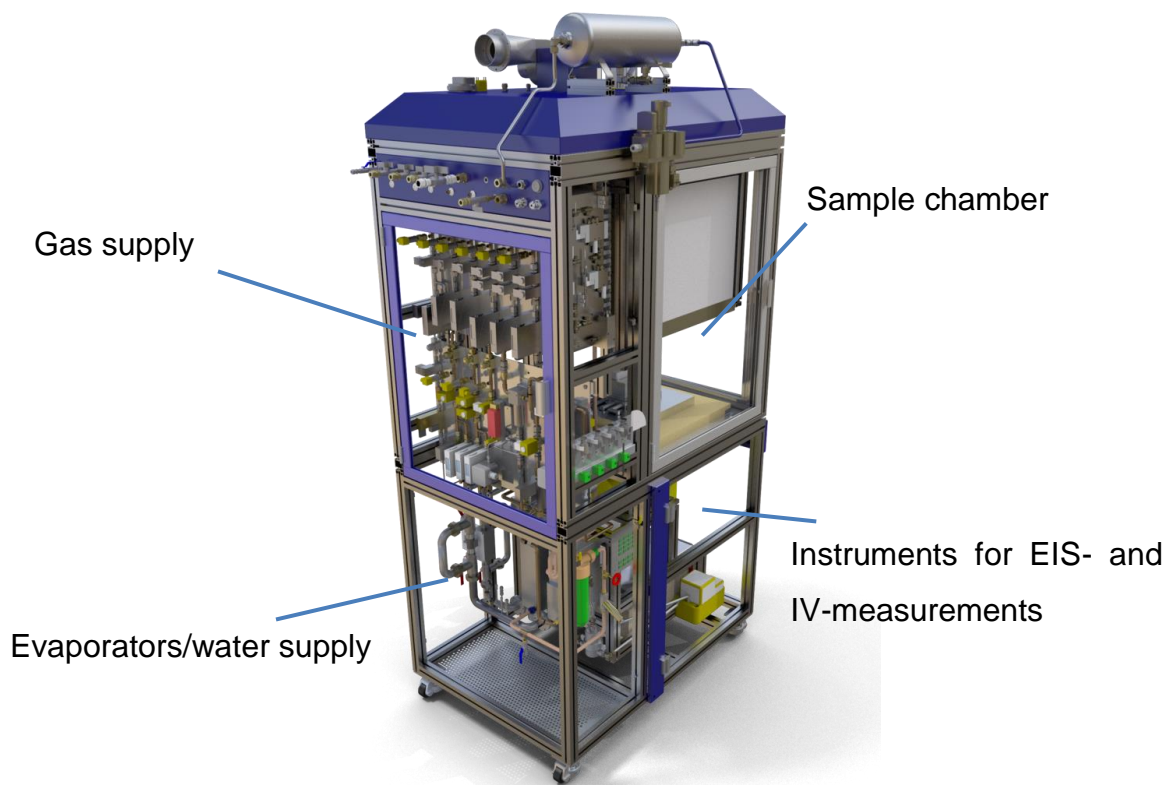


Figure 27: Model of EBZ single cell test rig used at the FZJ[86]

Further the test bench was outfitted with a CO₂-supply at the cathode line in order to meet the gas composition requirements for the exhaust gas experiments. Fig.28 shows the flow diagram implemented into the graphical user interface (GUI) of the test bed. On the left hand side the different actuators and measuring points for the media supply MFCs are implemented (top left: cathode line; bottom left: anode line). Note that in this picture the retrofitted CO₂-supply is not displayed because there was no publishable version of the updated flow diagram available at the time of testing. The implemented MFCs were ABB purgemaster, ABB 10A61/42 and Bürkert 8711 for the gas supply and Bronkhorst L13V12-AGD-33-K for the water supply.

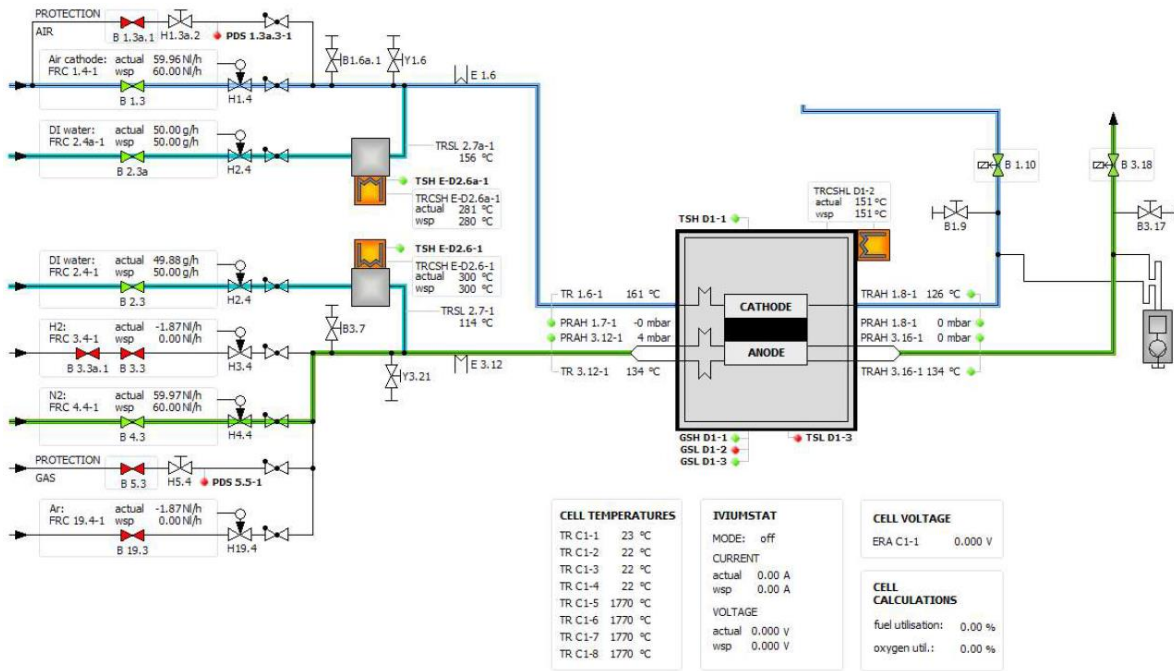


Figure 28: Flow diagram of the GUI implemented at the EBZ single cell test rigs at the FZJ[85]

In the center the heated sample chamber (grey) is visualized with a single cell test setup inside (cathode up). At the bottom all the monitored cell parameters (temperatures, cell voltage, fuel- and air utilization) and the status of the IV-measurement (Iviumstat) are shown. For temperature measurement type K thermocouples were used.

7.3.1. Cell housing and sealing

The cell housing for the single cell tests was manufactured in house at the FZJ and feature a ceramic build up with additional steel weights to achieve a proper seal between anode and cathode line. The layout of the setup can be seen in Fig.29. The ceramic parts of the housing were manufactured of aluminum oxide (Al_2O_3) to incorporate the 50x50mm single cells fitted with 40x40mm active cathode area. The weights were made of stainless steel. As shown in Fig.29 (right) the sample cell assembly is placed cathode side up on top of the base plate of the housing. The anode gas is supplied from the underside, where the cell rests on a gas distribution rack with a nickel current collector grid placed in-between them. The off-gas of the anode line is channeled away from the cell after utilization through the base plate.

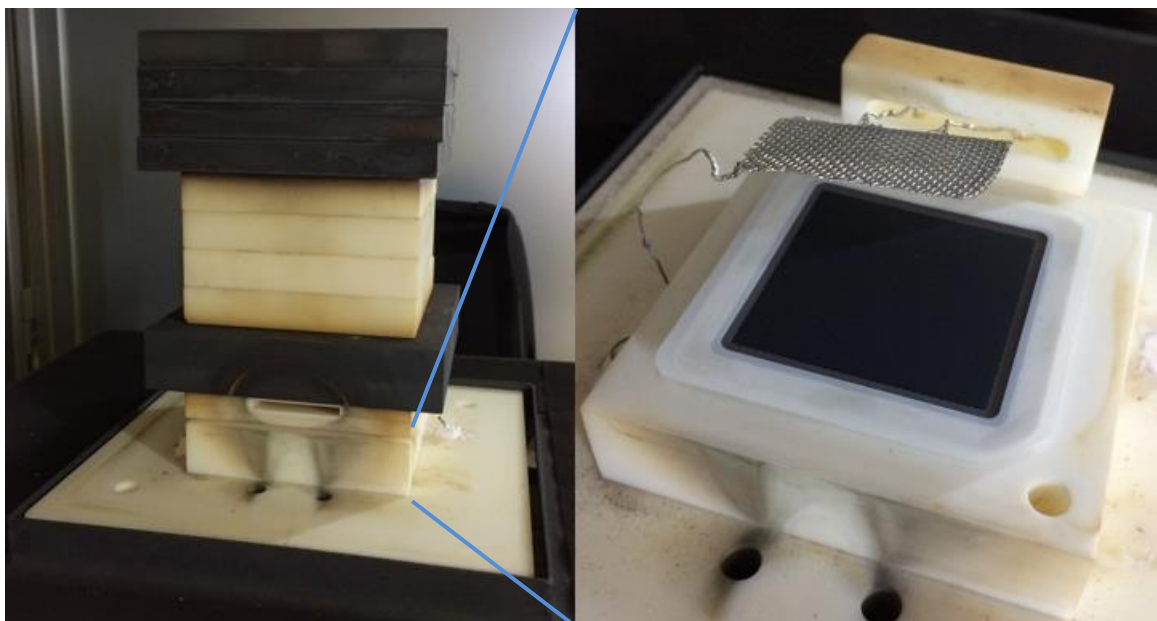


Figure 29: Test setup for single cell tests at FZJ: complete housing with steel weights (left); base plate with sample cell assembly (cathode side up) and Pt-current collector grid before final assembly (right)

The gas tightness of the test setup is provided by sandwiching the sample cell between two YSZ-frames and sealing it off with glass solder (type M242V/M243H) around the edges. Fig.30 shows a sample cell assembly with the YSZ frame and glass solder seal before testing. The YSZ-frames seal against the surface of the ceramic housing to the outside and through the glass solder against the sample cell to the inside to provide gas tightness between the cathode and anode side of the cell. On top of the sample a platinum current collector grid and another gas distribution rack for the cathode gases are stacked and weighed down by an additional steel weight.

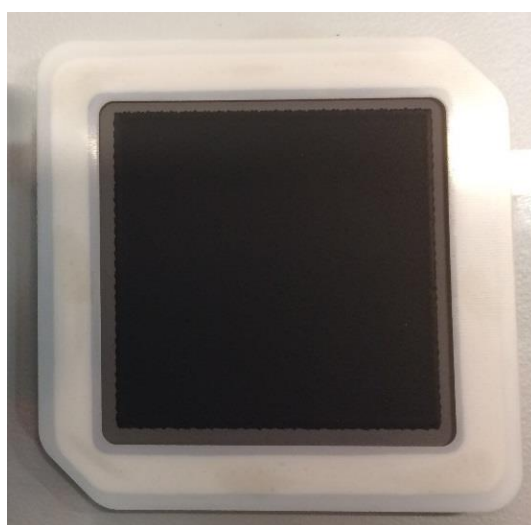


Figure 30: Sample cell assembly with YSZ-frame and glass solder sealing before testing

The cathode exhaust gases are ejected into the sealed sample chamber, where they are sucked away through the bottom of the base plate (black holes in Fig.29). To achieve gas tightness of the test setup all the components were assembled with utter care in order to avoid any sort of particle or debris contaminating the ceramic sealing surface. Due to the use of the ceramic cell housing components the maximum temperature gradient during heatup and operation was set to 1K/min.

7.3.2. Measurement equipment at test bed

During testing online monitoring of cell temperature and open circuit voltage was performed. The cells were operated without any electrical load, only for the periodic electrochemical characterization through IV-measurements electrical power was drawn from the cells. In these characterizations, electrochemical impedance spectroscopy (EIS) and current-voltage-dependency (IV-curve) measurements were carried out. These operations were controlled by an IviumStat A45206 electrochemical interface and impedance analyzer in combination with an IviumBoost IB7107 current booster supplied by Ivium Technologies B.V.

7.4. Testing schedule

For testing five identical samples as described in chapter 7.2. were available. One cell was left untouched as a backup/reference, hence four samples were tested under different conditions. As mentioned in the introduction, the goal of the experiments was to investigate the tolerance of the sample cell, in particular the cathode material for H₂O- and CO₂-containing surroundings during a simulated heatup process. Therefore a variation of the temperature between each experiment was chosen as a testing strategy. At the Forschungszentrum Jülich GmbH five consecutive weeks of experimental time were available at the test facilities. Thus the goal for setting up the detailed testing schedule was to maximize testing time within these five weeks avoiding test bed downtime as much as possible.

7.4.1. Startup procedure

At the beginning of each experiment the test assembly (sample cell and cell housing) had to be heated up according to a specific routine in order to avoid any condensation at the cell and ensure a proper seal of the sample cell assembly.

The startup procedure is further limited by the heating and cooling rates of the ceramic parts of the housing (1K/min maximum for Al₂O₃) to avoid excess thermal stress resulting in damage of ceramic parts. Additionally the test sample is initially characterized by recording IV-curves and EIS-spectra in 50°C intervals when cooling down from 850° to 650°C. The detailed startup procedure is listed in Table 10.

Table 10: Startup procedure for single cell tests at FZJ

Step	Temperature [°C]	Duration [hh:mm]	Gas species [NI/h]	Comment
Purge	20	00:30	Anode: 10 N ₂ Cathode: -	All gases off, purging of anode line
Heatup 150	20	02:10	Anode: - Cathode: -	Heatup to 150°C with 1K/min before gas application to prevent condensation
Gas application	150	00:05	Anode: 3 H ₂ /3 H ₂ O/14 N ₂ Cathode: 40 Air	Switch on gas supply (H ₂ /H ₂ O=1:1)
Heatup 350	150	03:20	Anode: 3 H ₂ /3 H ₂ O/14 N ₂ Cathode: 40 Air	Heatup to 350°C with 1K/min
Hold 350	350	01:00	Anode: 3 H ₂ /3 H ₂ O/14 N ₂ Cathode: 40 Air	Hold time for glass solder
Heatup 850	350	08:20	Anode: 3 H ₂ /3 H ₂ O/14 N ₂ Cathode: 40 Air	Heatup to 850°C with 1K/min
Hold 850	850	10:00	Anode: 3 H ₂ /3 H ₂ O/14 N ₂ Cathode: 40 Air	Hold time for glass solder and in situ cathode sintering
Gas application	850	00:05	Anode: 6 H ₂ /3 H ₂ O/11 N ₂ Cathode: 40 Air	Change anode gas composition (H ₂ /H ₂ O=2:1)

Step	Temperature [°C]	Duration [hh:mm]	Gas supply [NI/h]	Comment
1 st character- ization	850	01:00	Anode: 6 H ₂ /3 H ₂ O/11 N ₂ Cathode: 40 Air	IV-curve; EIS before and after IV
Cooldown 650 + character- ization every 50°C	850-650	10:00	Anode: 6 H ₂ /3 H ₂ O/11 N ₂ Cathode: 40 Air	Cooldown to 650°C with 1K/min

7.4.2. Test matrix

After the boundary conditions were defined a detailed schedule was developed for the five weeks of testing at the FZJ-facilities. As mentioned a total of five MSC sample cells with LSCF cathode material were available for investigations, whereas one of the samples (LSCF 0: 1309-175B) was left untouched for the later post mortem analytics. The examination of the remaining samples (LSCF 1-4) was spread out over the five weeks of testing. The complete test matrix is shown in Table 11.

As for the testing strategy a temperature variation (650/500/350°C) between each experiment was chosen as the way to go. Further the cathode gas species were altered between LSCF 1 and LSCF 2-4 from conventional air to the simulated exhaust gas (Table 7). The anode gas composition was kept unchanged for each trial as a mixture of humidified hydrogen and nitrogen (Table 8). For the duration of each test run 80h/cell of exposure time at constant temperature and gas composition were targeted. During the test run frequent characterizations were performed consisting of IV-recordings with EIS-measurements at OCV prior and after each IV-curve. These characterizations were conducted at standardized measuring conditions for each test (temperature 650°C; defined anode gas (Table 8); 40NI/h air at the cathode side). The IV-measurements were performed until either a maximum load of 40A (=2.5 A/cm²) or minimum cell voltage of 600mV with a current alteration step of 200mA per 10s. Moreover it is expected, that every individual sample cell shows a slightly different power output and resistance pattern to begin with.

Table 11: Test matrix; total anode gas flow: 20NI/h; total cathode gas flow: 40NI/h

Name / sample number	Purpose	Conditions	Gas species [NI/h] (see details in Table 7/8)			Duration	Measurements during testing	Post mortem analytics
LSCF 1 1309-005A (reference)	Reference test to get power output and behavior under standard operating conditions	Standard operating point: T=650°C	Operation	Anode 6 H ₂ 3 H ₂ O 11 N ₂	Cathode 40 Air	80h/cell	Characterization every 5h - IV-curves - EIS before and after IV	Analyzation of chemical composition - SEM/EDX - XRD
			Characterization	6 H ₂ 3 H ₂ O 11 N ₂	40 Air			
LSCF 2 1309-005B LSCF 3 1309-019B LSCF 4 1309-019A	Tests with exhaust gas at cathode side	Exposure to exhaust gas on cathode side; Temperature variation between each test sample: T=650/350/500 °C	Operation	6 H ₂ 3 H ₂ O 11 N ₂	1.65 CO ₂ 5.75 H ₂ O 32.6 Air	80h/cell	Characterization every 3h/40h - IV-curves - EIS before and after IV	Analyzation of chemical composition - SEM/EDX - XRD
			Characterization	6 H ₂ 3 H ₂ O 11 N ₂	40 Air			

At first a reference trial (LSCF 1/1309-005A) was conducted in order to investigate the degradation a cell experiences under normal operating conditions (defined anode gas (Table 8); air with no H₂O or CO₂ applied to cathode side) and to generate a foundation for comparing the following experiments to. The test was performed at a temperature of 650°C for the whole exposure time of 80h. During the test characterizations were executed frequently every 5h. After the exposure time the whole test bed was cooled down back to room temperature at 1K/min. The cooldown took approximately 10h until the test assembly could be disassembled and samples could be changed.

The second trial (LSCF 2/1309-005B) was executed at a temperature of 650°C as well, but with the simulated exhaust gas (Table 7) supplied to the cathode side of the sample. Further characterizations were done every 3h to get a more detailed monitoring of the cell behavior under exhaust gas application, since there was no knowledge about how fast the H₂O and CO₂ induced deterioration was going to occur.

The last two experiments were performed at temperatures of 350°C (LSCF 4/1309-019A) and 500°C (LSCF 3/1309-019B) respectively. As characterizations had to be carried out at a defined temperature of 650°C to generate comparable results, these two trials were split into two 40h segments of exhaust gas exposure each. Characterizations were scheduled at the beginning, at the halfway mark after 40h and at the end of the exposure time to reduce total heatup and cooldown time. Additionally it was decided to execute the trial LSCF 4 at 350°C at first because it was expected to show the most significant degradation at these lower temperatures (see chapter 6.2.-temperature dependence of LSCF degradation under the presence of H₂O and CO₂).

Before each experiment the testing assembly was cleaned and inspected thoroughly for any abnormalities in order to keep the test surroundings as steady as possible to deliver comparable and reproducible results. The test programs were implemented into the test bed's software to run the desired sequences automatically 24/7. Anyhow frequent control through the operator was executed.

8. Results of cell tests

To provide clear and comparable results the displayed data is reduced to the most significant points at the start (0h), at half time (40h) and at the end (80h) of each test run. The evaluation of each experiment therefore consists of IV-curves comprising characterizations at 850°C, 700°C and 650°C 0h/40h/80h and the corresponding Nyquist plots generated from the EIS-measurements. It is pointed out, that each sample cell shows a different power output and frequency response to start with.

8.1. LSCF 1: Reference trial at 650°C (1309-005A)

The reference trial at 650°C (LSCF 1/1309-005A) was executed first in order to gather basic knowledge about the behavior and the handling of the test setup under normal operating conditions (pure air at cathode; fuel mix from Table 8 at anode). The temperature profile and the evolution of the cell voltage over time are shown in Fig.31. The total duration of the LSCF 1 experiment was around 140h (approximately 6 days).

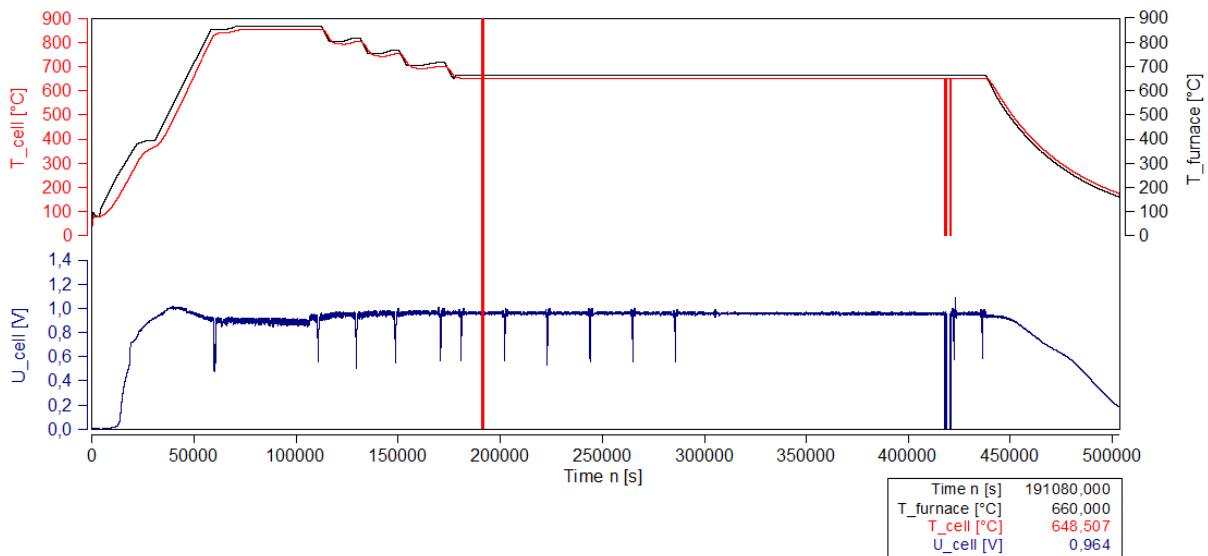


Figure 31: Timeplots of cell (T_{cell}) and furnace temperature ($T_{furnace}$) and cell voltage (U_{cell}) of the LSCF 1 trial

The temperature profile in Fig.31 shows the heatup and sealing procedure including the consequent stepwise cooldown to 650°C at the beginning of the test run as described in Table 10. Afterwards the exposure period with periodic characterizations every 5h at a constant temperature of 650°C and an anode and cathode gas composition listed in Table 11 takes place. The cooldown slope after the last characterization can be seen at the right hand side of the plot. The evolution of the

cell voltage (U_{cell}) is shown in the lower part of Fig.31. The downward-facing spikes represent the periodic IV-measurements. The otherwise rather constant OCV of around 960mV indicates a proper seal of the cell and therefore no gas leakages between anode and cathode. Halfway through the exposure period the connection to the IviumStat was lost and had to be reestablished. Nevertheless the significant measurements at the beginning, halfway and at the end of the exposure period were available. Fig.32 shows an overview of the recorded IV-curves during the cooldown at 850°C and 700°C and the ones at the beginning (0h) at the halfway point (40h) and at the end (80h) of the exposure period at 650°C. The curves express the behavior of the cell voltage U under load depending on the current density i considering an active cell area of 16cm².

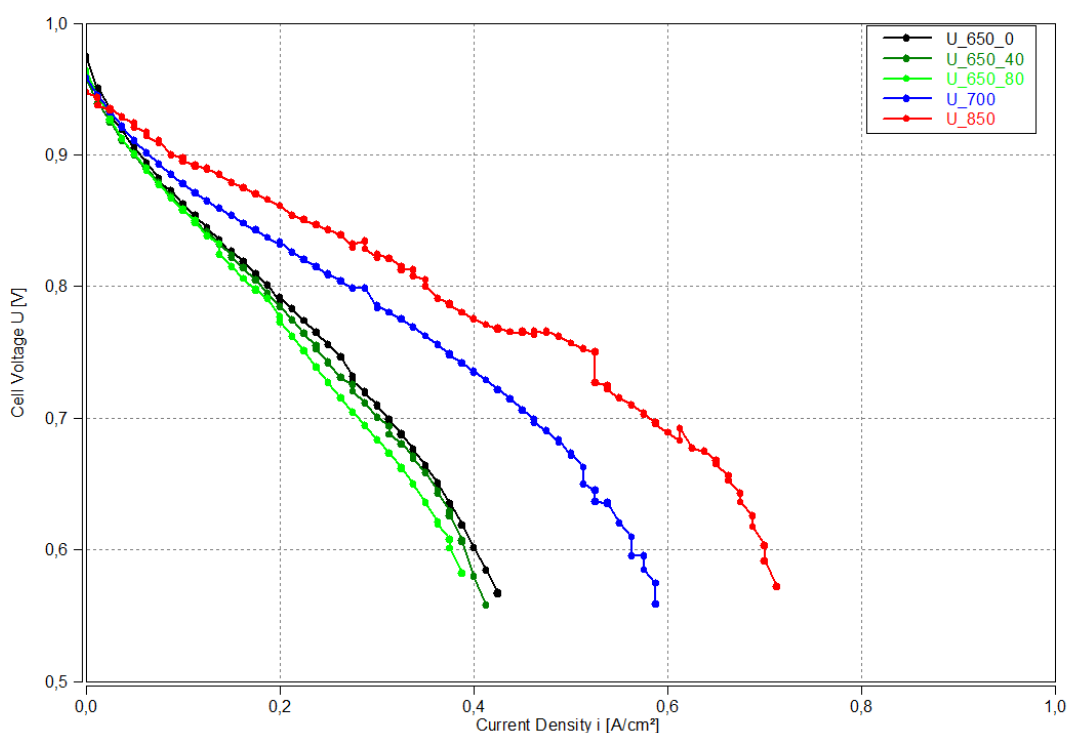


Figure 32: Overview of IV-measurements recorded at 850°C, 700°C and 650°C after 0/40/80h of exposure (LSCF 1)

Fig.33 further shows a detailed display of the IV-curves during the exposure period at 650°C. The three characteristic regions (activation-, ohmic- and concentration polarization) according to Fig.8 are distinguishable in the shape of the trends. The recorded curves show a slight drop in current density and therefore power output of the cell over the duration of the experiment. To quantify the degradation the percentage of power loss during 80h was calculated at a cell voltage of 0.7V (pink cursor) at 9.65% relative to the current density at 0h of exposure at 650°C.

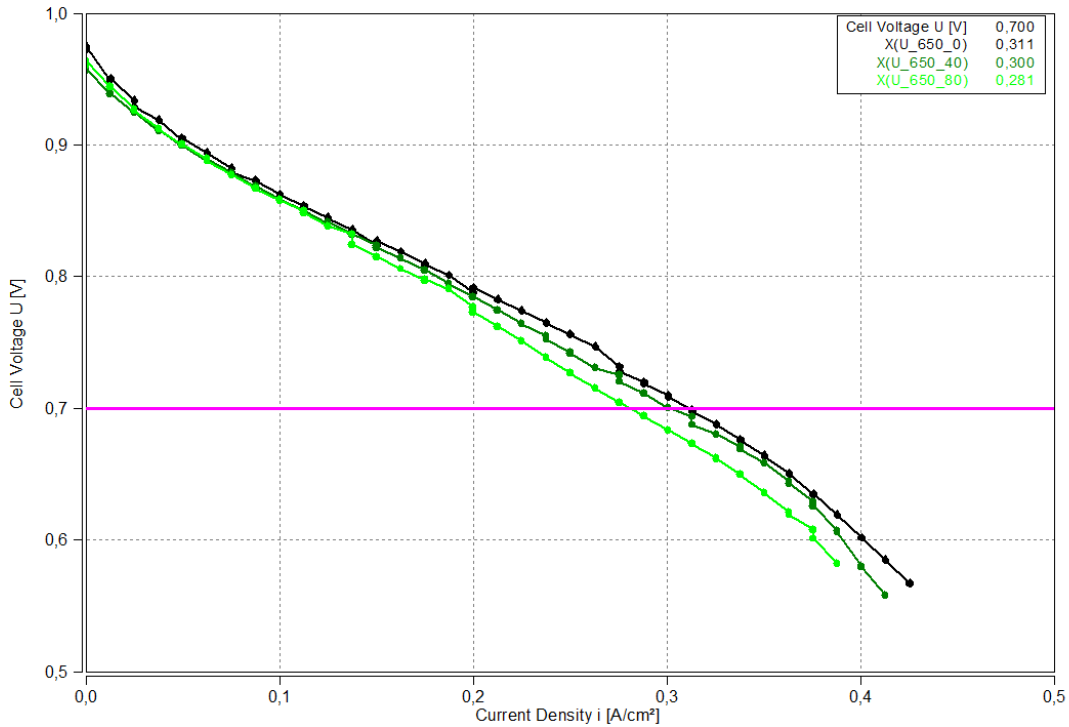


Figure 33: Detail of IV-curves recorded at 650°C after 0/40/80h of exposure; comparison of current density at 700mV (pink cursor, LSCF 1); 9.65% decrease in current density i

In Fig.34 the Nyquist plots of the frequency responses corresponding to the IV-curves shown in Fig.33 are plotted. The EIS-data were recorded straight before each IV-measurement at OCV.

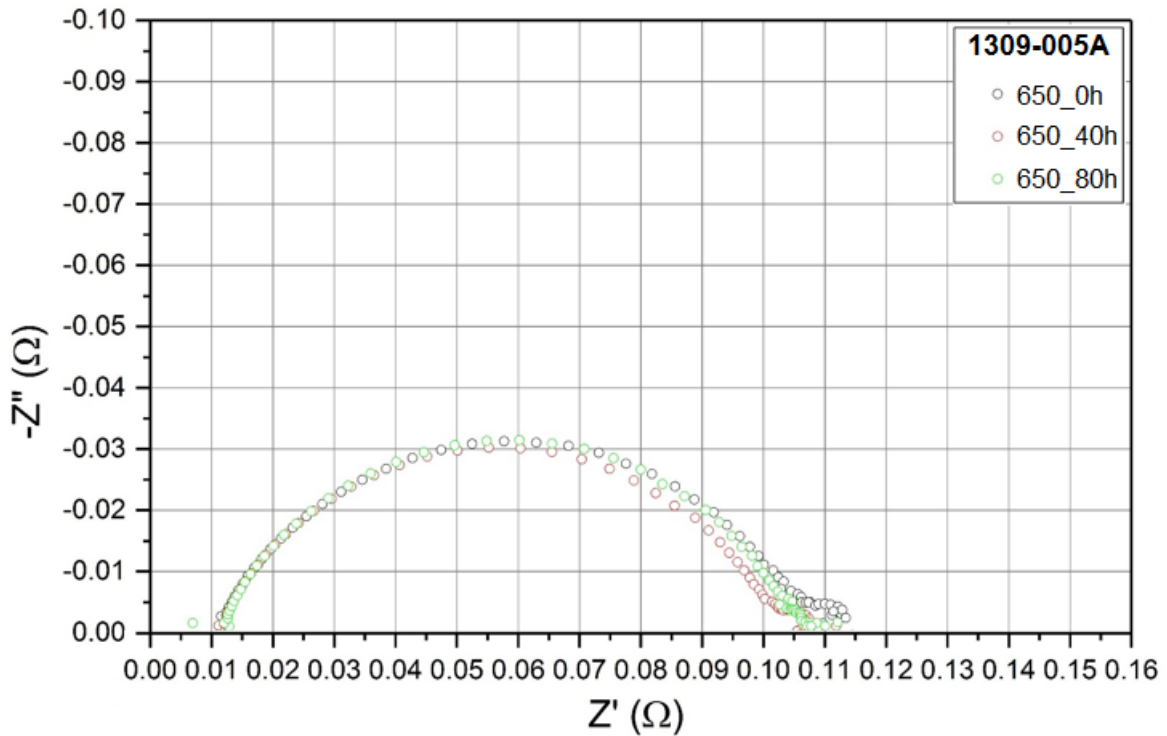


Figure 34: Nyquist plots of frequency responses recorded at 650°C after 0/40/80h of exposure (LSCF 1); 6.14% decrease in low frequency resistance

The plots in Fig.34 show a minor shift in the low to mid frequency range on the right hand side of the trend. Overall the resistance stays fairly constant over the duration of the experiment with a slight overall decrease of 6.14% at low frequencies.

8.2. LSCF 2: Exhaust gas trial at 650°C (1309-005B)

After the reference trial the next experiment was conducted at the same 650°C, 80h of exposure time and anode gas composition (Table 8), but with simulated exhaust gas (Table 7) applied to the cathode (LSCF 2/1309-005B). Fig.35 shows the profile of cell and furnace temperature as well as cell voltage over time. The duration of this experiment was around 164h (7 days).

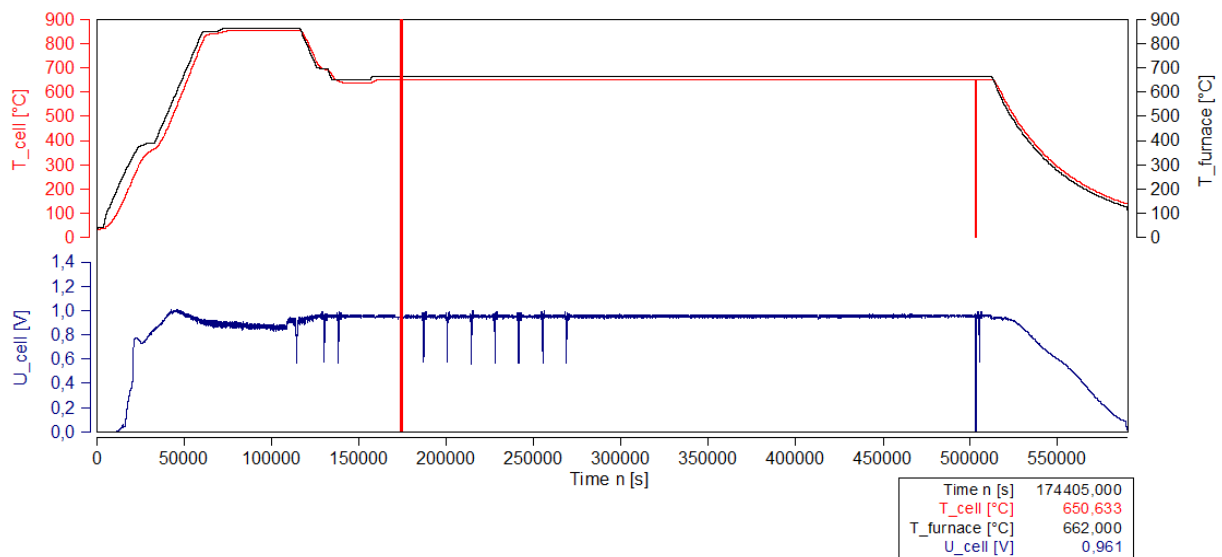


Figure 35: Timeplots of cell (T_{cell}) and furnace temperature ($T_{furnace}$) and cell voltage (U_{cell}) of the LSCF 2 trial

For this and the ongoing experiments the characterizations during the cooldown from 850°C to 650°C were reduced to three measuring points at 850/700/650°C in order to shorten the cooldown process. The constant OCV of around 960mV again indicates a proper seal of the test assembly. During exhaust gas exposure characterizations were made every 3h to obtain a finer resolution of the degradation behavior. After the 8th measurement the connection to the measuring equipment was lost again, but sufficient data were recorded to make a statement about the cell condition at the beginning, the middle and the end of the exposure period. In Fig.36 an overview of the recorded IV-data at 850°C, 700°C and during the exposure period at 650°C after 0/40/80h of exhaust gas application at the cathode is displayed.

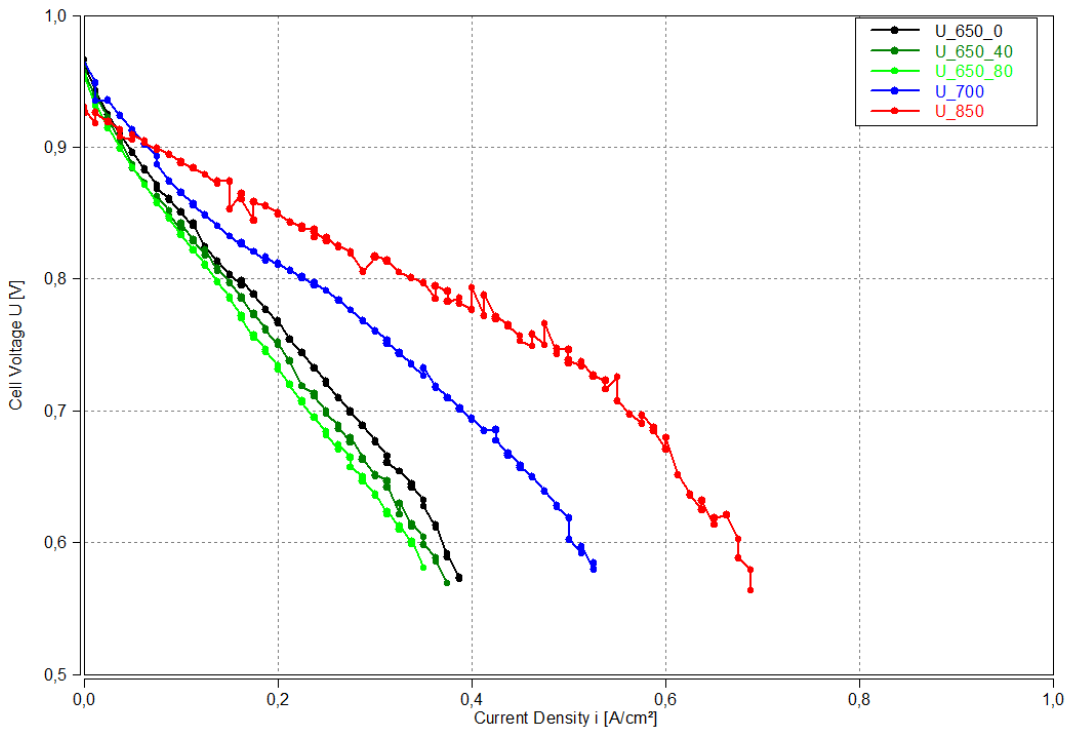


Figure 36: Overview of IV-measurements recorded at 850°C, 700°C and 650°C after 0/40/80h of exhaust gas exposure (LSCF 2)

Fig.37 further displays a detail of the three IV-curves at 650°C during the exposure period. They show the established shape with the three characteristic polarization regions and at 700mV cell voltage showcase a decline of 15.33% in current density based on value at 650°C/0h over the 80h of exhaust gas application.

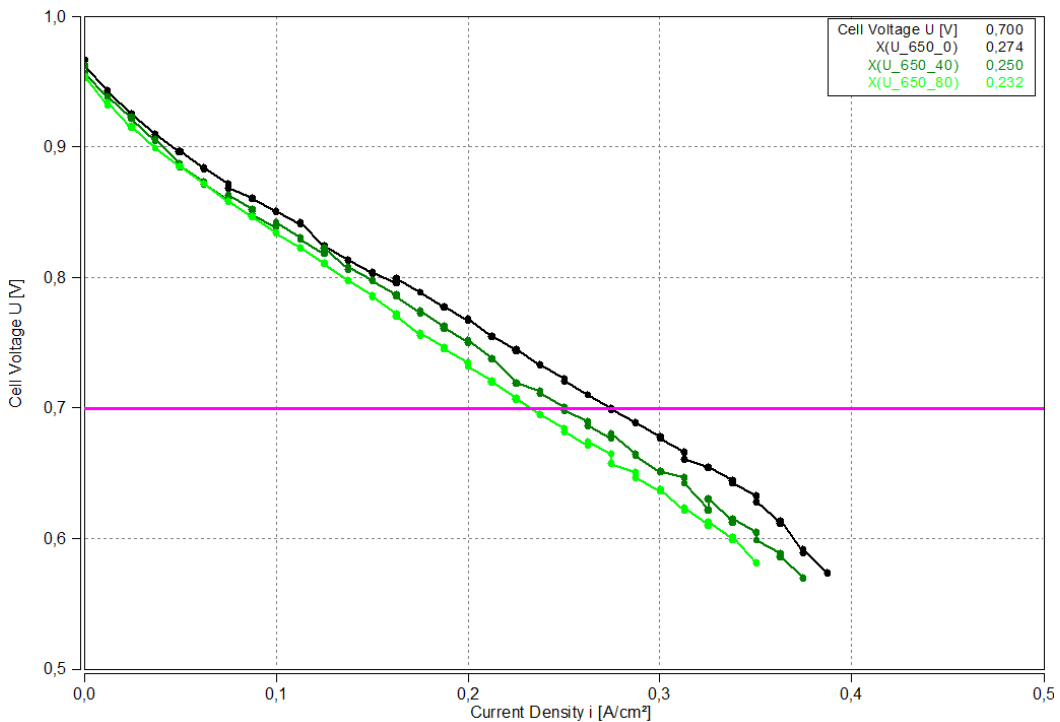


Figure 37: Detail of IV-curves recorded at 650°C after 0/40/80h of exhaust gas exposure; comparison of current density at 700mV (pink cursor, LSCF 2); 15.33% decrease in current density i

In Fig.38 the Nyquist plots of the frequency responses corresponding to the IV-curves in Fig.37 are plotted. The spectra were recorded at OCV/650°C right before each IV-measurement respectively. The graphs show a continuous increase in the low to mid frequency range over the duration of the experiment. The maximum shift of the resistance at low frequencies was calculated at 20.75% based on the value at 0h. The evolution of the shape of the curves indicates a change in both real and imaginary part, respectively amplitude and phase of the frequency responses over the exhaust gas exposure period.

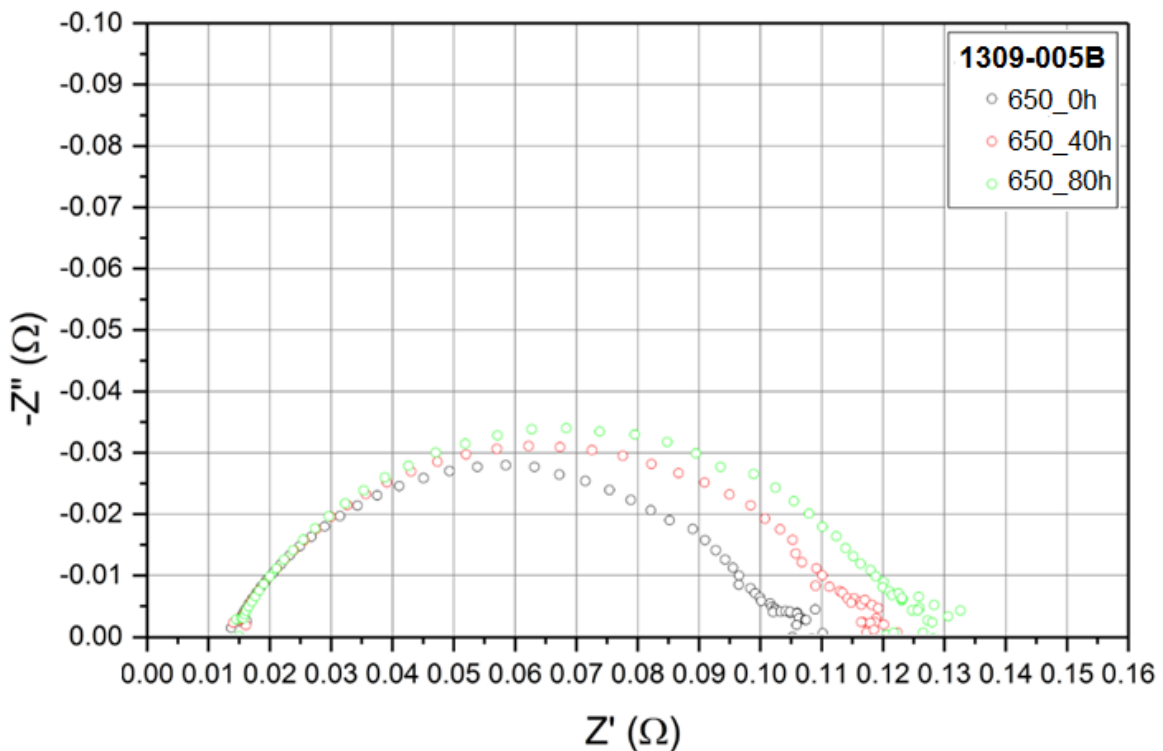


Figure 38: Nyquist plots of frequency responses recorded at 650°C after 0/40/80h of exhaust gas exposure (LSCF 2); 20.75% increase in low frequency resistance

8.3. LSCF 3: Exhaust gas trial at 500°C (1309-019B)

Next the LSCF 4 trial (sample number 1309-019B) was executed. Fig.39 shows the temperature profile and the history of the cell voltage. After the heatup and sealing procedure and the initial characterizations the cell was cooled down to 500°C and exposed to the simulated exhaust gas (Table 7) for 40h. Subsequently the cell was heated up again to 650°C and characterized according to Table 11, with another cooldown and 40h of exhaust gas application at 500°C. Finally the cell was characterized a final time at 650°C and standard operating conditions before cooldown to room temperature.

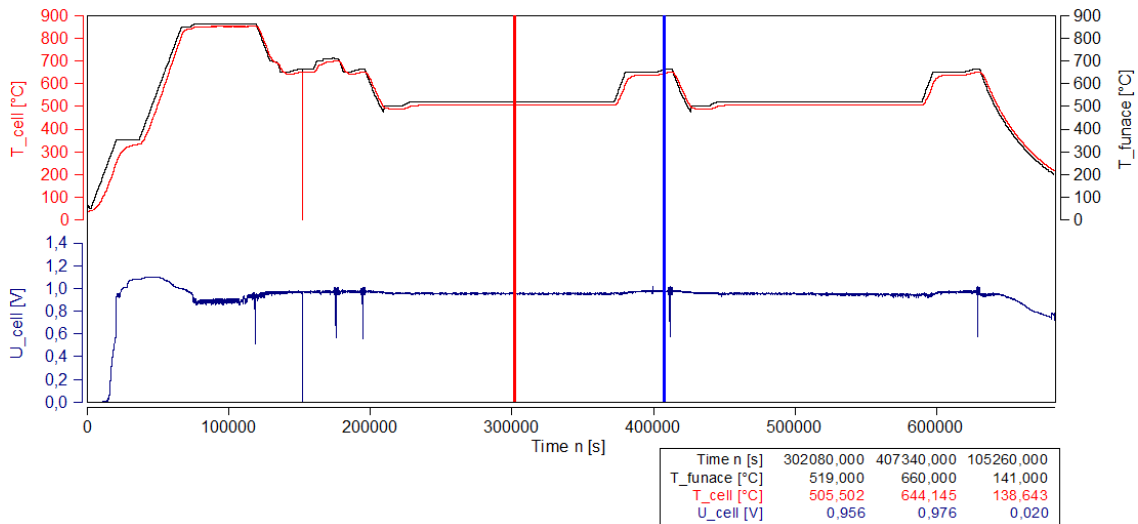


Figure 39: Timeplots of cell (T_{cell}) and furnace temperature ($T_{furnace}$) and cell voltage (U_{cell}) of the LSCF 3 trial

Fig.39 shows the startup and exposure periods with the 2x40h of exhaust gas application at 500°C and characterizations at the beginning, the halfway point and at the end of the experiment at 650°C. OCV was constant again over the exposure period at 950mV at 500°C, with a minor increase to 975mV at 650°C. The total duration of the experiment was 190h (8 days). In Fig.40 the overview of the recorded IV-measurements is shown, comprising IV-curves at 850°C and 700°C during the initial cooldown and after 0/40/80h of exhaust gas application at 500°C (data recorded at 650°C).

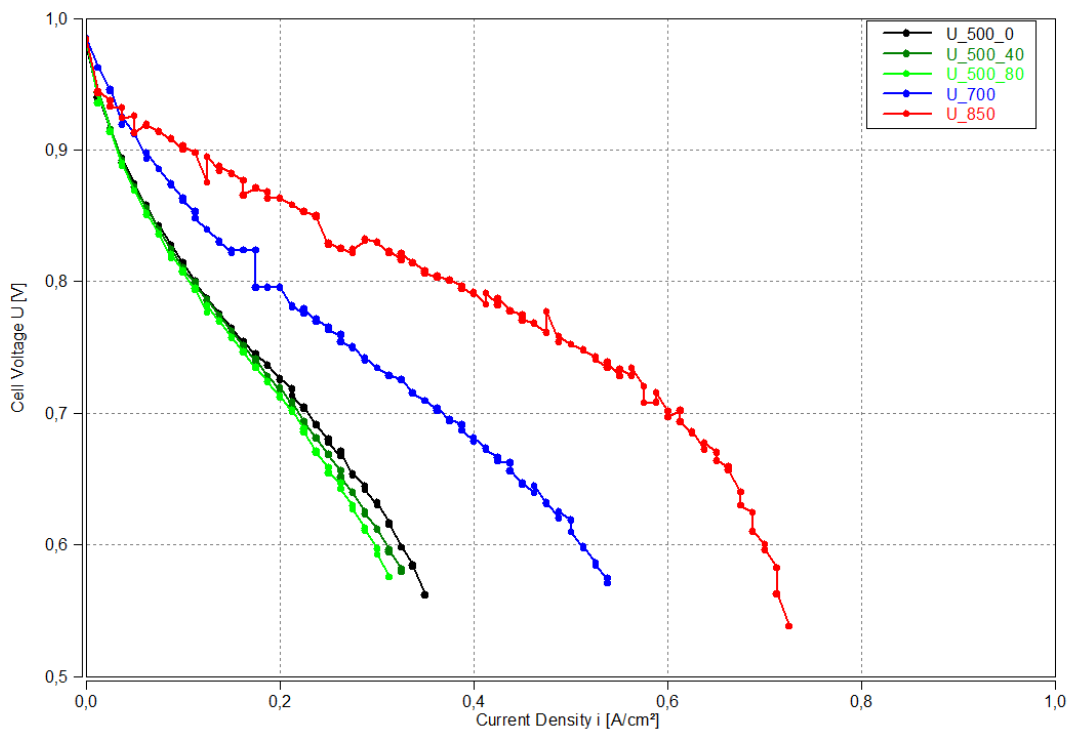


Figure 40: Overview of IV-measurements recorded at 850°C, 700°C and 650°C after 0/40/80h of exhaust gas exposure at 500°C (LSCF 3)

Fig.41 shows a detailed display of the three IV-curves right before (0h), at the halfway point (40h) and at the end (80h) of the exhaust gas exposure. They again show a fairly linear behavior in the middle of the range (ohmic polarization, see Fig.8) with a parabolic shape at the beginning at small loads (activation polarization) and at the end at loads greater $0.3\text{A}/\text{cm}^2$ (concentration polarization). The drop in current density at 700mV was calculated at 6.55% based on the current density at 0h of exhaust gas exposure.

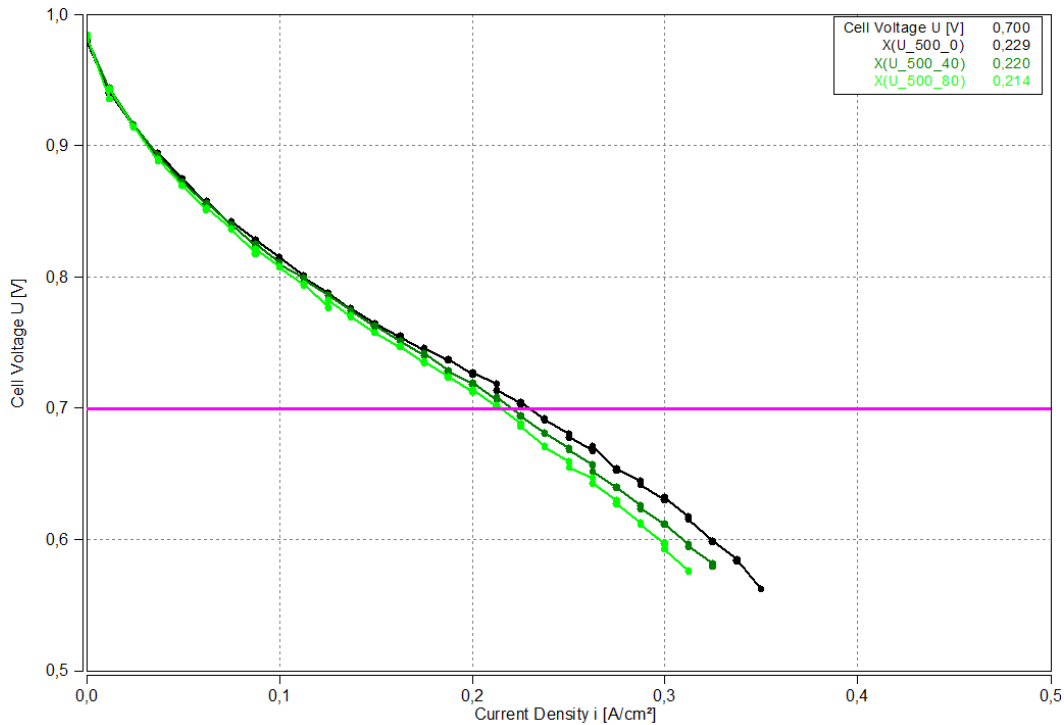


Figure 41: Detail of IV-curves recorded at 650°C after 0/40/80h of exhaust gas exposure at 500°C ; comparison of current density at 700mV (pink cursor, LSCF 3); 6.55% decrease in current density i

The Nyquist plots of the frequency responses of the characterizations according to Fig.41 are plotted in Fig.42. The spectra were recorded at OCV/ 650°C after 0/40/80h of exhaust gas application at 500°C , right before the corresponding IV-measurement. The plots again show a pronounced shift in the low to mid frequency range on the right half of the diagram paired with a minor shift in the high frequency regime at the far left. Most of the change in the frequency responses occurs during the first exposure period between 0h (black circles) and 40h (red circles) of exhaust gas application. The increase in resistance at low frequencies over the duration of the experiment was calculated at 10.99% relative to the value at the start of the measurements (0h).

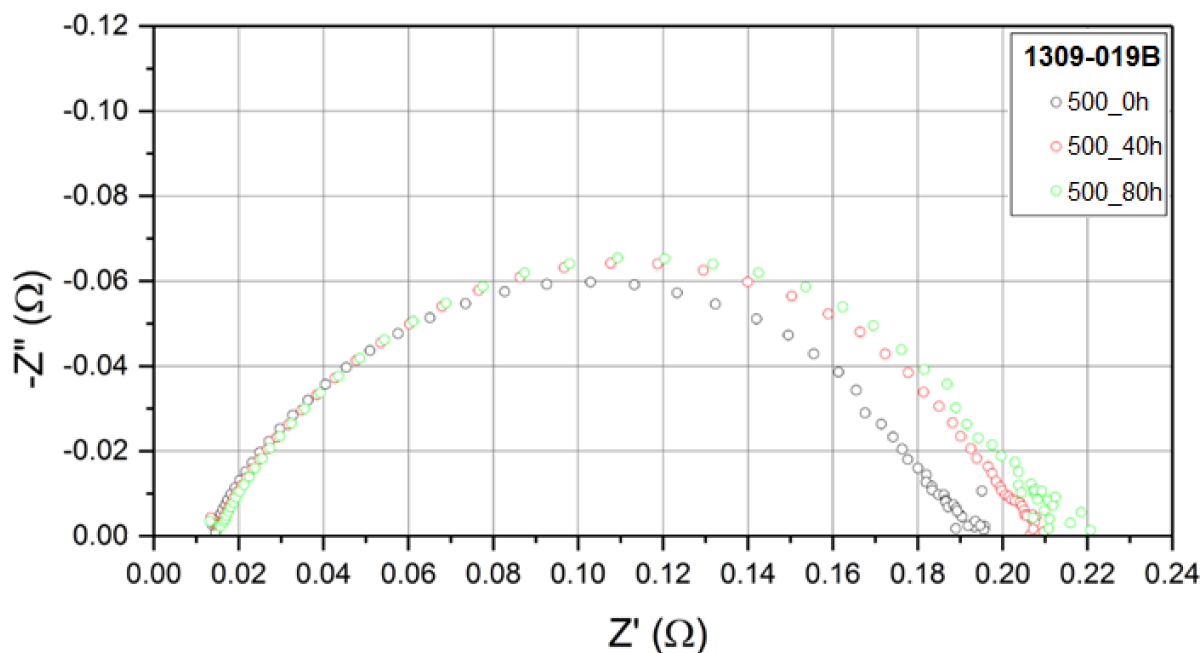


Figure 42: Nyquist plots of frequency responses at 650°C after 0/40/80h of exhaust gas exposure at 500°C (LSCF 3); 10.99% increase in low frequency resistance

8.4. LSCF 4: Exhaust gas trial at 350°C (1309-019A)

Fig.43 shows the timeplots of the LSCF 4 trial (sample number 1309-019A). The experiment featured two 40h periods of exhaust gas application to the cathode at 350°C and characterizations at 650°C after 0/40/80h of exposure time similar to the previous LSCF 3 trial. The cell voltage being dependent on temperature (see equation 14) dropped to 750mV at 350°C, but showed familiar values of 970mV at 650°C. Total duration of the experiment was clocked at 192h (8 days).

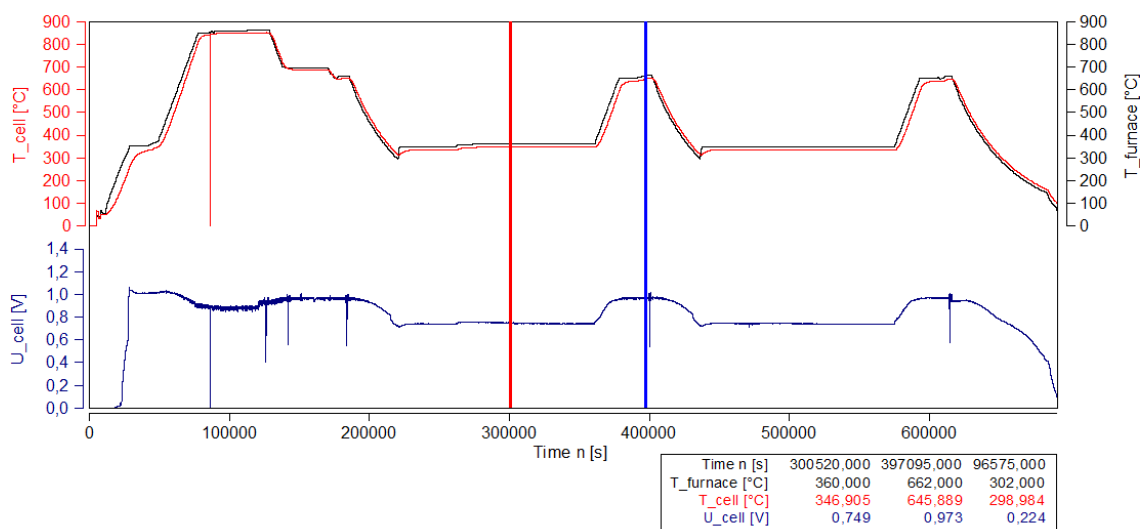


Figure 43: Timeplots of cell (T_{cell}) and furnace temperature (T_{furnace}) and cell voltage (U_{cell}) of the LSCF 4 trial

Fig.44 shows an overview of all the conducted IV-measurements during the test. IV-curves were recorded at 850/700°C and at 650°C after 0/40/80h of exhaust gas exposure at 350°C.

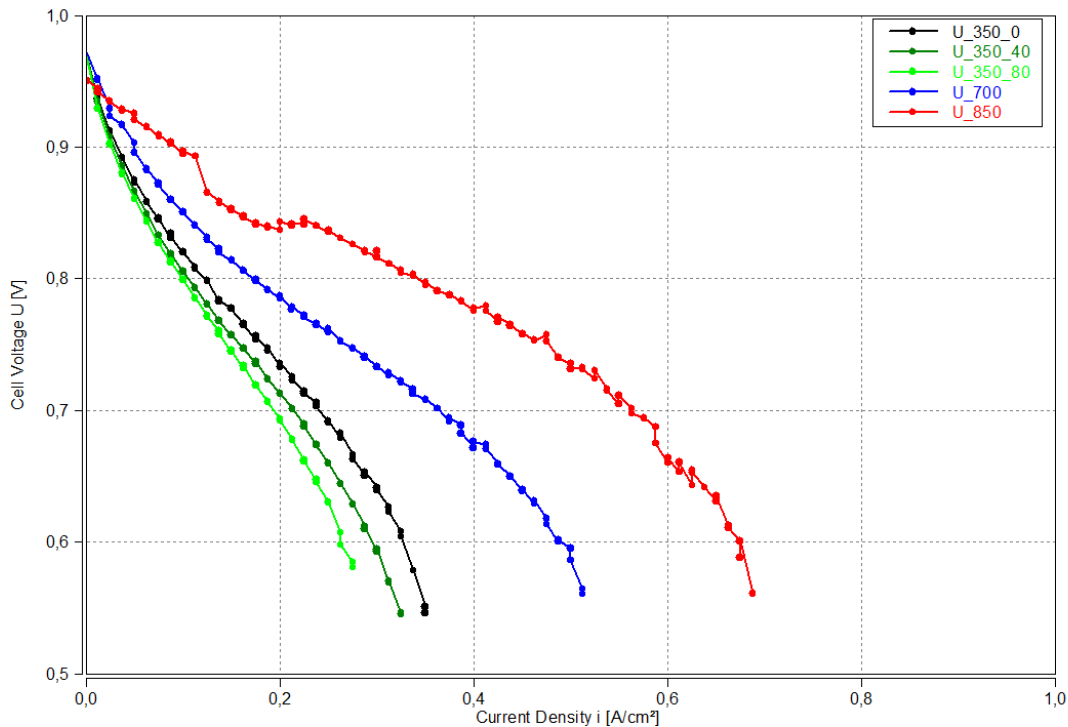


Figure 44: Overview of IV-measurements recorded at 850°C, 700°C and 650°C after 0/40/80h of exhaust gas exposure at 350°C (LSCF 4)

A detailed display of the IV-during the exhaust gas exposure at 350°C is shown in Fig.45. The plots show a similar shape to those described in the previous section (see Fig.41). The decrease in current density measured at a cell voltage of 700mV over the duration of the exhaust gas application was calculated at 19.92% based on the value at the start of the exposure (0h).

Fig.46 further displays the Nyquist plots of the frequency responses corresponding to the IV-curves in Fig.45. The spectra again were recorded right before each IV-measurement at OCV/650°C after 0/40/80h of exhaust gas application to the cathode at 350°C. The plots show a major shift in the low to mid frequency range as well as a noticeable variation at higher frequencies at the far left side of the spectra. The total increase of resistance at low frequency over the duration of the experiment was calculated at 22.87% based on the value of the first spectrum at 0h.

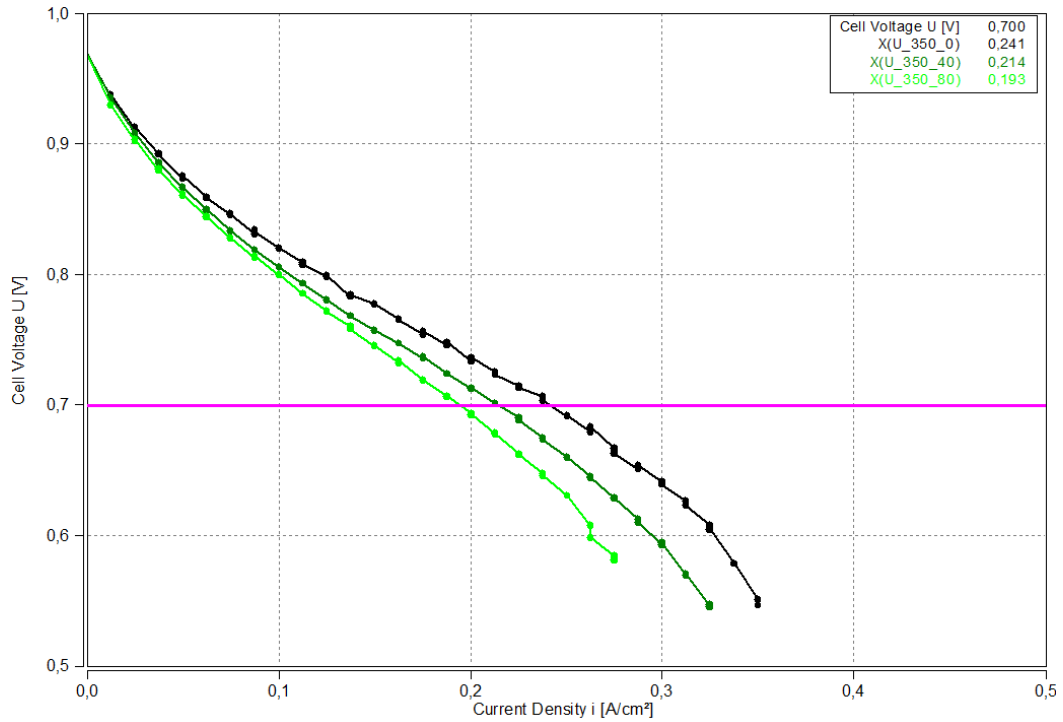


Figure 45: Detail of IV-curves recorded at 650°C after 0/40/80h of exhaust gas exposure at 350°C; comparison of current density at 700mV (pink cursor, LSCF 4); 19.92% decrease in current density i

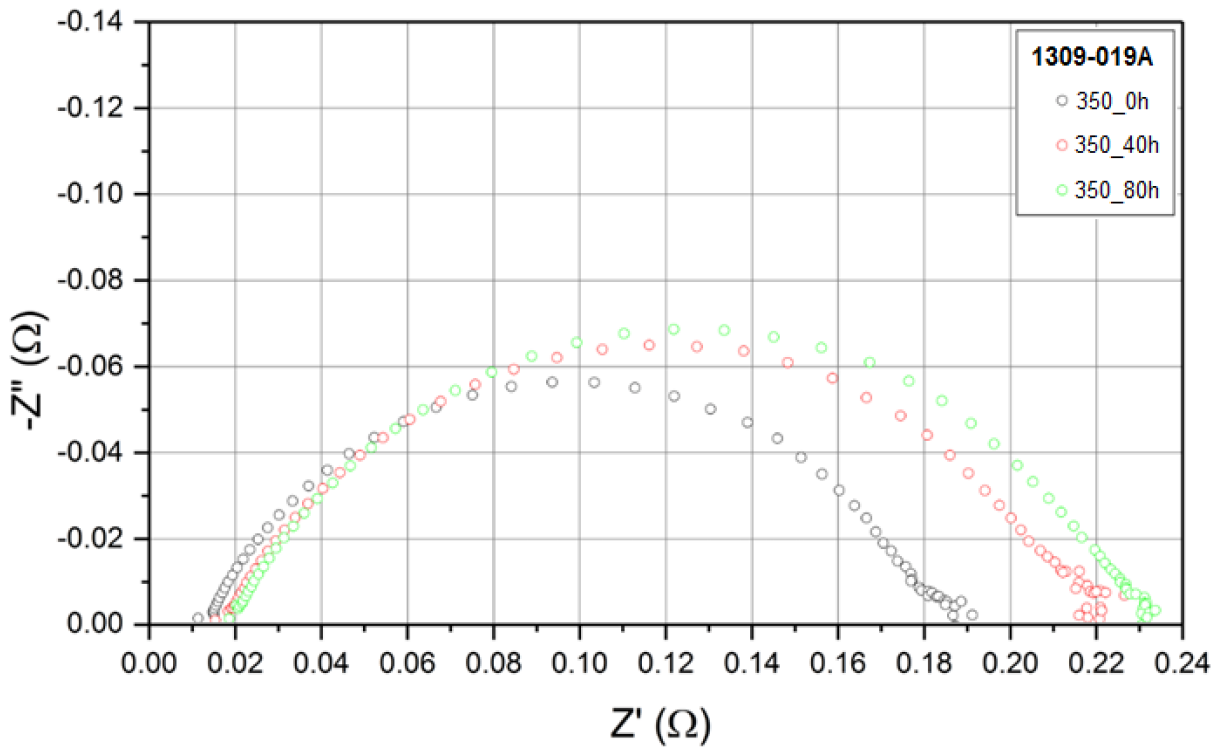


Figure 46: Nyquist plots of frequency responses recorded at 650°C after 0/40/80h of exhaust gas exposure at 350°C (LSCF 4); 22.87% increase in low frequency resistance

8.5. Summary of cell tests

Overall the intended testing schedule (Table 11) was successfully executed. The collected data are summarized in Table 12. Comparing individual data the OCV-values show some minor variation of around 10-15mV between trials indicating a proper seal and stable operation of the cell assembly. Looking at IV-data the cells show some variation of initial power output. Further all samples show a decline in current density over the duration of the experiment. The losses reach a maximum of 19.92% after 80h of exhaust gas exposure at 350°C (LSCF 4).

Regarding EIS-data the shape of the frequency response plots remains similar over the 4 experiments, although there is a shift from a minor drop in resistance at the reference experiment (LSCF 1) to a steady increase in resistance all across the frequency range over the experiments where exhaust gas was applied (LSCF 2-4). The increase in resistance was most severe at the LSCF 4 test run at an exposure temperature of 350°C. Therefore with the exception of the LSCF 3 trial the change in resistance is inversely proportional to the exposure temperature. It is noted again, that each sample had different initial resistance values to begin with.

Table 12: Summary of collected data from cell tests

Trial	Sample Number	Operating conditions (Anode / Cathode)	Duration (total / exposure)	Average OCV [mV]	Power loss* [%]	Resistance increase** [%]
LSCF 1	1309-005A	Fuel / Air T=650°C	140h / 80h	960	9.65	-6.14
LSCF 2	1309-005B	Fuel / Exhaust gas T=650°C	140h / 80h	960	15.33	20.75
LSCF 3	1309-019B	Fuel / Exhaust gas T=500°C	190h / 2x40h	975	6.55	10.99
LSCF 4	1309-019A	Fuel / Exhaust gas T=350°C	192h / 2x40h	970	19.92	22.87

* relative to current density at 0h of EG exposure

** relative to total resistance at low frequencies at 0h of EG exposure

9. Post mortem analytics

Visual inspection of the sample cells showed significant cathode delamination (Fig.47) after disassembling of the test setup. This was at first glance associated to adhesion of the cathode layer to the Pt-current collector grid during in-situ sintering of the cathode.

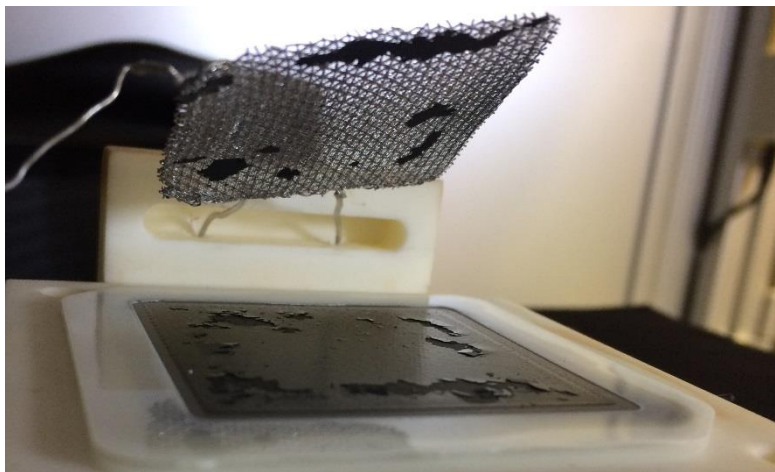


Figure 47: Cell disassembly after completed test cycle; partial delamination and adhesion of cathode layer to Pt-current collector grid

The sample cells were further examined focusing on microstructure and chemical composition of the functional components, especially the cathode layer. Therefore the samples were analysed at the Department of Physical Chemistry at the Montanuniversität Leoben (MUL) using scanning electron microscope (SEM) with corresponding energy dispersive X-ray (EDX) and X-ray diffraction (XRD) analysis technology.

9.1. Analytics strategy

The approach for the post mortem analytics was to do an investigation of both the cell cross section and the cathode surface of each sample. Hence the tested cells were cut into smaller pieces approximately 10x10mm in order to meet the requirements for the subsequent sample preparation depending on each type of analytics method. The specimens for surface examination were left untreated, whereas the pieces used for cross section analysis were further conditioned. In this case sample preparation included embedding of the sample pieces using a two-part epoxy resin cold mount (Araldit DBF CH resin + Aradur HY 951 hardener). The embedding process was done with the cells as a whole before cutting in order to

prevent further delamination of the specimens due to the cutting process. After curing the samples were then wet-ground and polished to provide a clear microsection of the cell profile. The grinding process included three steps (3µm Diamond Suspension Mono; 1µm Diamond Suspension Mono; 50nm Silica Suspension Final) to successively refine the surface. After sample preparation the specimens were handed over to the analytics department at the MUL in order to perform XRD- and SEM-analysis. X-ray diffraction investigations of the cathode layer were conducted at the untreated samples, whereas SEM images were recorded of both the microsection and the untreated surface of the cathode with additional EDX spectroscopy conducted at the cathode surface.

9.2. Suspected failure modes

Prior to the analytics possible failure patterns of the tested cells and especially the cathode layer were discussed with focus on the behavior of the samples under the somewhat uncommon application of exhaust gas to the cathode of the cell. Table 13 shows an overview of the of the suspected failure modes presumably occurring under the presence of exhaust gas resulting from aquanol combustion.

Table 13: Possible failure modes of samples cells exposed to exhaust gas containing H₂O and CO₂[87]

Failure mode	Characteristics	Display
Poisoning	Formation of secondary phases (e.g. carbonates, hydrates, hydroxides) in the presence of H ₂ O and CO ₂ ; electrically insulating and electrochemically inactive	Increase of cathode and total cell ASR leading to decrease in power output (visible in IV-curve and EIS frequency response); material contrast in SEM picture (BSD signal); XRD pattern
Segregation	Interdiffusion of active elements within the cathode (La, Sr) leading to local enrichment of certain components; prestage of poisoning: La- and Sr-rich surface more prone to carbonate and hydroxide formation	Increase of ASR and drop in power output; SEM/EDX mapping of cathode surface; XRD profile
Delamination/ Cracking	Expansion of cathode material due to thermal and chemical cycling relative to substrate leading to detachment of cathode layer	Increase of ASR and drop in power output; visible detachment in SEM picture of cell cross section
Decomposition	Decay of LSCF in highly reducing atmospheres ($p_{O_2} < 10^{-3}$ bar) at high temperatures ($T > 600^\circ\text{C}$) due to the simulated combustion exhaust gas	Increase of ASR and drop in power output; comparison of XRD profile to reference LSCF

9.3. Results from SEM-analytics

In the following section the SEM recordings of each sample cell are shown. The specimens were examined with the possible failure modes described in Table 13 in mind. The untouched sample (1309-175B) is further named LSCF 0 and works as a reference in order to characterize possible changes between the used and the green cells.

9.3.1. LSCF 0: Green sample (1309-175B)

Fig.48 shows the cross section of the unused sample cell as produced by Plansee. Analog to Fig.26 the functional layers are visible with the coarsely porous substrate at the bottom and the finely porous functional layers according to Table 9 on top of each other.

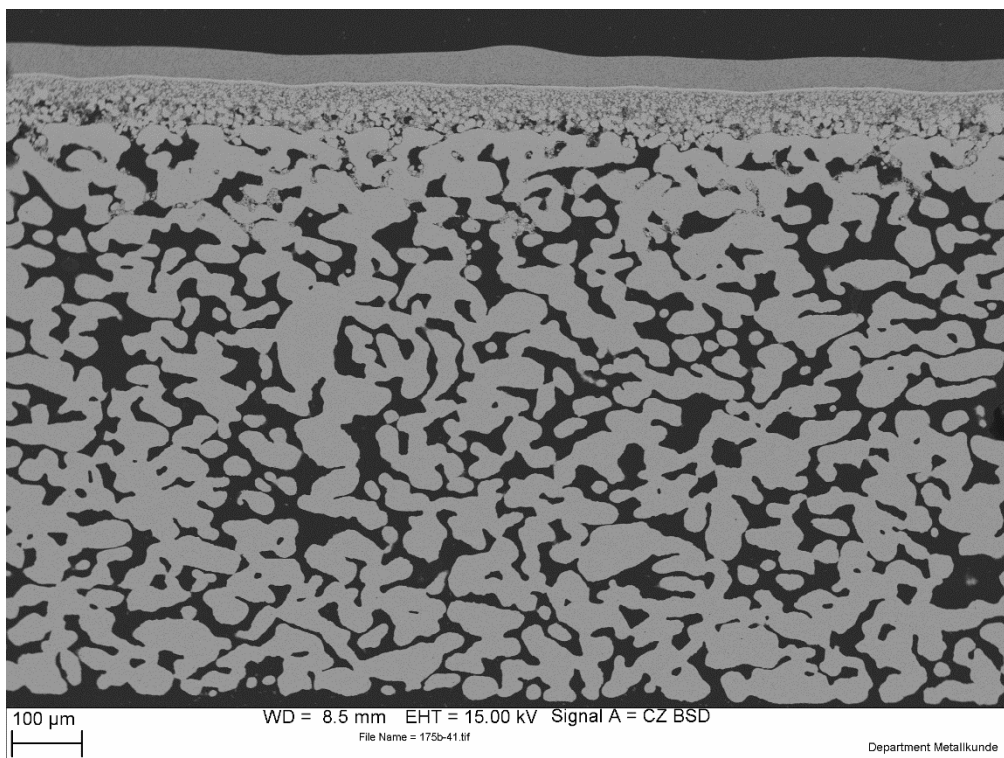


Figure 48: SEM cross section of green sample (LSCF 0); coarsely porous substrate on the bottom; finely porous cathode layer on top

Investigation of the profile shows minor areas of delamination between LSCF cathode layer and GDC diffusion barrier layer. A detailed display of the cathode-DBL interface is shown in Fig.49 with the area of delamination marked (red). The width of the crack measures around 500nm. It is further noted that the layer thickness, especially of the cathode layer varies over the whole surface area of the sample.

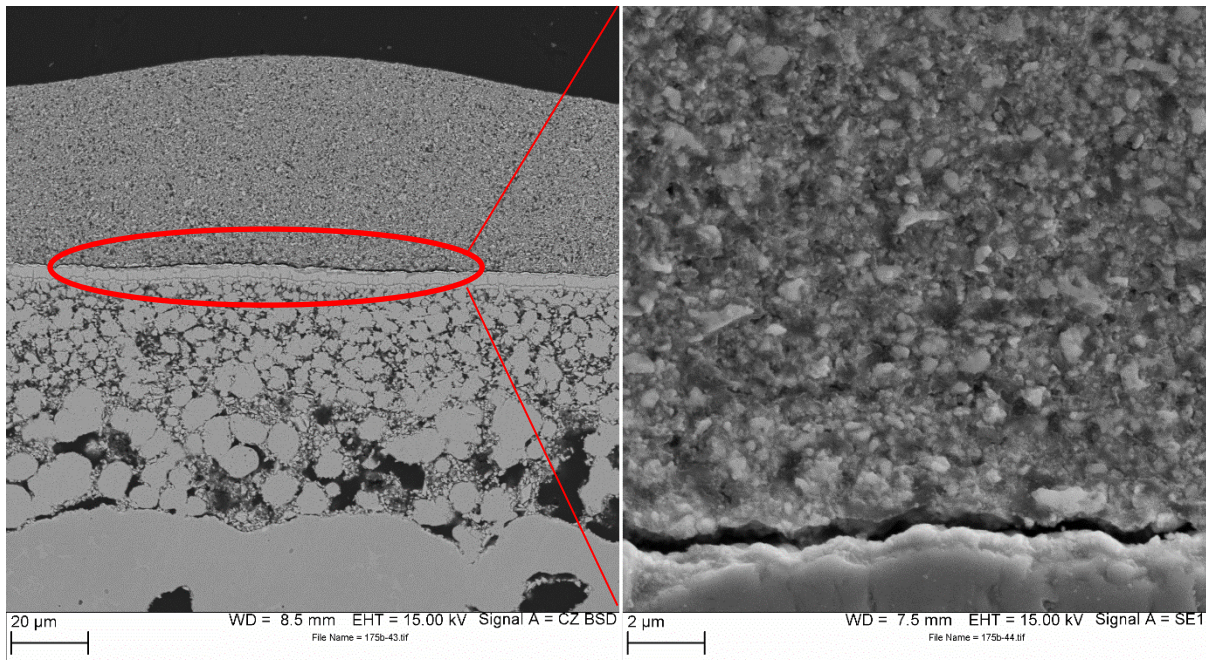


Figure 49: Detail of functional layer interface of LSCF 0 sample with section of delamination marked (left); magnification of delaminated zone (right)

9.3.2. LSCF 1: Reference sample 650°C (1309-005A)

Fig.50 shows a detail of the cross section of the LSCF 1 sample similar to Fig.49. The picture shows extensive delamination of the cathode layer across the sample. The cathode layer has entirely detached from the GDC barrier layer over nearly the entire cell. Comparing the size of the detachment area with Fig.49 the width of the crack has increased from 500nm to around 2μm.

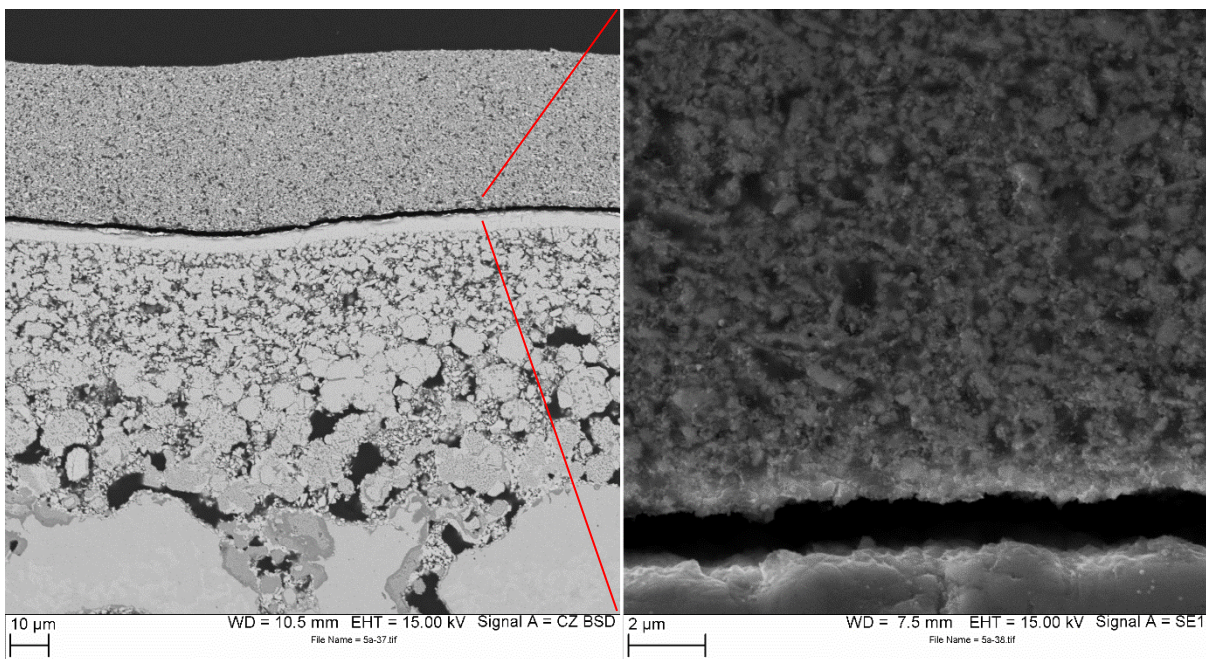


Figure 50: Detail of functional layer interface of LSCF 1 sample with delamination of the cathode across the whole picture (left); magnification of delaminated zone (right)

In Fig.51 a top view of the cathode surface is displayed. The picture reveals several artifacts on the cathode surface (dark spots marked in blue, separate particles marked in green) and also vertical cracks through the cathode layer are visible in the BSD image (red arrows).

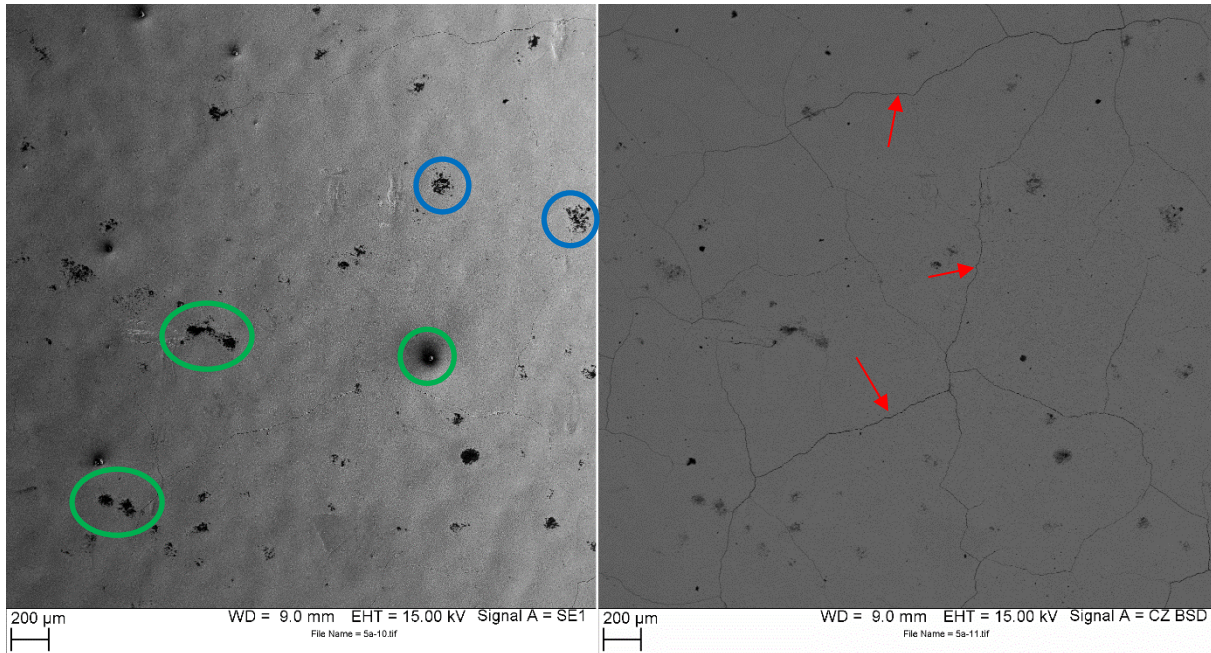


Figure 51: Aerial view of cathode surface of LSCF 1 sample with artifacts spots (blue, green) and vertical cracks (red); SE image (left) and BSD image (right)

Further investigation of the dark spots using EDX spectroscopy revealed them as carbon residues. Fig.52 shows the EDX point spectrum of one such dark spot. Additionally to the characteristic spectrum of the LSCF cathode material containing La, Sr, Co, Fe and O it shows a pronounced peak of carbon to the far left of the plot.

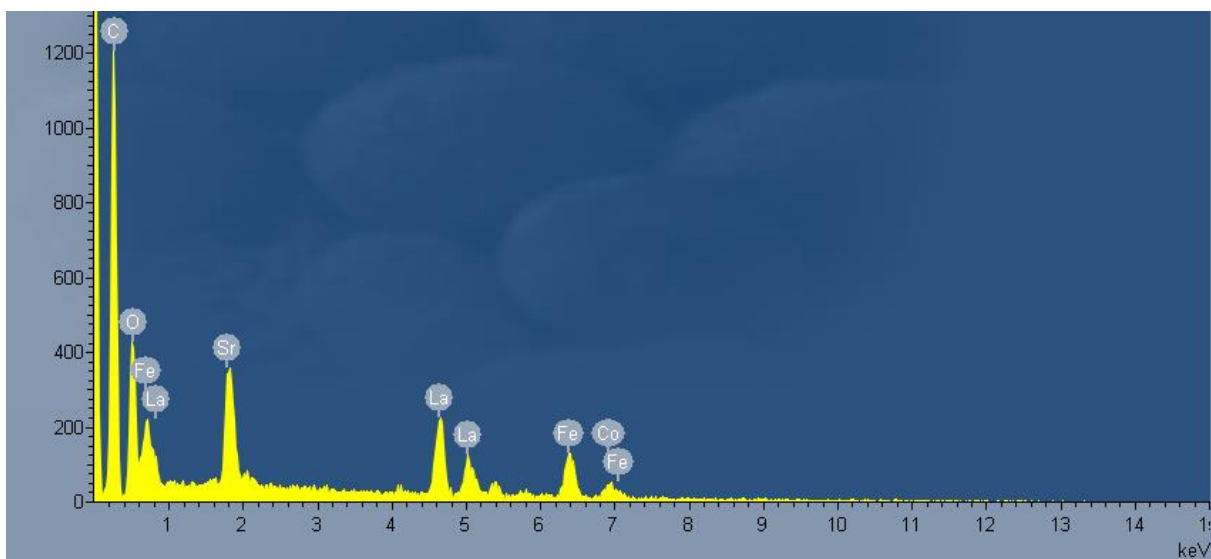


Figure 52: EDX spectrum of dark residues of LSCF 1 sample marked in Fig.51 showing characteristic LSCF pattern with abnormal carbon peak close to 0keV

9.3.3. LSCF 2: Exhaust gas sample 650°C (1309-005B)

Fig.53 shows the cross section SEM picture of the LSCF 2 sample operated with simulated exhaust gas at the cathode side at 650°C. The shot again shows horizontal delamination above the GDC barrier layer and also vertical cracks through the cathode layer. Although the delamination again seems to spread over the entire cell, looking at the magnification of the crack area (Fig.53; right) it appears that the gap between the cathode and the GDC layer is smaller compared to the previous samples (see Fig.50). The vertical cracks pass through the entire cathode layer (red arrow).

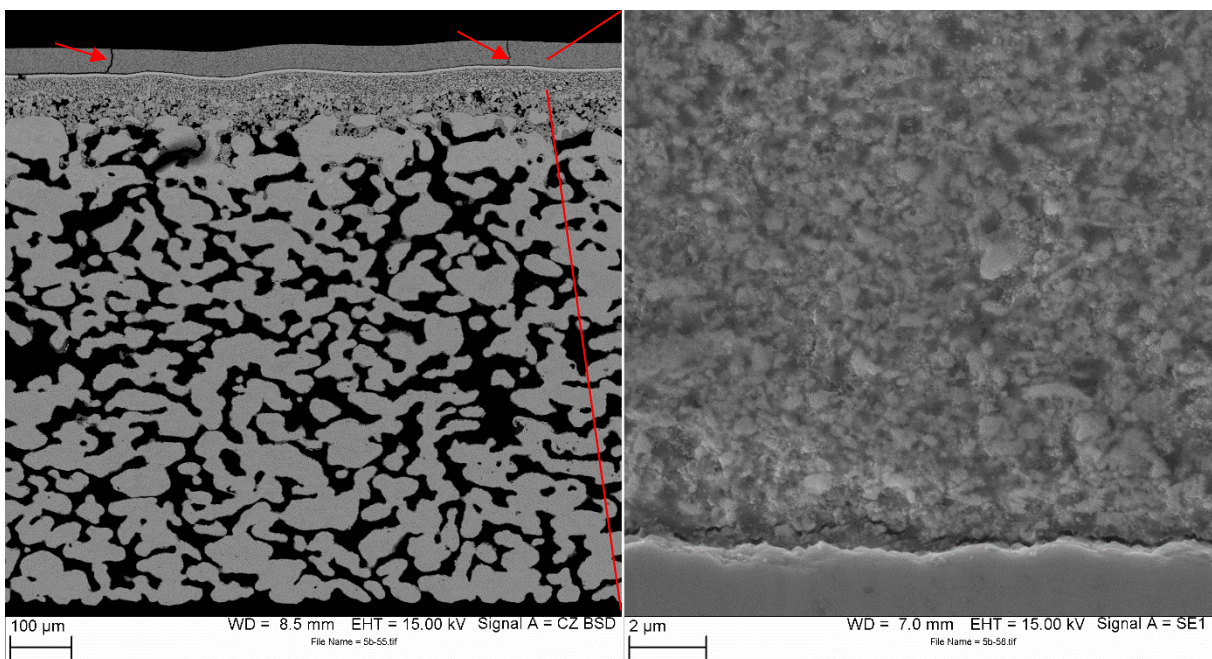


Figure 53: SEM cross section of LSCF 2 sample with horizontal delamination and vertical cracks (red arrow) of the cathode (left); magnification of delaminated zone (right)

Looking at the aerial view of the cathode layer in Fig.54 it shows that the vertical rifts (red arrows) spread over most of the surface. Further there are some imprints visible in the SE image at the bottom right corner (marked in green), supposedly resulting from the Pt-collector grid being weighed down during the prior experiment.

Apart from this partial damage of the cathode there were also some carbon residuals (marked in blue) as described in Fig.51/52 visible on the surface. However the carbon deposition occurs to be less compared to the LSCF 1 sample.

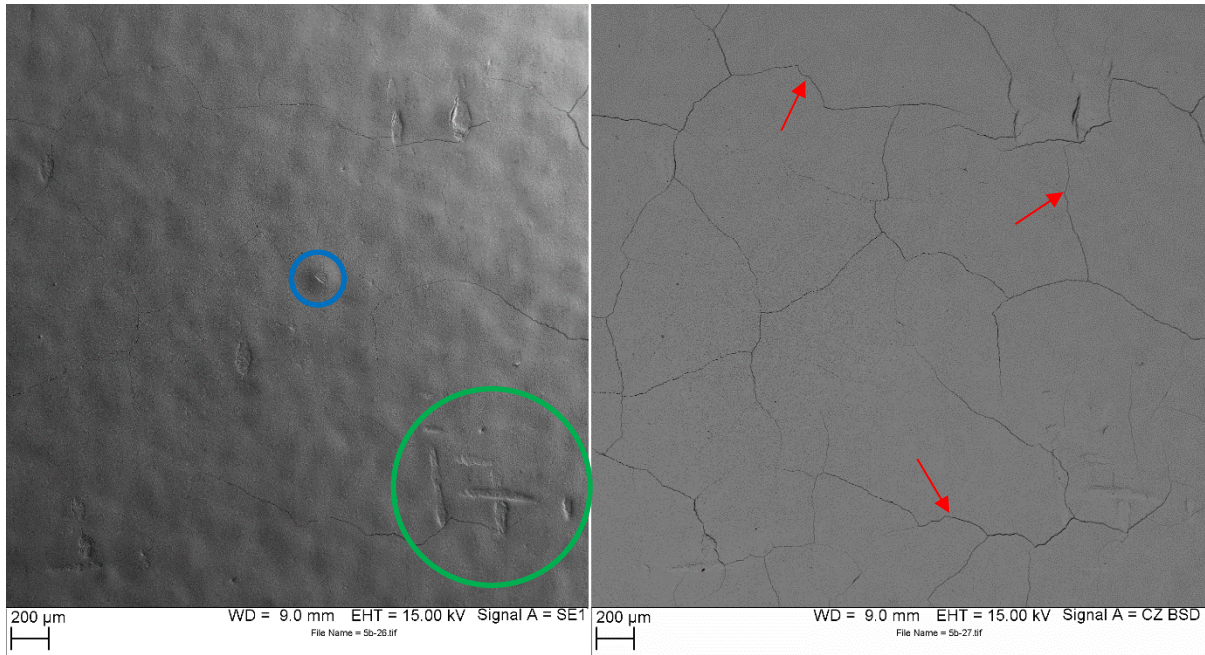


Figure 54: Aerial view of cathode surface of LSCF 2 sample with carbon residuals (blue), imprints from current collector grid (green) and vertical cracks (red); SE image (left) and BSD image (right)

9.3.4. LSCF 3: Exhaust gas sample 500°C (1309-019B)

Fig.55 displays the top view of the cathode surface of the LSCF 3 sample cell. The cathode layer shows vertical cracks (red arrows) spreading over the entire sample size and some spots of carbon deposition (marked in blue) as analysed in Fig.52. Additionally the specimen shows some contaminant particles on the edge of the cell (marked in green)

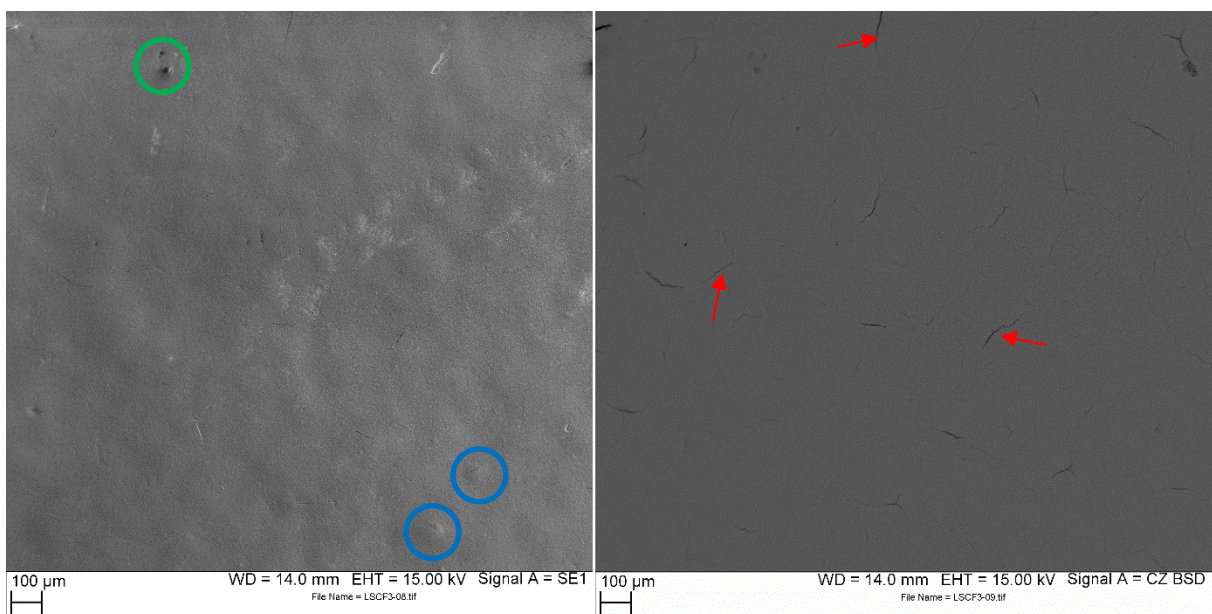


Figure 55: Aerial view of cathode surface of LSCF 3 sample with carbon residuals (blue), artifact particles (green) and vertical cracks (red); SE image (left) and BSD image (right)

Looking at the previous samples the crack pattern has a similar appearance and carbon precipitates show the familiar spot like shape as mentioned before. The particles marked in green appear to be residuals carried over from the earlier cutting process.

Unfortunately due to issues with sample preparation there was no possibility to generate a cross section image of the LSCF 3 and the following LSCF 4 samples.

9.3.5. LSCF 4: Exhaust gas sample 350°C (1309-019A)

In Fig.56 the surface of the cathode of the LSCF 4 sample is displayed. Again the surface shows vertical cracks (red arrows) visible in the BSD image running all over the cathode area and partial spots of carbon deposition (marked in blue) analog to Fig.52 visible in the SE image.

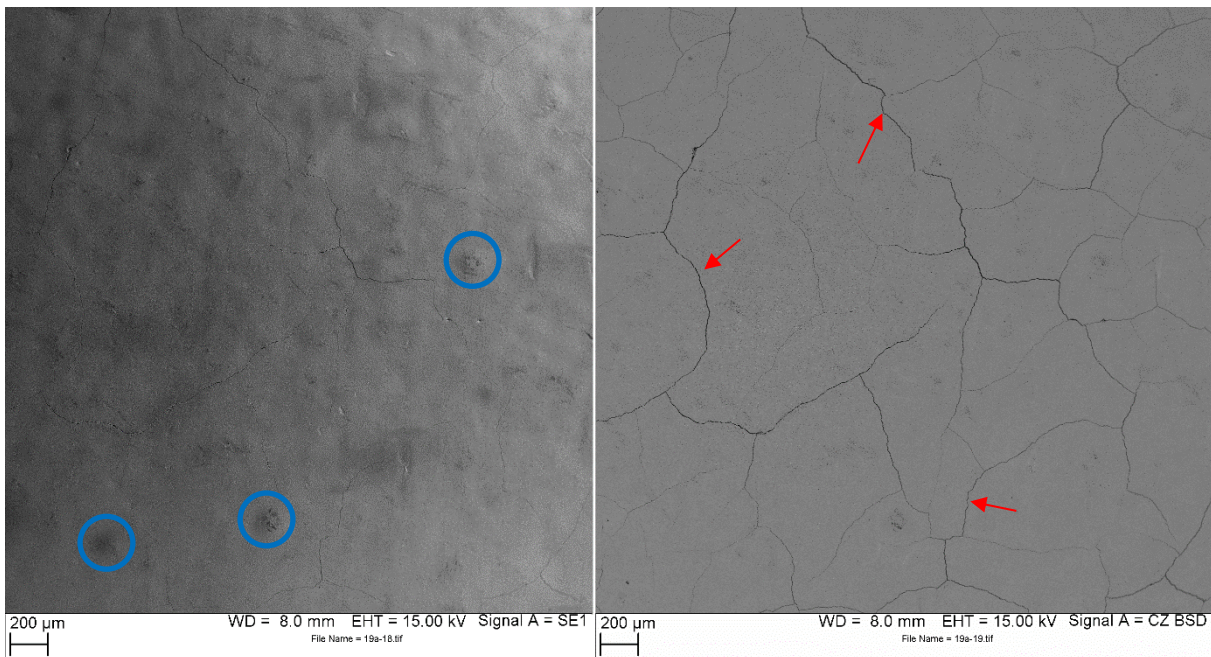


Figure 56: Aerial view of cathode surface of LSCF 4 sample with carbon residuals (blue) and vertical cracks (red); SE image (left) and BSD image (right)

Comparing the images to the previous samples the crack pattern shows similar shape and extension to the other samples, although there appears to be a larger number of carbon deposition spots compared to the two other samples operated with exhaust gas (LSCF 2, LSCF 3).

9.4. Results of XRD-analytics

The last part of the post mortem analytics consists of XRD scans of all five samples focusing on the cathode with the objective to identify possible modifications of the microstructure or formation of secondary phases. The spectra were compared among the individual samples and further checked against the corresponding reference patterns of the International Centre for Diffraction Data (ICDD; status 2018).

9.4.1. Overview of XRD spectra

Fig.57 shows an overview of the cathode spectra of all five specimens. The spectra were recorded across an angle range of $2\Theta=10\dots100^\circ$ with a step size of $\Delta\Theta=0.02^\circ/\text{step}$ and an observation time of $t_{\text{step}}=1\text{sec}/\text{step}$. The patterns show three distinct regions where the signal intensity differs within the individual samples. These three regions of interest magnified in 1, 2 and 3 are to be investigated in more detail. Looking at regions 2 and 3 there is a noticeable correlation of the intensity ratios of the different specimen related to their exposure temperature.

9.4.2. Main phase spectrum

First an identification of the cathode's LSCF-6428 main phase was done. Therefore the XRD-pattern of the unused LSCF 0 (1309-175B) sample was measured in order to rule out any distortion induced by possible artifacts or other secondary phases. Fig.58 shows the recorded spectrum (red) compared to the reference pattern for rhombohedral LSCF-6428 (04-018-2448; blue) from the ICDD data base. The patterns show matching peaks across the entire angle range, hence there is proof for the cathode material to be LSCF-6428. However there is no clear evidence about the orientation of the material. The characteristic reflex setting the rhombohedral phase apart from its cubic counterpart at 38.3° (black arrow) is overlapped by a foreign phase's pattern possibly originating from one of the layers beneath the cathode. The 99%-penetration depth of Cu-K α radiation in fully dense LSCF-6428 measures approximately $36\mu\text{m}$, which can lead to interference taking the porosity of the $50\mu\text{m}$ thick cathode into account[88]. Because of the relatively broad shape of the reflex the resolution of the measurement is insufficient to allow a clear differentiation between the rhombohedral and the cubic system.

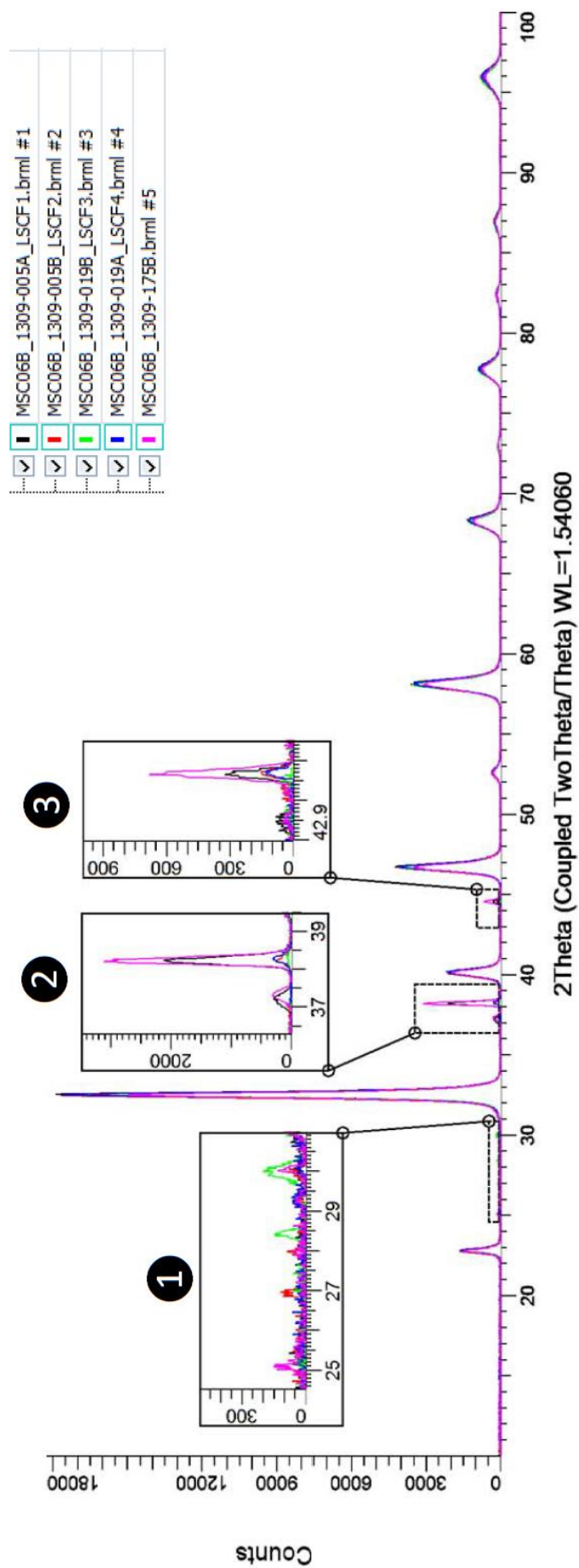


Figure 57: Overview of XRD-spectra of all five samples; regions of differing signal intensity magnified (1, 2 and 3); $2\Theta=10\dots100^\circ$; $\Delta\Theta=0.02^\circ/\text{step}$; $t_{\text{step}}=1\text{sec}/\text{step}$

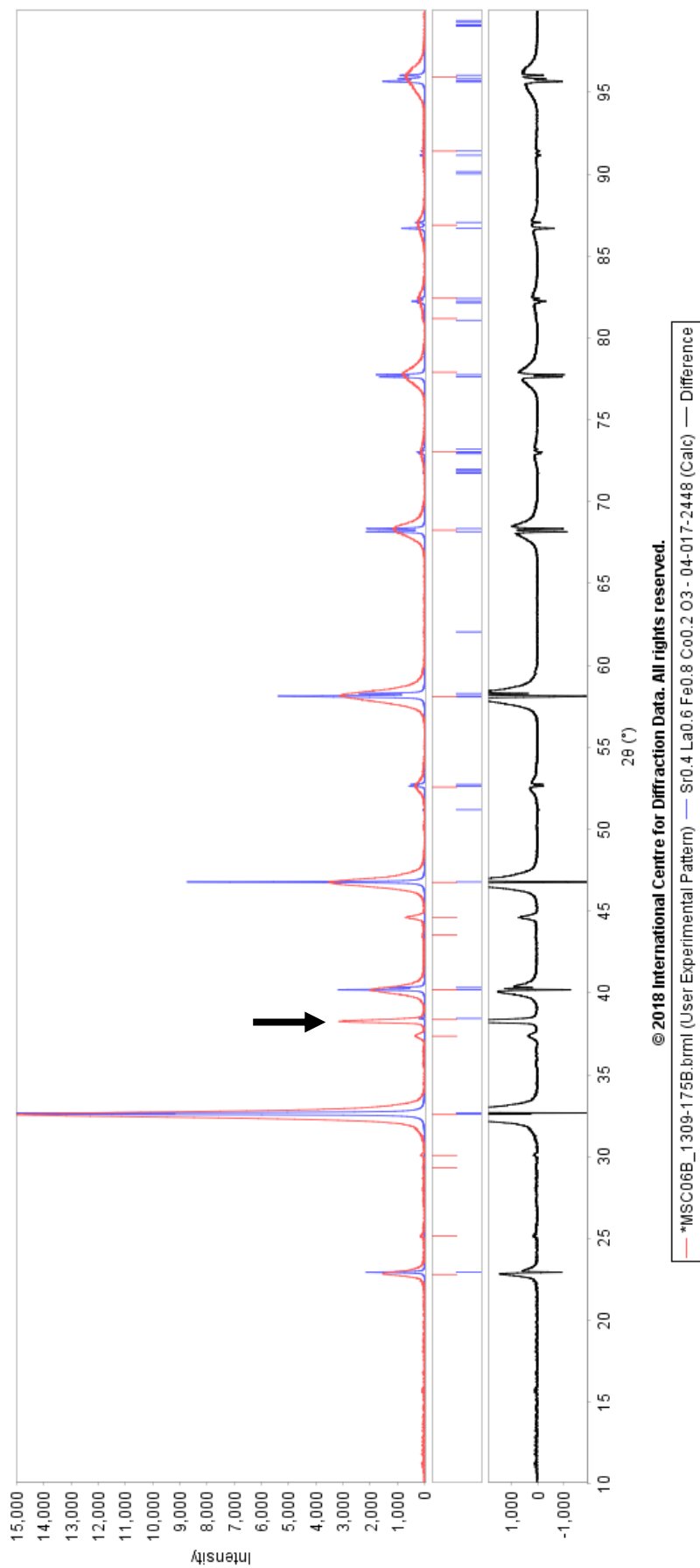


Figure 58: XRD-spectra of LSCF 0 (1309-175B) sample (red) compared to the characteristic pattern for rhombohedral LSCF-6428 (blue) from the ICDD data base; characteristic peak for rhombohedral system marked at 38.3° (black arrow)

9.4.3. Secondary phases section 1 (24-31°)

Next a more detailed investigation of section 1 marked in Fig.57 ranging from $2\Theta=24\text{...}31^\circ$ was done. Fig.59 shows an overlay of the cathode spectra of all five samples within the desired region of interest.

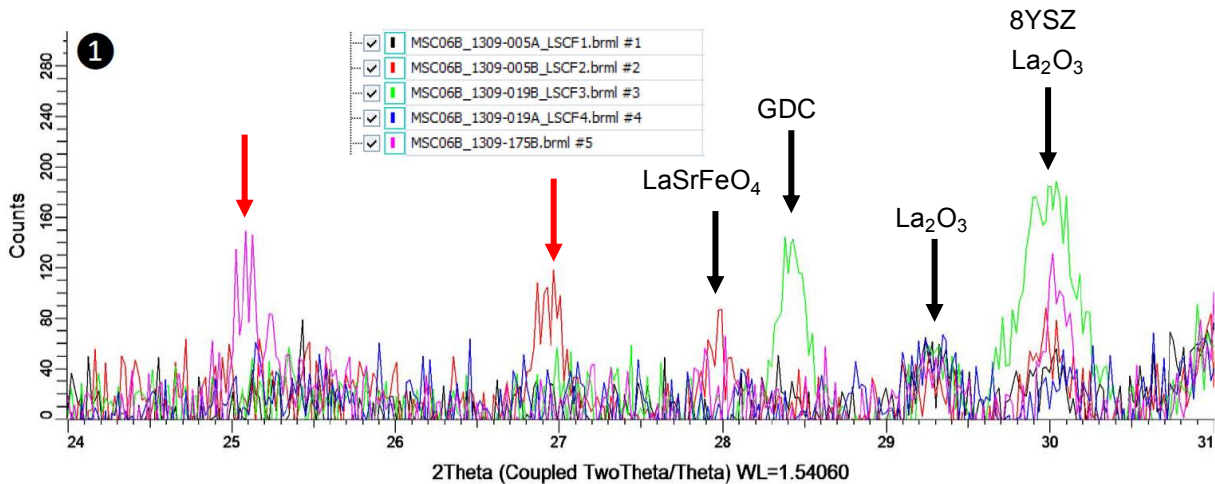


Figure 59: XRD-spectra of all five samples in section 1 ($2\Theta=24\text{...}31^\circ$); identified phases marked in black; not assignable peaks marked in red

The graphs show some divergence of the reflex intensities between the individual samples. The reflexes on the right hand side (marked in black) can be partly assigned to the cathode material and its modifications (La_2O_3 ; LaSrFeO_4) and otherwise to other cell components (GDC diffusion barrier layer; YSZ electrolyte) shining through from the background. However the two peaks at approximately 25° and 27° (marked in red) cannot be assigned to any noted phase yet.

9.4.4. Secondary phases section 2 (36-41°)

The second section of interest marked in Fig.57 reaches from $2\Theta=36\text{...}41^\circ$. Fig.60 displays a detail of the cathode spectra of the five samples in this range together with a spectrum recorded from the ITM-substrate alone. The plot shows a uniform peak of all the samples at around 40.1° representing the LSCF-6428 cathode material. Further the patterns show unusual reflexes at around 37.3° and 38.2° (marked in red). Looking at these areas the intensity of the peaks differ significantly between the fresh sample (LSCF 0), the reference sample (LSCF 1) and the cells operated in exhaust gas atmosphere (LSCF 2-4). At 37.3° the peaks almost completely disappear for the samples LSCF 2-4).

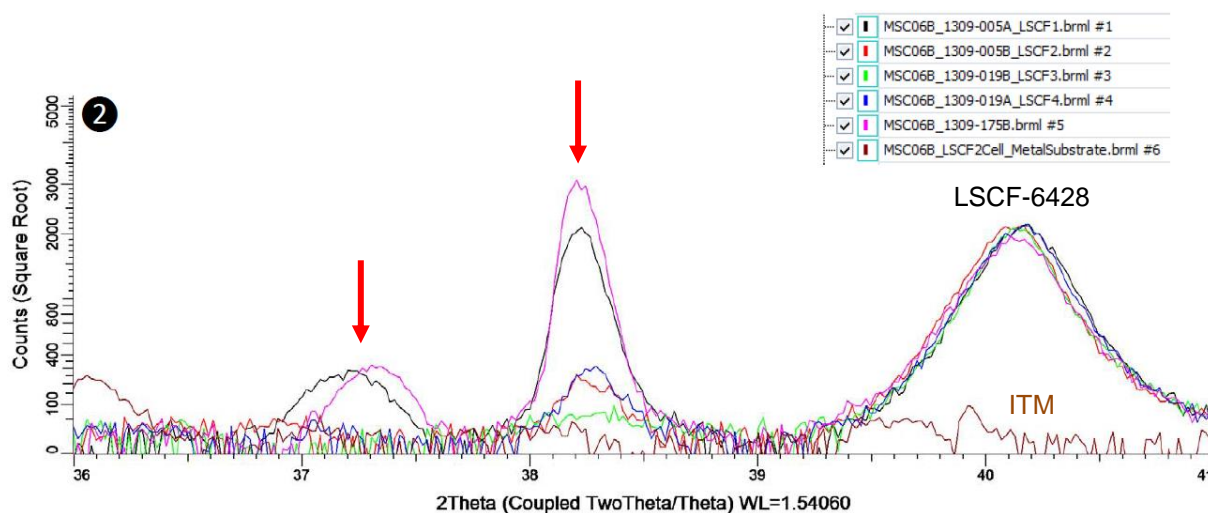


Figure 60: XRD-spectra of all five samples in section 2 ($2\Theta=36\dots41^\circ$); identified LSCF-6428 phase marked in black; not assignable peaks marked in red

The influence of the substrate (brown graph) shining through can be ruled out hence the spectra of the ITM-alloy show no noteworthy change in intensity in this angle range. Nevertheless the fact that the intensity of the reflexes decreases comparing the fresh LSCF 0 sample to the tested samples (LSCF1-4) which also precludes the possibility of formation of new phases or adsorption of artifacts during the exposure period.

9.4.5. Secondary phases section 3 ($42.2\text{-}48^\circ$)

Fig.61 shows a detailed magnification of section 3 marked in Fig.57 ranging from $2\Theta=42.2\dots48^\circ$. The plot again displays the cathode spectra of the five sample cells together with the spectrum of the substrate material (ITM). The collective peak at 46.7° can be assigned to the LSCF-6428 cathode material.

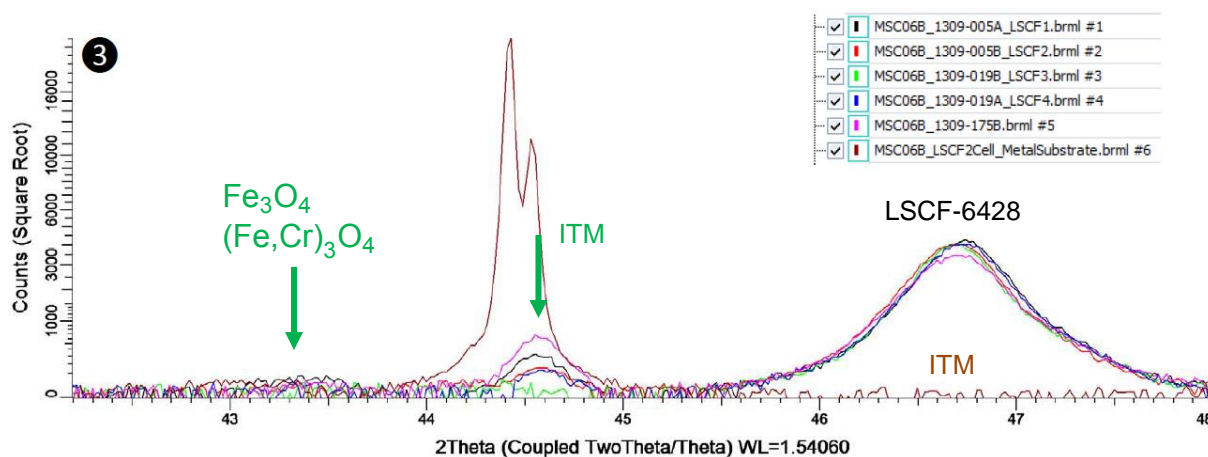


Figure 61: XRD-spectra of all five samples in section 3 ($2\Theta=42.2\dots48^\circ$); identified LSCF-6428 phase marked in black; reflexes passing through from the substrate marked in green

The graphs further show some reflexes at 44.6° and additional less pronounced changes in intensity at 43.4°. Both peaks can be assigned to the ITM-substrate and its modifications reaching through from them background. In detail the reflex at 43.4° can be associated with magnetite (Fe_3O_4) and $(\text{Fe,Cr})_3\text{O}_4$, whereas the one at 44.6° directly correlates with the ITM-material (brown).

9.4.6. Summary of XRD-results

To sum things up the recordings of the XRD-analysis were compared to numerous different patterns of possible secondary phases formed during the operation of the sample cells under the defined operating circumstances. Fig.62 shows the cathode XRD-spectra of the LSCF 1 (operated in air) and the LSCF 2 sample (operated in the defined exhaust gas listed in Table 7) compared against the characteristic patterns of the cathode material and other cell components themselves as well as various secondary phases presumably occurring in the applied testing environment. These possible foreign phases aside from the LSCF-6428 cathode material and its modifications feature substances from different cell layers, such as Ni and NiO (anode), yttrium zirconium oxide (electrolyte), cerium gadolinium oxide (DBL), Pt from the current collector grid as well as possible degradation products, such as La- and Sr-carbonate and hydroxide (mentioned in chapter 6.2.1. and 6.2.2.) and graphite.

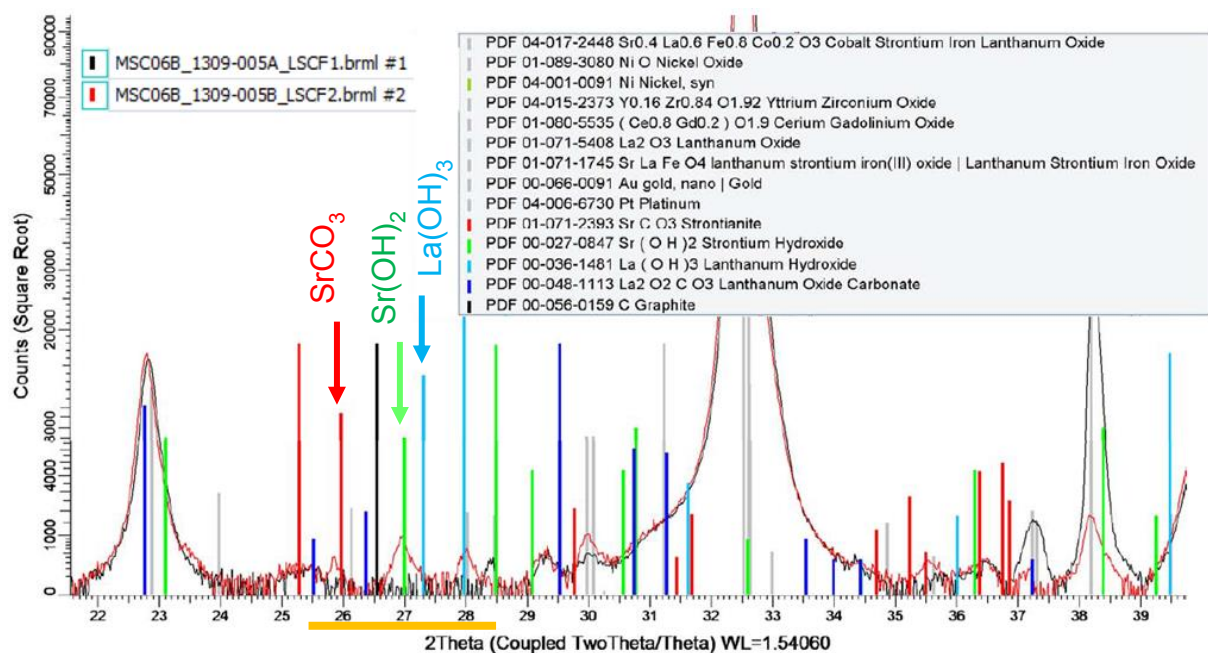


Figure 62: XRD-spectra of LSCF 1 and LSCF 2 sample compared to characteristic patterns of LSCF-6428 and various possible secondary phases

The comparison in Fig.62 reveals a partial match of the recorded sample patterns with the characteristic spectra of other phases, although the interference of the signals with e.g. the cathode material itself makes it difficult to accurately distinguish certain secondary materials. One area of particular interest is located in the range of $2\theta=25.5\dots28^\circ$ (marked in yellow), where the LSCF 2 sample operated in exhaust gas environment (red graph) shows three peaks the LSCF 1 sample operated in air only (black graph) is missing. These reflexes could possibly be assigned to SrCO_3 (marked in red), Sr(OH)_2 (marked in green) and La(OH)_3 (marked in blue). However the partial overlap of certain reflexes with patterns of other cell components and the lack of other characteristic peaks further down the spectrum makes it difficult to clearly identify any degradation inducing phases in particular. Nevertheless the cathode material itself could be successfully identified and other patterns could be matched to further components of the cell structure interfering due to higher penetration depths of the Cu-K α radiation in the porous cathode or being exposed due to the partial delamination of the cathode layer.

10. Roundup and discussion

The emphasis of this thesis was to investigate the behavior of SOFC cathode materials, in particular the most commonly used LSCF in H₂O- and CO₂-containing atmospheres representing the exhaust gas of the combustion of an ethanol-water mixture at different temperatures. Therefore a literature search tailored towards the effects of such extraordinary operating conditions on the cells function was conducted. Further a schedule for a series of cell tests with state-of-the-art MSC samples was developed (see Table 11) in order to distinguish the actual response of such cells. In the course of this limited schedule the focus was on four individual experiments which were successfully executed.

The data recorded throughout the trials show an enhanced drop in power output of the tested cells when operated in H₂O- and CO₂-containing environment at the cathode side compared to normal operation in air. Further the drop in power output increases with decreasing temperature (see Table 12). Looking at the results of the EIS-measurements the decrease in power output corresponds with an increase in resistance displayed in the Nyquist plots of the frequency responses of each tested cell. The plots show a pronounced increase in resistance in the low to mid frequency range throughout the duration of each experiment. Again the increase in resistance was most significant at the sample exposed to the simulated exhaust gas at the lowest temperatures tested at 350°C. Hubert et al. [76] summarize the impact on the change in the frequency responses at low frequencies to be related to the cathode condition, specifically the surface reaction (0.5 to 1Hz), the bulk and solid state transport (5 to 100Hz) and the influence of surface transport and charge transfer reaction (around 1kHz).

Several sources (see [75] to [78]) indicate possible changes in the cathode's microstructure when operated in atmospheres containing H₂O and CO₂ being a potential reason for performance degradation of SOFCs. The probability of hydroxide- and/or carbonate-formation with the cathode's alkaline earth metals (e.g. Sr(OH)₂, SrCO₃) is a harmful factor to LSCF-cathode performance when operated in the presence of H₂O and CO₂ (see Fig.21/22). In particular Yang et al. [89] point out, that the oxygen activity and the surface adsorption of LSCF cathodes is severely affected by the formation of SrCO₃ in such atmospheres. First CO₂ tends to adsorb

to the cathode's surface competing with O_2 and occupies the active oxygen sites impacting the ORR. Moreover carbonate formation is possible due to surface segregation. Additionally Darvish et al. [79] confirms that especially the carbonate formation is more pronounced at lower temperatures (see Fig.24). However due to the fact that such carbonates and hydroxides tend to be more stable at lower temperatures, these performance reducing effects can be reversible at higher temperatures and/or H_2O - and CO_2 -free atmospheres. Altogether these phenomena might be one reason for the performance degradation experienced during the prior cell tests.

In order to dig deeper into the causes for the declining cell performances post mortem analysis containing SEM and XRD investigation of each sample cell was conducted. An optical inspection of the cells after testing illustrated in Fig.47 revealed partial delamination and attachment of the cathode layer to the Pt-current collector grid, which was weighed down and pressed against the cathode surface in order to ensure proper contacting during testing. Further investigation of the cross section revealed delamination of the cathode layer across major parts of the cell across all the tested cells compared to the unused sample only showing minor detachment (see chapter 9.3.). It remains questionable whether this delamination already occurred during the experiments due to thermal and chemical cycling or if it was a result of disassembling the test setup and removing the cell of the test bed after each trial. Nevertheless such delamination could substantially influence the cell performance during operation. Additionally the samples showed smaller vertical cracks in the cathode layer across the entire surface possibly caused by thermal cycling too, hence there were no side loads applied to the samples throughout the experiments. There were also foreign particles and spots of carbon enrichment found on the cells surface (see Fig.51/52). These particles (mostly present on the LSCF 1 sample's surface) potentially placed there during the cutting process prior to the post mortem analysis, which was drastically improved for later samples in order to shield the specimens from any kind of debris.

The carbon containing residuals however were found on every single investigated cell surface, even on the LSCF 1 sample which was operated solely in pure air and therefore unlikely originate from the CO_2 -application. They are more likely a result of possible impurities in the media supply at the test bed e.g. lubricant residuals from

valves or compressors. Another reason for these spots could be remains of the binder used for the screen printing process during the cell fabrication still being present on the cathode surface after the in-situ sintering at relatively low temperatures of 850°C. Therefore it is doubtful whether they contributed to the monitored degradation of the cells.

In the course of the finalizing XRD-investigation a broad spectrum of reflexes was recorded. The LSCF-6428 main phase could successfully be identified (see Fig.58) and was still mostly intact after the experiments. The recorded patterns also showed a wide degree of interference with other cell layers, such as the ITM-substrate, the diffusion barrier layers, the anode and the electrolyte. Further cathode related secondary phases, such as La_2O_3 and LaSrFeO_4 were also identified. Looking for degradation inducing phases there were some interesting reflexes found on the samples operated with the simulated exhaust gas in the range of $2\Theta=25.5\dots28^\circ$ (see Fig.62), which could possibly belong to some of the mentioned carbonate- and hydroxide phases formed during the exposure. However the high degree of interference and the absence and/or the possible overlap of other characteristic peaks of such phases makes it difficult to entirely prove the presence of those phases.

This interference caused by the fact, that the penetration depth of the Cu-K α radiation partially exceeds the thickness of the cathode layer has to be considered. Due to slight deviation in the height of the cells fragments a 2Θ -angle azimuth in the range of 0.1° has to be taken into account as well. These phenomena limit the resolution of the powder diffractometry and therefore do not allow a more accurate determination of secondary phases. Also the partial delamination of the samples seen in the SEM-images further limits the accuracy of the investigation.

11. Conclusion and prospect

The objective of this thesis was to investigate the behavior of state-of-the-art SOFCs under the presence of H₂O- and CO₂-containing gases at the cathode side in order to replicate the heatup process using a burner combusting an ethanol-water mixture. With that in mind a testing schedule was developed and a series of four experiments was executed using the current cell design provided by Plansee SE® with LSCF-6428 cathode material. The targeted program was successfully executed. All the tested cells experienced a certain degree of power loss over the exhaust gas exposure period with a corresponding increase in resistance visible in the impedance spectra. The degradation was more severe toward at lower temperatures, which is in line with already existing literature. The maximum drop in power output was recorded at around 20% after an 80h exposure to the defined exhaust gas at 350°C. Nevertheless all the tested samples were still functional after testing, although visual inspection after each trial showed partial delamination of the cathode layer of the cells after disassembling from the test setup, possibly caused by adhesion of the current collector grid during the in situ sintering process of the cathode.

The following post mortem analysis using SEM and XRD techniques revealed substantial macroscopic damage in the form of major delamination of the cathode layer and smaller vertical cracks across the cathode layer. Moreover carbon-containing accumulations were found on the cathode surface, potentially being residuals of the binder used during cell fabrication, in particular the screen printing process of the cathode layer. The fact that these carbon containing spots were also found on unused new cells rules almost certainly out that their appearance is a result of the testing conditions. An alternative reason for the depositions according to Blum et al. [90] could be impurities carried in the air supply at the test stand. Moreover the degradation monitored during testing is more likely caused by the macroscopic cell damage in the form of cracks. A more in depth XRD-investigation of the cathode layer revealed a high degree of interference of the signal originating from subjacent cell layers in combination with the partial cathode delamination detected in the SEM-analysis. However the intact cathode phase could be identified amongst other cell components. There was presumption of secondary phase formation in the form of carbonates and hydroxides in the presence of H₂O and CO₂ according to several sources, and indeed some reflexes were found in the XRD-pattern possibly indicating

such phenomena. Nonetheless the high degree of interference combined with the restricted accuracy of the analytics makes it difficult to clearly identify any further secondary phases.

In conclusion it is stated that the tested cells experience enhanced degradation in an environment containing H₂O and CO₂. The drop in power is more pronounced towards lower temperatures, which correlates with existing literature suggesting carbonate and hydroxide formation as cause. Regardless the macroscopic changes (delamination, cracks) seem to outweigh such microstructural changes when it comes to influencing power degradation. In order to prove the formation of such microscopic secondary phase, a more precise analysis also including high resolution EDX scans or XRD-investigation of single cathode fragments would be necessary.

For future applications regarding the heatup strategy of an APU-system it is further of great interest whether or not such performance losses are reversible during standard operation. Stability studies conducted by Egger [91] indicate, that especially the suspected carbonates are less stable at elevated temperatures (see Fig.63, chapter 15. Appendix) and possibly decay again after the successful startup. In order to estimate the influence of the temperature changes on cell degradation to a greater extent a more extensive testing schedule including additional reference samples for each temperature level should be developed. Moreover other difficulties have to be taken into account when supplying a complete stack of fuel cells with the exhaust gas of a burner introducing major temperature gradients and thermal loads to the assembly possibly resulting in irreversible damage and sealing issues. To sum facts up, the results presented in this thesis contain several possible phenomena which are likely to occur during a heatup scenario and therefore require careful consideration.

12. References

- [1] U.S. Department of Energy, *Fuel Cell Handbook (Seventh Edition)*, EG&G Technical Services, Inc., November 2004
- [2] H. Eichseder, M. Klell, *Wasserstoff in der Fahrzeugtechnik – Erzeugung, Speicherung, Anwendung (3. Auflage)*, Springer Vieweg, 2010
- [3] E. Ivers-Tiffée, A. Weber, D. Herbstritt, *Materials and technologies for SOFC-components*, Institut für Werkstoffe der Elektrotechnik IWE, Universität Karlsruhe (TH), December 2000
- [4] U.S. Department of Energy, *Comparison of Fuel Cell Technologies*, Fuel Cell Technology Office, www.hydrogenandfuelcells.energy.gov., April 2016
- [5] A. A. Buldain, *Stability studies of critical components in SOFC technologies*, Doctoral School in Materials Science and Engineering, University of Trento, April 2013
- [6] J. Mathé, Operating temperatures for SOFCs, personal communication, November 2017
- [7] V. V. Krishnan, *Recent developments in metal-supported solid oxide fuel cells*, WIREs Energy Environ 2017
- [8] J. Mathé, *Sulfur poisoning of solid oxide fuel cells*, Institut für Chemische Technologien und Analytik, Technische Universität Wien
- [9] J. Rechberger, M. Reissig, M. Hauth, P. Prenninger, *SOFC System Development*, AVL List GmbH, June 2012
- [10] Nissan Motor Co., Ltd., *Nissan Solid-Oxide Fuel Cell Vehicle Specification*, <http://nissannews.com/en-US/nissan/usa/releases/nissan-unveils-world-s-first-solid-oxide-fuel-cell-vehicle>, March 8th, 2018
- [11] G. Rabenstein, V. Hacker, *Hydrogen for fuel cells from ethanol by steam-reforming, partial-oxidation and combined auto-thermal reforming: A thermodynamic analysis*, Christian Doppler Laboratory for Fuel Cell Systems. Graz University of Technology, August 2008

- [12] J. Rechberger, F. Moradi, *AVL Fuel Cell*, AVL List GmbH, June 2017
- [13] AVL List GmbH, *Flowsheet Nissan APU*, February 2017
- [14] P. Satardekar, *Materials Development for the Fabrication of Metal Supported-Solid Oxide Fuel Cells by Co-sintering*, Doctoral School in Materials Science and Engineering, University of Trento, September 2014
- [15] N. P. R. Frank, *Umsetzung von Kohlenwasserstoffen in SOFCs*, Fakultät für Maschinenwesen, Technische Universität München, December 2009
- [16] S. C. Singhal, K. Kendall, *High Temperature Solid Oxide Fuel Cells – Fundamentals, Design and Applications*, Elsevier Ltd., 2003
- [17] S. J. McPhail, L. Leto, C. B. Muñoz, *The Yellow Pages of SOFC Technology International Status of SOFC deployment 2012-2013*, IEA, December 2013
- [18] J. Yuan, *Solid Oxide Fuel Cells (SOFCs)*, Department of Energy Sciences, Lund Institute of Technology (LTH), November 2008
- [19] M. C. Tucker, *Progress in metal-supported solid oxide fuel cells: A review*, Journal of Power Sources, Volume 195, Issue 15, August 2010
- [20] T. Franco, M. Haydn, R. Mücke, A. Weber, M. Rüttinger, O. Büchler, S. Uhlenbruck, N. H. Menzler, A. Venskutonis, L. S. Sigl, *Development of Metal-Supported Solid Oxide Fuel Cells*, The Electrochemical Society, 2011
- [21] M. Rüttinger, R. Mücke, T. Franco, O. Büchler, N. H. Menzler, A. Venskutonis, *Metal-Supported Cells with Comparable Performance to Anode-Supported Cells in Short-Term Stack Environment*, The Electrochemical Society, 2011
- [22] T. Klemenso, J. Nielsen, P. Blennow, A. Persson, T. Stegk, P. Hjalmarsson, B. Christensen, S. Sonderby, J. Hjelm, S. Ramousse, *Development of Long-Term Stable and High-Performing Metal-Supported SOFCs*, The Electrochemical Society, 2011
- [23] N. Christiansen, S. Primdahl, M. Wandel, S. Ramousse, A. Hagen, *Status of the Solid Oxide Fuel Cell Development at Topsoe Fuel Cell A/S and DTU Energy Conversion*, The Electrochemical Society, 2013

- [24] P. Blennow, J. Hjelm, T. Klemensø, S. Ramousse, A. Kromp, A. Leonide, A. Weber, *Manufacturing and characterization of metal-supported solid oxide fuel cells*, Journal of Power Sources, Volume 196, Issue 17, September 2011
- [25] G. Schiller, *Progress in Metal-Supported Solid Oxide Fuel Cells*, German Aerospace Center (DLR), Institute of Technical Thermodynamics, March 2011
- [26] P. K. Moon, H. L. Tuller, *Solid State Ionics 1988*
- [27] S. Wang, T. Kato, S. Nagata, T. Kaneko, N. Iwashita, T. Honda, M. Dokiya, *Solid State Ionics 2002*
- [28] T. Ishihara, H. Matsuda, Y. Takita, *Doped LaGaO₃ Perovskite Type Oxide as a New Oxide Ionic Conductor*, J. Am. Chem. Soc 116, May 1994
- [29] K. Yamaji, T. Horita, M. Ishikawa, N. Sakai, H. Yokokawa, *Solid State Ionics 1999*
- [30] M. Yashima, M. Kakihana, M. Yoshimura, *Metastable-stable phase diagrams in the zirconia-containing systems utilized in solid-oxide fuel cell application*, Solid State Ionics, Volumes 86-88, July 1996
- [31] J. A. Kilner, M. Burriel, *Materials for Intermediate-Temperature Solid-Oxide Fuel Cells*, Department of Materials, Imperial College London, April 2014
- [32] T. A. Ramanarayanan, W. L. Worrell, H. L. Tuller, *Proceedings of the Second International Symposium on Ionic and Mixed Conducting Ceramics*, The Electrochemical Society, 1994
- [33] P. I. Cowin, C. T. G. Petit, R. Lan, J. T. S. Irvine, S. Tao, *Recent Progress in the Development of Anode Materials for Solid Oxide Fuel Cells*, Advanced Energy Materials, May 2011
- [34] W. Z. Zuh, S. Deevi, *A Review on the Status of Anode Materials for Solid Oxide Fuel Cells*, Materials Science and Engineering, December 2003
- [35] T. Kawada, J. Mizusaki, *Current electrolytes and catalysts*, Handbook of Fuel Cells, December 2010

- [36] C. Sun, R. Hui, J. Roller, *Cathode materials for solid oxide fuel cells: a review*, Journal Solid State Electrochemistry, 2010
- [37] S. P. Jiang, *A comparison of O₂ reduction reactions on porous (La,Sr)MnO₃ and (La,Sr)(Co,Fe)O₃ electrodes*, Solid State Ionics, Volume 146, Issues 1-2, January 2002
- [38] H. Ullmann, N. Trofimenko, F. Tietz, D. Stöver, A. Ahmad-Khanlou, *Correlation between thermal expansion and oxide ion transport in mixed conducting perovskite-type oxides for SOFC cathodes*, Solid State Ionics, Volume 138, Issues 1-2, December 2000
- [39] Y. Teraoka, H. M. Zhang, K. Okamoto, N. Yamazoe, *Mixed ionic-electronic conductivity of La_{1-x}Sr_xCo_{1-y}Fe_yO_{3-δ} perovskite-type oxides*, Materials Research Bulletin 1988
- [40] L.- W. Tai, M. M. Nasrallah, H. U. Anderson, D. M. Sparlin, S. R. Sehlin, *Structure and electrical properties of La_{1-x}Sr_xCo_{1-y}Fe_yO₃. Part 1. The system La_{0.8}Sr_{0.2}Co_{1-y}Fe_yO₃*, Solid State Ionics, Volume 76, Issues 3-4, March 1995
- [41] R. Chiba, F. Yoshimura, Y. Sakurai, *An investigation of LaNi_{1-x}Fe_xO₃ as a cathode material for solid oxide fuel cells*, Solid State Ionics, Volume 124, Issues 3-4, September 1999
- [42] E. Siebert, A. Hammouche, M. Kleitz, *Electrochimica Acta*, Volume 40, Issue 11, August 1995
- [43] M. J. Jørgensen, M. Mogensen, *Journal of The Electrochemical Society*, Volume 148, 2001
- [44] F. S. Baumann, J. Fleig, H.- U. Habermeier, J. Maier, *Impedance spectroscopic study on well-defined (La,Sr)(Co,Fe)O_{3-δ} model electrodes*, Solid State Ionics, Volume 177, Issues 11-12, April 2004
- [45] J. M. Serra, V. B. Vert, M. Betz, V. A. C. Haanappel, W. A. Meulenbergh, F. Tietz, *Screening of A-Substitution in the System A_{0.68}Sr_{0.3}Fe_{0.8}Co_{0.2}O_{3-δ} for SOFC Cathodes*, Journal of The Electrochemical Society, Volume 155, 2008

- [46] J. Fleig, *Solid Oxide Fuel Cell Cathodes: Polarization Mechanisms and Modeling of the Electrochemical Performance*, Annual Review of Materials Research, Volume 33, August 2003
- [47] T. Ishihara, *Perovskite Oxide for Solid Oxide Fuel Cells*, Springer, 2009
- [48] A. J. McEvoy, *Activation processes, electrocatalysis and operating protocols enhance SOFC performance*, Solid State Ionics, Volume 135, Issues 1-4, November 2000
- [49] B. A. Boukamp, *Fuel cells: The amazing perovskite anode*, Nature Materials, 2003
- [50] O. Muller, R. Roy, *The major ternary structural families. Crystal Chemistry of Non-Metallic Materials*, Volume 4, Springer, 1975
- [51] J. Philibert, *Atom movements – Diffusion and mass transport in solids*, Université de Paris-Sud, 1991
- [52] J. A. Kilner, R. A. De Souza, I. C. Fullarton, *Surface exchange of oxygen in mixed conducting perovskite oxides*, Solid State Ionics, Volumes 86-88, July 1996
- [53] R. A. De Souza, R. Armand, *Ionic transport in acceptor-doped perovskites*, Imperial College London, 1996
- [54] J. A. M. Van Roosmalen, R. B. Helmholtz, E. H. P. Cordfunke, H. Zandberg, *The defect chemistry of $\text{LaMnO}_{3+\delta}$. 2. Structural aspects of $\text{LaMnO}_{3+\delta}$* , National Centre for High Resolution Electron Microscopy, Delft University of Technology, 1992
- [55] M. Balkanski, T. Takahashi, H. L. Tuller, *Solid State Ionics*, International Conference on Advanced Materials, North-Holland, 1992
- [56] J. Mizusaki, *Nonstoichiometry, diffusion, and electrical properties of perovskite-type oxide electrode materials*, Solid State Ionics, Volume 52, Issues 1-3, May 1992

- [57] R. A. De Souza, J. A. Kilner, *Oxygen transport in $La_{1-x}Sr_xMn_{1-y}Co_yO_{3\pm\delta}$ perovskites Part I. Oxygen tracer diffusion*, Solid State Ionics, Volume 106, February 1998
- [58] S. J. Benson, *Oxygen transport and degradation processes in mixed conducting perovskites*, London University, 2002
- [59] Y. Yu, H. Luo, D. Cetin, X. Lin, K. Ludwig, U. Pal, S. Gopalan, S. Basu, *Effect of atmospheric CO₂ on surface segregation and phase formation in $La_{0.6}Sr_{0.4}Co_{0.2}Fe_{0.8}O_{3-\delta}$ thin films*, Applied Surface Science, April 2014
- [60] G. Ch. Kostoglou, Ch. Ftikos, *Properties of A-site-deficient $La_{0.6}Sr_{0.4}Co_{0.2}Fe_{0.8}O_{3-\delta}$ -based perovskite oxides*, Solid State Ionics, Volume 126, Issues 1-2. November 1999
- [61] A. Mai, V. A. C. Haanappel, F. Tietz, *A-site deficient lanthanum ferrites as cathode materials for SOFCs*, Electrochemical Society High Temperature Materials, 2005
- [62] P. M. da Costa Almeida, *Formation of Lanthanum Zirconates in Solid Oxide Electrolysis Cells*, RES – the School for Renewable Energy Science, University of Iceland, University of Akureyri, February 2009
- [63] V. Dusastre, J. A. Kilner, *Optimisation of composite cathodes for intermediate temperature SOFC applications*, Solid State Ionics, Volume 126, Issues 1-2, November 1999
- [64] B. C. H. Steele, *Survey of materials selection for ceramic fuel cells II. Cathodes and anodes*, Solid State ionics, Volumes 86-88, Part 2, July 1996
- [65] X. Meng, S. Lü, Y. Ji, T. Wie, Y. Zhang, *Characterization of $Pr_{1-x}Sr_xCo_{0.8}Fe_{0.2}O_{3-\delta}$ ($0.2 \leq x \leq 0.6$) cathode materials for intermediate-temperature solid oxide fuel cells*, Journal of Power Sources, Volume 183, Issue 2, September 2008
- [66] M. T. Colomer, B. C. H. Steele, J. A. Kilner, *Structural and electrochemical properties of the $Sr_{0.8}Ce_{0.1}Fe_{0.7}Co_{0.3}O_{3-\delta}$ perovskite as cathode material for ITSOFCs*, Solid State Ionics, Volume 147, Issues 1-2, March 2002

- [67] Z. Shao, S. M. Haile, *A high-performance cathode for the next generation of solid-oxide fuel cells*, Nature 431, February 2004
- [68] H. Yokokawa, H. Tu, B. Iwanschitz, A. Mai, *Fundamental mechanisms limiting solid oxide fuel cell durability*, Journal of Power Sources, Volume 182, February 2008
- [69] E. Bucher, *Degradation mechanisms for SOFC cathode materials*, Montanuniversität Leoben, personal communication – Email, October 24th, 2016
- [70] S. C. Singhal, J. Mizusaki, *Solid oxide fuel cells IX: (SOFC-IX): proceedings of the International Symposium*, Electrochemical Society, 2005
- [71] A. Mai, M. Becker, W. Assenmacher, F. Tietz, D. Hathiramani, E. Ivers-Tiffée, D. Stöver, W. Mader, *Time-dependent performance of mixed-conducting SOFC cathodes*, Solid State Ionics, Volume 177, Issues 19-25, October 2006
- [72] S. Linderoth, A. Smith, N. Bonanos, A. Hagen, L. Mikkelsen, K. Kammer, D. Lybye, P. V. Hendriksen, F. W. Poulsen, M. Morgensen, W. G. Wang, *Proceedings of the 26th Riso International Symposium on Materials Science*, Risø National Laboratory, September 2005
- [73] I. Kaus, K. Wiik, *Stability of SrFeO₃-Based Materials in H₂O/CO₂-Containing Atmospheres at High Temperatures and Pressures*, Department of Materials Science and Engineering, Norwegian University of Science and Technology, Trondheim, 2007
- [74] C. Endler-Schuck, *Alterungsverhalten mischleitender LSCF Kathoden für Hochtemperatur-Festoxid-Brennstoffzellen (SOFCs)*, Institut für Werkstoffe der Elektrotechnik, Karlsruher Institut für Technologie, Band 19, 2010
- [75] J. Hardy, J. Stevenson, T. Singh, M. Mahapatra, E. Wachsman, *Effects of Humidity on Solid Oxide Fuel Cell Cathodes*, U.S. Department of Energy, March 2015

- [76] M. Hubert, J. Laurencin, P. Cloetens, J.C. da Silva, F. Lefebvre-Joud, P. Bleuet, A. Nakajo, E. Siebert, Role of microstructure on electrode operating mechanisms for mixed ionic electronic conductors: From synchrotron-based 3D reconstruction to electrochemical modeling, *Solid State Ionics*, Volume 294, 2016
- [77] R. R. Liu, S. H. Kim, S. Taniguchi, T. Oshima, Y. Shiratori, K. Ito, K. Sasaki, Influence of water vapor on long-term performance and accelerated degradation of solid oxide fuel cell cathodes, *Journal of Power Sources*, Volume 196, August 2010
- [78] S. Darvish, Y. Zhong, S. Gopalan, *Thermodynamic Stability of $La_{0.6}Sr_{0.4}Co_{0.2}Fe_{0.8}O_{3\pm\delta}$ in Carbon Dioxide Impurity: A Comprehensive Experimental and Computational Assessment*, Electrochemical Society, 2017
- [79] S. Darvish, S. Gopalan, Y. Zhong, *Thermodynamic stability maps for the $La_{0.6}Sr_{0.4}Co_{0.2}Fe_{0.8}O_{3\pm\delta}$ -CO₂-O₂ system for application in solid oxide fuel cells*, *Journal of Power Sources*, Volume 336, October 2016
- [80] ABHS Science, *Combustion of Ethanol*, <https://abhsscience.wikispaces.com/Combustion+of+Ethanol>, March 8th, 2018
- [81] V. Lawlor, Operating boundary conditions for cell tests, personal communication – Email, December 27th, 2016
- [82] W. Schafbauer, Cell data for sample cells, Plansee SE, personal communication – Email, July 6th, 2017
- [83] V. Vasechko, G. Pećanac, B. Kuhn, J. Malzbender, Mechanical properties of porous ITM alloy, *International Journal of Hydrogen Energy*, Volume 41, Issue 1, January 2016
- [84] W. Schafbauer, Cell build up for sample cells, Plansee SE, personal communication – Email, July 6th, 2017
- [85] EBZ Entwicklungs und Vertriebsgesellschaft Brennstoffzelle mbH, *Handbuch SOFC Teststand*, Version 1.1, July 2012

- [86] EBZ Entwicklungs und Vertriebsgesellschaft Brennstoffzelle mbH, *Test Rigs*, <http://www.ebz-dresden.de/fuel-cells/test-rigs/>, March 8th, 2018
- [87] E. Bucher, Failure modes of LSCF cathodes, personal document – Email, October 24th, 2016
- [88] A. Egger, E. Bucher, XRD-Analysen von La_{0.6}Sr_{0.4}Co_{0.2}Fe_{0.8}O_{3-δ} Kathoden auf MSCs, Lehrstuhl für Physikalische Chemie, Montanuniversität Leoben, personal document, January 23th, 2018
- [89] Z. Yang, M. Guo, N. Wang, C. Ma, J. Wang, M. Han, *A short review of cathode poisoning and corrosion in solid oxide fuel cell*, International Journal of Hydrogen Energy, 2017
- [90] L. Blum, Possibility of air impurities at FZJ test facility, personal conversation, February 21st, 2018
- [91] A. Egger, Stability studies of secondary phases, personal document, January 23th, 2018

13. Illustration directory

Figure 1: Schematic of a unit cell[1].....	5
Figure 2: Overview of reactants and operating temperatures of the most important types of fuel cells[8]	10
Figure 3: Nissan e-Bio Fuel-Cell vehicle based on the e-NV200 platform[10]	12
Figure 4: Schematic architecture of an electric vehicle incorporating a SOFC-APU[10]	12
Figure 5: APU-system developed by AVL - main parts[9].....	13
Figure 6: Flowsheet of ethanol APU developed by AVL including sensor and actuator position [13]	15
Figure 7: Operating principle of a SOFC[14].....	16
Figure 8: Characteristic IV-curve with different types of losses[1]	19
Figure 9: Comparison of combustion based power plant systems regarding efficiency and power output (ICE = internal combustion engine; GTCC = gas turbine combined cycle; IGCC = integrated gasification combined cycle; GT = gas turbine bottoming cycle[17]	21
Figure 10: Schematic layout of planar (A.1) and tubular (B.1) SOFCs[18]	22
Figure 11: Evolution of the planar solid oxide fuel cell design[5]	23
Figure 12: Fabrication cycle of a MSC developed by Plansee (ITM = intermediate temperature metal; DBL = diffusion barrier layer; PVD = physical vapor deposition; YSZ = yttria stabilized zirconia; CGO = cerium gadolinium oxide; LSCF = lanthanum strontium cobalt ferrite oxide)[20]	24
Figure 13: Schematic of the cathode side triple phase boundary (TPB)[36].....	29
Figure 14: Mechanisms of three different reaction paths for the oxygen reduction at a porous SOFC cathode[46].....	30
Figure 15: Unit cell layout of an ideal ABO ₃ perovskite structure[49].....	31
Figure 16: Brouwer diagram for an acceptor doped La _{1-y} AyBO _{3±δ} showing five different regions of oxygen content δ with their corresponding oxygen vacancy concentration VO•• and electronic conductivity σ as a function of the oxygen partial pressure pO ₂ [55].....	35
Figure 17: Oxygen tracer diffusion D*coefficient and surface exchange coefficient k of La _{0.8} Sr _{0.2} Mn _{1-x} CoxO _{3±δ} as a function of the Cobalt site fraction x at 1000°C[57]	38
Figure 18: Layout of a 2x2x2 supercell of La _{0.75} Sr _{0.25} Co _{0.25} Fe _{0.75} O ₃ [59].....	39

Figure 19: Schematic of degradation phenomena of SOFCs[68]	41
Figure 20: Nyquist-plots of impedance spectra of porous LSCF cathode sample in humidified air with varying water content at 600°C[75]	44
Figure 21: Increase in polarization resistance of LSCF cathode sample depending on concentration of water in air[75].....	44
Figure 22: Time dependent cathodic overpotential of LSCF cathode sample when switching between dry (10 vol% argon in air) and humidified (10 vol% water in air) media at 600°C and constant voltage of 0.25V [75].....	45
Figure 23: Increase in polarization resistance of LSCF cathode sample depending on concentration of CO ₂ in air[75]	46
Figure 24: Amount of SrCO ₃ formed out of LSCF-6428 depending on pCO ₂ at different temperatures [78].....	47
Figure 25: MSC sample cell with 40x40mm LSCF cathode (left); anode side (right)	49
Figure 26: SEM picture of the cross section of MSC sample provided by Plansee SE (left); schematic of cross section with marking of the functional layers (right)[82]	50
Figure 27: Model of EBZ single cell test rig used at the FZJ[86].....	51
Figure 28: Flow diagram of the GUI implemented at the EBZ single cell test rigs at the FZJ[85]	52
Figure 29: Test setup for single cell tests at FZJ: complete housing with steel weights (left); base plate with sample cell assembly (cathode side up) and Pt-current collector grid before final assembly (right)	53
Figure 30: Sample cell assembly with YSZ-frame and glass solder sealing before testing.....	53
Figure 31: Timeplots of cell (T _{cell}) and furnace temperature (T _{furnace}) and cell voltage (U _{cell}) of the LSCF 1 trial.....	59
Figure 32: Overview of IV-measurements recorded at 850°C, 700°C and 650°C after 0/40/80h of exposure (LSCF 1)	60
Figure 33: Detail of IV-curves recorded at 650°C after 0/40/80h of exposure; comparison of current density at 700mV (pink cursor, LSCF 1); 9.65% decrease in current density i	61
Figure 34: Nyquist plots of frequency responses recorded at 650°C after 0/40/80h of exposure (LSCF 1); 6.14% decrease in low frequency resistance	61
Figure 35: Timeplots of cell (T _{cell}) and furnace temperature (T _{furnace}) and cell voltage (U _{cell}) of the LSCF 2 trial.....	62

Figure 36: Overview of IV-measurements recorded at 850°C, 700°C and 650°C after 0/40/80h of exhaust gas exposure (LSCF 2)	63
Figure 37: Detail of IV-curves recorded at 650°C after 0/40/80h of exhaust gas exposure; comparison of current density at 700mV (pink cursor, LSCF 2); 15.33% decrease in current density i	63
Figure 38: Nyquist plots of frequency responses recorded at 650°C after 0/40/80h of exhaust gas exposure (LSCF 2); 20.75% increase in low frequency resistance	64
Figure 39: Timeplots of cell (T_{cell}) and furnace temperature ($T_{furnace}$) and cell voltage (U_{cell}) of the LSCF 3 trial.....	65
Figure 40: Overview of IV-measurements recorded at 850°C, 700°C and 650°C after 0/40/80h of exhaust gas exposure at 500°C (LSCF 3)	65
Figure 41: Detail of IV-curves recorded at 650°C after 0/40/80h of exhaust gas exposure at 500°C; comparison of current density at 700mV (pink cursor, LSCF 3); 6.55% decrease in current density i	66
Figure 42: Nyquist plots of frequency responses at 650°C after 0/40/80h of exhaust gas exposure at 500°C (LSCF 3); 10.99% increase in low frequency resistance	67
Figure 43: Timeplots of cell (T_{cell}) and furnace temperature ($T_{furnace}$) and cell voltage (U_{cell}) of the LSCF 4 trial.....	67
Figure 44: Overview of IV-measurements recorded at 850°C, 700°C and 650°C after 0/40/80h of exhaust gas exposure at 350°C (LSCF 4)	68
Figure 45: Detail of IV-curves recorded at 650°C after 0/40/80h of exhaust gas exposure at 350°C; comparison of current density at 700mV (pink cursor, LSCF 4); 19.92% decrease in current density i	69
Figure 46: Nyquist plots of frequency responses recorded at 650°C after 0/40/80h of exhaust gas exposure at 350°C (LSCF 4); 22.87% increase in low frequency resistance	69
Figure 47: Cell disassembly after completed test cycle; partial delamination and adhesion of cathode layer to Pt-current collector grid.....	72
Figure 48: SEM cross section of green sample (LSCF 0); coarsely porous substrate on the bottom; finely porous cathode layer on top	75
Figure 49: Detail of functional layer interface of LSCF 0 sample with section of delamination marked (left); magnification of delaminated zone (right).....	76

Figure 50: Detail of functional layer interface of LSCF 1 sample with delamination of the cathode across the whole picture (left); magnification of delaminated zone (right)	76
Figure 51: Aerial view of cathode surface of LSCF 1 sample with artifacts spots (blue, green) and vertical cracks (red); SE image (left) and BSD image (right)	77
Figure 52: EDX spectrum of dark residues of LSCF 1 sample marked in Fig.51 showing characteristic LSCF pattern with abnormal carbon peak close to 0keV	77
Figure 53: SEM cross section of LSCF 2 sample with horizontal delamination and vertical cracks (red arrow) of the cathode (left); magnification of delaminated zone (right)	78
Figure 54: Aerial view of cathode surface of LSCF 2 sample with carbon residuals (blue), imprints from current collector grid (green) and vertical cracks (red); SE image (left) and BSD image (right)	79
Figure 55: Aerial view of cathode surface of LSCF 3 sample with carbon residuals (blue), artifact particles (green) and vertical cracks (red); SE image (left) and BSD image (right)	79
Figure 56: Aerial view of cathode surface of LSCF 4 sample with carbon residuals (blue) and vertical cracks (red); SE image (left) and BSD image (right)	80
Figure 57: Overview of XRD-spectra of all five samples; regions of differing signal intensity magnified (1, 2 and 3); $2\Theta=10\dots100^\circ$; $\Delta\Theta=0.02^\circ/\text{step}$; $t_{\text{step}}=1\text{sec}/\text{step}$	82
Figure 58: XRD-spectra of LSCF 0 (1309-175B) sample (red) compared to the characteristic pattern for rhombohedral LSCF-6428 (blue) from the ICDD data base; characteristic peak for rhombohedral system marked at 38.3° (black arrow)	83
Figure 59: XRD-spectra of all five samples in section 1 ($2\Theta=24\dots31^\circ$); identified phases marked in black; not assignable peaks marked in red.....	84
Figure 60: XRD-spectra of all five samples in section 2 ($2\Theta=36\dots41^\circ$); identified LSCF-6428 phase marked in black; not assignable peaks marked in red	85
Figure 61: XRD-spectra of all five samples in section 3 ($2\Theta=42.2\dots48^\circ$); identified LSCF-6428 phase marked in black; reflexes passing through from the substrate marked in green.....	85
Figure 62: XRD-spectra of LSCF 1 and LSCF 2 sample compared to characteristic patterns of LSCF-6428 and various possible secondary phases.....	86
Figure 63: Thermodynamic stability modelling of possible secondary phases at 350, 500 and 650°C (using FactSage v6.4)[91].....	109

14. List of tables

Table 1: Comparison of fuel cell technologies [4][5][6]	6
Table 2: Influences on fuel cell type selection	9
Table 3: Vehicle data for Nissan e-Bio Fuel-Cell® vehicle[10]*	13
Table 4: Nernst equations according to different fuel cell reactions (see 4.1.)[1].....	18
Table 5: Functionality and processing of the different layers of a state-of-the-art MSC	25
Table 6: Most common perovskite materials used in SOFCs (CTEs of electrolytes are usually 10-12ppm/K; σ_e =electronic conductivity, σ_i =ionic conductivity)[5]	28
Table 7: Gas fractions of calculated exhaust gas for exposure to cell cathode	49
Table 8: Gas fractions for cell anode during operation	49
Table 9: Buildup of tested MSC sample cells[82]	50
Table 10: Startup procedure for single cell tests at FZJ	55
Table 11: Test matrix; total anode gas flow: 20NI/h; total cathode gas flow: 40NI/h .	57
Table 12: Summary of collected data from cell tests	71
Table 13: Possible failure modes of samples cells exposed to exhaust gas containing H ₂ O and CO ₂ [87].....	74
Table 14: List of ferritic alloys for porous metallic SOFC substrates[25].....	107
Table 15: List of perovskite type materials for SOFC cathode application, thermal expansion coefficient (TEC), electronic and ionic conductivity (σ_e , σ_i)[36].....	108

15. Appendix

Table 14: List of ferritic alloys for porous metallic SOFC substrates[25]

Alloy	Supplier	Composition
Ferrochrom (1.4742)	ThyssenKrupp	18% Cr, 0.9% Al, 0.9% Si, 0.69% Mn, 0.06% C
CrAl20 5 (1.4767)	ThyssenKrupp	19% Cr, 5.5% Al, 0.5% Si, 0.5% Mn, 0.05% C
FeCrAlY	Technetics	22% Cr, 5% Al, 0.1% Y
ZMG 232	Hitachi Metals	21% Cr, 0.08% Al, 0.43% Si, 0.47% Mn, 0.02% C
SUS 430 HA	Nippon Steel	16% Cr, 0.13% Al, 0.29% Si, 0.13% Mn, 0.05% C
SUS 430 Na	Nippon Steel	16% Cr, 0.01% Al, 0.29% Si, 0.56% Mn, 0.05% C
CroFer22 APU	ThyssenKrupp	22% Cr, 0.12% Al, 0.1% Si, 0.41% Mn, 0.16% Ni, 0.05% Ti, 0.08% La
IT 14	Plansee	26% Cr, < 0.03% Al, < 0.03% Si, Mo, Ti, Mn, Y ₂ O ₃

Table 15: List of perovskite type materials for SOFC cathode application, thermal expansion coefficient (TEC), electronic and ionic conductivity (σ_e , σ_i)[36]

Composition	TEC ($\times 10^{-6} \text{K}^{-1}$)	T ($^{\circ}\text{C}$)	σ_e (Scm^{-1})	σ_i (Scm^{-1})
$\text{La}_{0.8}\text{Sr}_{0.2}\text{MnO}_3$	11.8	900	300	5.93×10^{-7}
$\text{La}_{0.7}\text{Sr}_{0.3}\text{MnO}_3$	11.7	800	240	–
$\text{La}_{0.6}\text{Sr}_{0.4}\text{MnO}_3$	13	800	130	–
$\text{Pr}_{0.6}\text{Sr}_{0.4}\text{MnO}_3$	12	950	220	–
$\text{La}_{0.8}\text{Sr}_{0.2}\text{CoO}_3$	19.1	800	1,220	–
$\text{La}_{0.6}\text{Sr}_{0.4}\text{CoO}_3$	20.5	800	1,600	0.22
$\text{La}_{0.8}\text{Sr}_{0.2}\text{FeO}_3$	12.2	750	155	–
$\text{La}_{0.5}\text{Sr}_{0.5}\text{FeO}_3$	–	550	352	–
	–	800	369	0.205
$\text{La}_{0.6}\text{Sr}_{0.4}\text{FeO}_3$	16.3	800	129	5.6×10^{-3}
$\text{Pr}_{0.5}\text{Sr}_{0.5}\text{FeO}_3$	13.2	550	300	–
$\text{Pr}_{0.8}\text{Sr}_{0.2}\text{FeO}_3$	12.1	800	78	–
$\text{La}_{0.7}\text{Sr}_{0.3}\text{Fe}_{0.8}\text{Ni}_{0.2}\text{O}_3$	13.7	750	290	–
$\text{La}_{0.8}\text{Sr}_{0.2}\text{Co}_{0.8}\text{Fe}_{0.2}\text{O}_3$	20.1	600	1,050	–
$\text{La}_{0.8}\text{Sr}_{0.2}\text{Co}_{0.2}\text{Fe}_{0.8}\text{O}_3$	15.4	600	125	–
$\text{La}_{0.6}\text{Sr}_{0.4}\text{Co}_{0.8}\text{Mn}_{0.2}\text{O}_3$	18.1	500	1,400	–
$\text{La}_{0.6}\text{Sr}_{0.4}\text{Co}_{0.8}\text{Fe}_{0.2}\text{O}_3$	21.4	800	269	0.058
$\text{La}_{0.6}\text{Sr}_{0.4}\text{Co}_{0.2}\text{Fe}_{0.8}\text{O}_3$	15.3	600	330	8×10^{-3}
$\text{La}_{0.4}\text{Sr}_{0.6}\text{Co}_{0.2}\text{Fe}_{0.8}\text{O}_3$	16.8	600	–	–
$\text{La}_{0.8}\text{Sr}_{0.2}\text{Co}_{0.2}\text{Fe}_{0.8}\text{O}_3$	14.8	800	87	2.2×10^{-3}
$\text{La}_{0.8}\text{Sr}_{0.2}\text{Co}_{0.8}\text{Fe}_{0.2}\text{O}_3$	19.3	800	1,000	4×10^{-2}
$\text{La}_{0.6}\text{Sr}_{0.4}\text{Co}_{0.9}\text{Cu}_{0.1}\text{O}_3$	19.2	700	1,400	–
$\text{Pr}_{0.8}\text{Sr}_{0.2}\text{Co}_{0.2}\text{Fe}_{0.8}\text{O}_3$	12.8	800	76	1.5×10^{-3}
$\text{Pr}_{0.7}\text{Sr}_{0.3}\text{Co}_{0.2}\text{Mn}_{0.8}\text{O}_3$	11.1	800	200	4.4×10^{-5}
$\text{Pr}_{0.6}\text{Sr}_{0.4}\text{Co}_{0.8}\text{Fe}_{0.2}\text{O}_3$	19.69	550	950	–
$\text{Pr}_{0.4}\text{Sr}_{0.6}\text{Co}_{0.8}\text{Fe}_{0.2}\text{O}_3$	21.33	550	600	–
$\text{Pr}_{0.7}\text{Sr}_{0.3}\text{Co}_{0.9}\text{Cu}_{0.1}\text{O}_3$	–	700	1236	–
$\text{Ba}_{0.5}\text{Sr}_{0.5}\text{Co}_{0.8}\text{Fe}_{0.2}\text{O}_3$	20	500	30	–
$\text{Sm}_{0.5}\text{Sr}_{0.5}\text{CoO}_3$	20.5	700~900	>1,000	–
$\text{LaNi}_{0.6}\text{Fe}_{0.4}\text{O}_3$	11.4	800	580	–
$\text{Sr}_{0.9}\text{Ce}_{0.1}\text{Fe}_{0.8}\text{Ni}_{0.2}\text{O}_3$	18.9	800	87	0.04

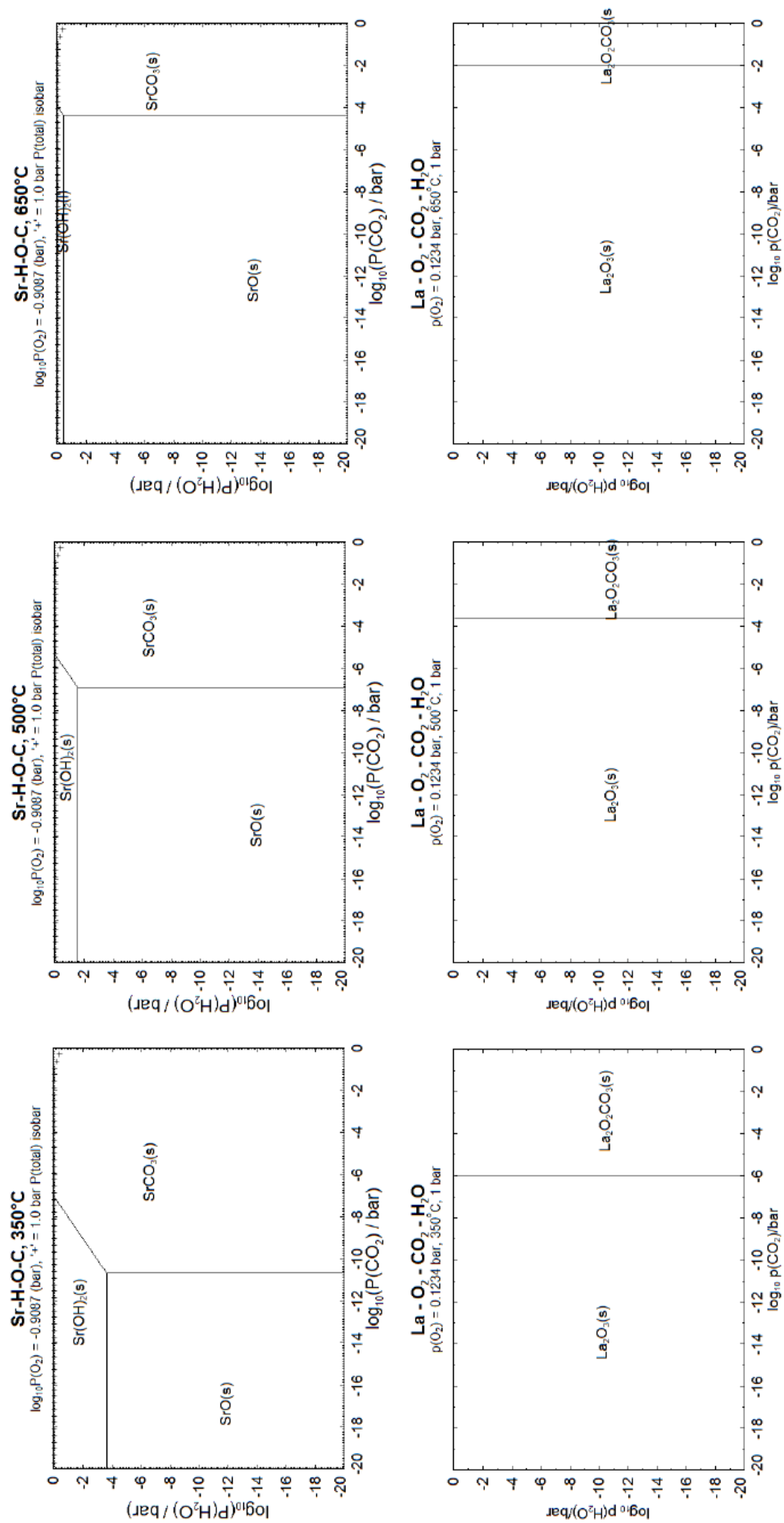


Figure 63: Thermodynamic stability modelling of possible secondary phases at 350, 500 and 650°C (using FactSage v6.4)[91]